The Growth and Morphology of Small Ice Crystals in a Diffusion Chamber

Georg Ritter

Thesis submitted to the University of Hertfordshire in partial fulfilment

of the requirements of the degree of

Doctor of Philosophy

September 2014

School of Physics, Astronomy and Mathematics,

University of Hertfordshire, UK.

Declaration

I, Georg Ritter, confirm that the work presented in this thesis is my own. Where information has been derived from other sources, I confirm that this has been indicated in the thesis.

Abstract

Small water ice crystals are the main component of cold tropospheric clouds such as cirrus. Because these clouds cover large areas of our planet, their role in the radiation budget of incoming and outgoing radiation to the planet's surface is important. At present, the representation of these clouds in climate and weather models is subject to improvements: a large part of the uncertainty error stems from the lack of precise micro-physical and radiation model schemes for ice crystal clouds.

To improve the cloud representations, a better understanding of the life time dynamics of the clouds and their composition is necessary, comprising a detailed understanding of the ice particle genesis, and development over their lifetime.

It is especially important to understand how the development of ice crystals over time is linked to the changes in observable variables such as water vapour content and temperature and how they change the light scattering properties of the crystals.

Recent remote and aircraft based in-situ measurements have shown that many ice particles show a light scattering behaviour typical for crystals having rough surfaces or being of complex geometrical shapes.

The aim of this thesis was to develop the experimental setup and experiments to investigate this further by studying the surface morphology of small water ice crystals using scanning electron microscopy (SEM). The experiments I developed study the growth of water ice crystals inside an SEM chamber under controlled environmental conditions. The influence of water vapour supersaturation, pressure and temperature is investigated.

I demonstrate how to retrieve the surface topology from observed crystals for use as input to computational light scattering codes to derive light scattering phase functions and asymmetry parameters, which can be used as input into atmospheric models.

Difficulties with the method for studying the growth of water ice crystals, such as the effect of the electron beam-gas ionization and charging effects, the problem of facilitating repeated and localized ice growth, and the effect of radiative influences on the crystal growth are discussed. A broad set of nucleation target materials is studied.

In a conclusion, I demonstrate that the method is suitable to study the surface morphologies, but is experimentally very challenging and many precautions must be taken, such as imaging only once and preventing radiative heat exchange between the chamber walls and the crystals to avoid unwanted effects on the crystal morphology. It is also left as a question if a laboratory experiment, where crystals will need to be grown in connection to a substrate, can represent the real world well enough. Deriving the required light scattering data in-situ might be an alternative, easier way to collect data for modelling use.

Contents

List of Tables

List of Figures

Acknowledgements

I would like to express my gratitude to Prof. Zbigniew Ulanowski, my principal supervisor, for his enthusiastic support, his curiosity, his invaluable and tireless review of my research project, for his guidance and teaching, scientifically, professionally and personally over the past four years.

I would like to extend this gratitude to Dr. Evelyn Hesse, my secondary supervisor, for her advice and discussions.

I also would like to thank Prof. Paul Kaye and his group with Dr. Chris Stopford, Dr. Edwin Hirst, Dr. Richard Green and Dr. Warren Stanley for their support and help with all sorts of experimental questions and for allowing me to become a member of their team.

I thank Dr. Ole Steuernagel for his enthusiastic advice on mathematical and theoretical questions and for sharing his exciting quantum mechanics project.

My thanks and gratitude also go to Prof. William E. Martin for many interesting discussions and his invaluable advice and help on laser optics.

I would like to thank Prof. Mark Tracey, Dr. Ian Johnston, Dr. Tan Christabel, Dr. Loïc Coudron for sharing their laboratory, their materials and protocols and helping out with equipment, parts and cables and their knowledge on surfaces. I would also like to thank Prof. Andreas Chrysantou, for allowing me to use some of his diamond materials.

My thanks also extend to Prof. Ben Murray and his team at University Leeds, for his generosity in sharing samples, protocols and knowledge, when I visited their group.

I wish to thank all the post-docs, staff, students and colleagues in the lab, at the Centre for Atmospheric and Instrumentation Research at UH, who I can not cite individually, but who have contributed to my education and research during my student years.

My deepest gratitude goes to my wife Laura, for encouraging me not to give up, her support and for the exciting time spent in her lab and our labs.

Finally, I wish to thank my family and friends for sharing this exciting time with me.

Publications and Presentations

- A diffusion chamber design to study effects of temperature, ambient pressure and water vapour saturation on the fine structure of ice crystals using scanning electron microscopy, G Ritter, E Hesse, PH Kaye and ZJ Ulanowski; poster presentation, 16th International Conference on Clouds and Precipitation, Leipzig, Germany, 2012

- Optogenetic Tools Applied to Target Interneurons and to Suppress Epileptiform Activity in Vivo, L Mantoan Ritter, RC Wykes, DC MacDonald, G Ritter, JH Heeroma, S Schorge, MC Walker, DM Kullmann; poster presentation, British Neuroscience Association Meeting, London, April 2013.

- In-situ SEM Imaging of Water Ice Crystal Growth in a Small Diffusion Chamber, G Ritter, JZ Ulanowski; poster presentation, Annual Conference of the British Association for Crystal Growth, Leeds, 2014

- Investigation of nucleation, dynamic growth and surface properties of single ice crystals, J Voigtlaender, P Herenz, C Chou, H. Bieligk, T Clauss, D Niedermeier, G Ritter, JZ Ulanowski, and F Stratmann, Geophysical Research Abstracts, Vol. 16, EGU2014-5649, 2014, EGU General Assembly 2014

- Wigner Flow Reveals Topological Order in Quantum Phase Space Dynamics, O Steuernagel, D Kakofengitis, G Ritter, Physical Review Letters, 110(3), 2013.

Chapter 1

Introduction

1.1 The Role of the Atmosphere in Radiation Transport

The sun is our planet's main source of energy by providing the large amount of 340 Wm^{-2} longitudinally averaged (a total of about 1.3×10^4 TW), in the form of sunshine. Of this total electromagnetic radiation about a third is reflected back into space and does not enter the Earth's system. The remaining two thirds interact with the planet in a complex way and large parts are absorbed by the oceans, the terrestrial surfaces or in the atmosphere (figure 1.1). It is this amount of absorbed energy which fuels the motors of our climate, the large systems that transport heat across the Earth: the thermohaline circulation which constantly moves large amounts of water across our globe's oceans or the atmospheric Hadley cell system, one of the three primary atmospheric circulation systems, which transports warm air masses that are generated at the equator and rise to high altitudes polewards.

The interactions at these circulation cell boundaries, which in the case of the Hadley cell is with the neighbouring Ferell cell, together with the forces originating from the rotation of the planet, are responsible for phenomena such as jet streams, trade winds, the subtropical deserts or the tropical rain belt. The circulatory systems in general equilibrate the temperature differences on our planet, but they also define our climate, locally as well as globally. A collapse of one of the main systems would have severe, far reaching implications.

They are all part of the one complex system Earth. But in order to reduce the complexity it is necessary to study individual systems and their interactions

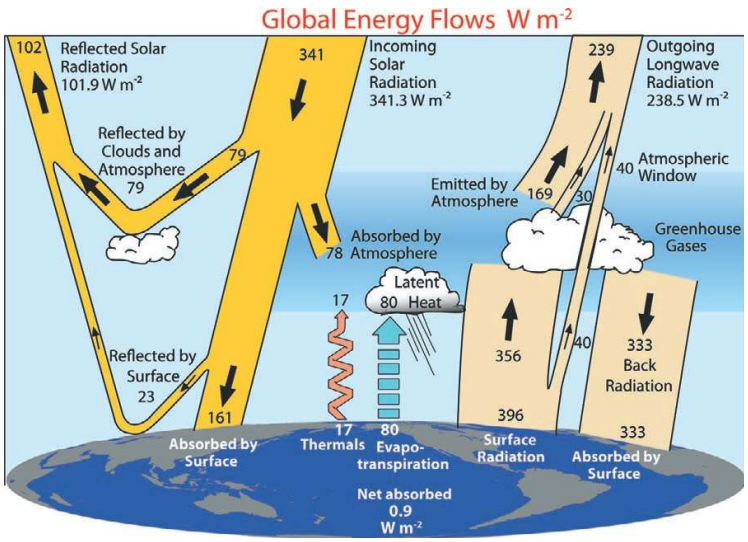

Figure 1.1 – Annual mean — years 2000 to 2004 — of energy flows (Wm^{-2}) for Earth; reproduced from Trenberth et al. (2009).

separately. The main driver for couplings is, often in complex ways, radiation: radiation is absorbed and stored as heat or latent heat, which can be transported over large distances by circulatory systems in the atmosphere or the oceans, and it can be re-emitted. In this context it is important that different cloud layers and land and water surfaces interact with radiation differently.

Understanding the Earth's radiative and other physical properties and mechanisms, couplings and thermodynamics is key to understanding the Earth and its climate as a global system.

1.1.1 The Atmosphere

The atmosphere is the defining system for climate. It forms an approximately 100 km layer interfacing Earth to space and all incoming and outgoing radiation passes through it. It consists of mainly oxygen and nitrogen and a small fraction (<1%) of other gases. Although only present in a small amount, many important radiative properties of the atmosphere are a result of the presence and migration of these other gases, with, from a climate perspective, the most important gases being carbon dioxide (CO_2), water vapour (H_2O) and methane (CH_4).

Water vapour accounts for only 0.25% of the total mass of the atmosphere, and is up to 99.5% in vapour phase (Stevens and Bony (2013)). But it assumes a special role due to its physical and radiative properties.

Firstly, the radiative properties of the water molecule make it highly absorbent in the infra-red regions. The angled water molecule with its dipole moments has many vibrational and rotational modes which can be excited: this leads to closely spaced resonance frequency peaks. Together with other effects such as Doppler line broadening, this has the consequence that a layer of water vapour is nearly opaque for all wavelengths except for a range in the visible and some windows in the infra-red (IR) spectrum. It is the most important absorber of incoming solar energy. The other highly abundant diatomic gases O_2, N_2, as well as CO_2 only absorb a small fraction as they have linear molecule topology and only absorb by electronic excitation. Nitrogen does significantly contribute to the absorption, and oxygen absorbs 2% of the incoming radiation. In comparison, water vapour absorbs 70% thereof (e.g. Maurellis and Tennyson (2003)). It also has a high variability in space and time, whilst this is not the case for the other radiatively important gases, which are mixed and distributed more evenly.

Secondly, the unique phase diagram of water defines the transitions between its gaseous, liquid and solid form and interlinks them with atmospheric temperatures and pressures. Because the phase boundaries fall into the atmospherically occurring temperatures, they define the processes involved in formation and the lifecycle of hydrometeors, which are condensed water in liquid or solid state – ice. They form through condensation or nucleation, when changes in the local thermodynamic parameters lead to a sufficient saturation of the water vapour. The phase diagram of water further governs the interaction of the hydrometeors with remaining or newly introduced water vapour, as well as governing the transport and convective properties of air parcels, by determining their density, water vapour content and temperature. Something to note is that generally air parcels in the atmosphereare not in thermodynamic equilibrium state.They constantly move, are mixed and take up or loose energy.

The phenomenon whereby long wave radiation emitted from the surface is absorbed in the atmosphere and radiated back to the ground, thereby reducing the loss of heat into space is referred to as the greenhouse effect (Fourier (1824), Tyndall (1863), Arrhenius (1896)). Although water vapour is the most effective greenhouse gas contributing about 50% of Earth's greenhouse effect (clouds contribute a further 25%), CO_2 with its 20% contribution (aerosols and remaining gases contribute the remaining 5%) is the most climate relevant greenhouse gas. Its atmospheric concentration controls the long term temperature. Because

water vapour can condense, evaporate and precipitate it reacts rapidly to temperature changes leading to fast (usually negative) feedbacks, whereas the non-condensing gases remain for decades in the atmosphere (Lacis et al. (2010)). Numerical experiments in which the CO_2 has been removed demonstrate this dependence clearly and ice core data on atmospheric CO_2 from the Antarctic and Greenland show cycles over the glacial- interglacial cycles during the past 650,000 years (Stocker et al. (2013)).

The hydrometeors themselves are the building blocks of clouds, which are the third reason for the importance of atmospheric water vapour. Only a tiny fraction of the atmospheric water is present in the form of clouds, but their influence on the radiation budget is substantial.

Ensembles of water droplets and ice crystals that make up most clouds, change the amount of reflected and re-emitted radiation as light is absorbed and scattered differently at the particles and droplets. Composition and particle size distributions (PSD) of the cloud particles define the different cloud variants, besides temperatures and their locations. In rain clouds, for example, water droplets can grow to millimetre sizes; once they are heavy enough to counter uplifting air movements, they fall towards the ground as rain. Other clouds, such as cold cirrus contain predominately small ice crystals and are found high in the atmosphere.

The real importance of clouds, besides being the source of precipitation, is the radiative effect they have on the global radiation budget. Large areas of the planet surrounding the Earth's sphere are constantly covered with clouds. If the cloud cover or its radiative properties change, this will affect the total energy budget. If a very high altitude cloud prevented large parts of incoming solar radiation from entering the atmosphere, the overall energy uptake would be substantially reduced. If, at the same time, it also lets IR radiation escape to space, the overall effect would be a cooling of the whole system. If, on the contrary, a high layer of clouds strongly reflect back this long wave radiation originating from the terrestrial surface, and heat becomes trapped, but also still lets incoming radiation pass into the system, the overall effect is a warming.

Considering the overall warming of the planet (Stocker et al. (2013)), the biggest uncertainty lies in how changes in the cloud system contribute to the future development of our climate, and how the cloud system is influenced by the changes in the climate — the cloud-climate feedback.

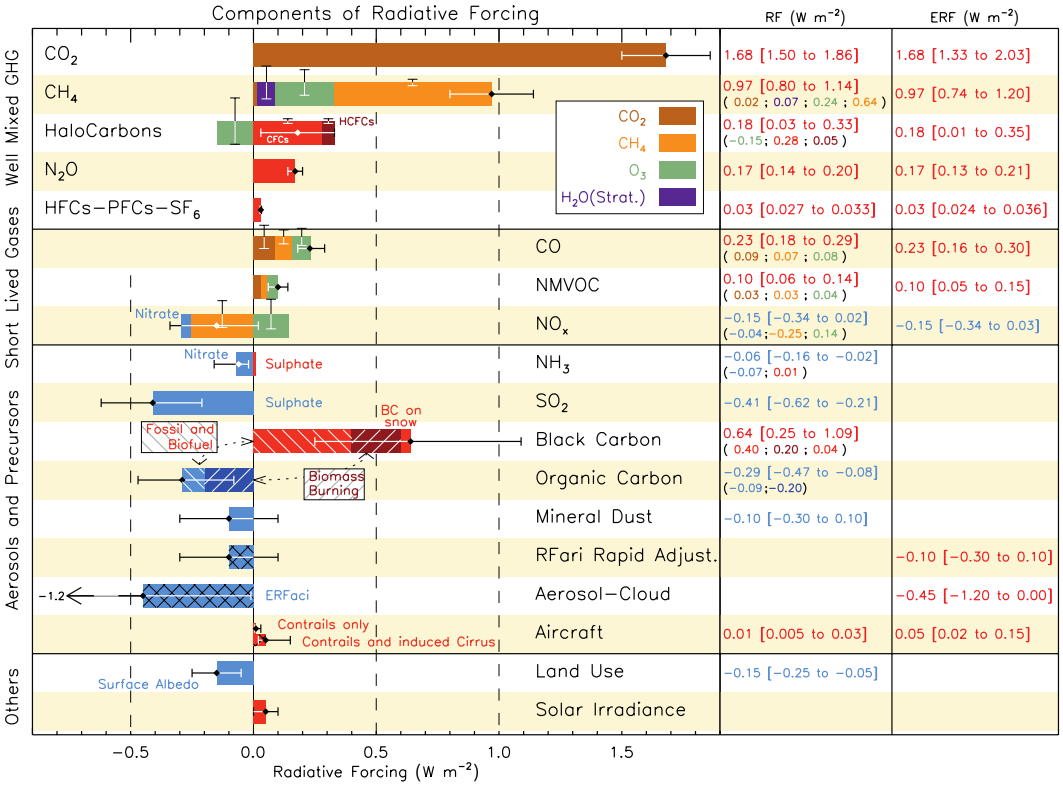

Figure 1.2 – Radiative forcing (RF) of climate change during 1750-2011, as published in the 5th IPCC Assessment Report (Stocker et al. (2013), p. 57). The overall uncertainty for the Aerosol-Cloud (third from bottom) is, as the others, indicated in horizontal bars (vertical: individual components). Best estimates for the total and individual components of the response are given in the right columns. Effective radiative forcing (ERF); ERFaci: ERF due to aerosol-cloud interaction, chlorofluorocarbons (CFC), hydrochlorofluorocarbons (HCFC), hydrofluorocarbons (HFC), perfluorocarbons (PFC), non-methane volatile organic compounds (NMVOC), black carbon (BC).

The uncertainty originates partly from the way climate research is conducted: because it is very difficult to study large scale systems in the laboratory, most of the research is based on observing the real system and is trying to reproduce the behaviour in the numerical domain using computational models. Because computational resources are restricted, modellers need to choose which physical processes they represent and to what level of detail. This is sometimes done by representing only a selection of processes or even, if the computational effort is too large, using parametrisations. The ultimate goal is an exact match between model and past and current observations.

Since the introduction of the first general circulation models (GCM) 50 years ago by Smagorinsky (1963), there has been a lot of progress and models have advanced a lot: today they include a great amount of detailed processes, in a way that allows them to correctly reproduce surface temperature development over decades or even millennia, but also reproduce shorter events such as cooling caused by a volcanic ash cloud (Stocker et al. (2013), p.15).

In the current models the representation of clouds and moist convection, and the coupling of atmospheric water with circulation is still one of the main limitations (Stevens and Bony (2013)), which also affects the cloud forcing — the contribution of the cloud cover to the radiation budget. This is still ranked number one for uncertainties in modelling, and has been so for some time (Baker (1997), Zickfeld et al. (2010) and Stocker et al. (2013), p. 14).

Figure 1.2 lists the expected contributions from different components to the radiative forcing and it can be seen that the uncertainty (horizontal black error-bars) for the Aerosol-Cloud interactions is greater than the effective forcing itself and covers the full range of -1.2 – 0 Wm^{-2}.

The difference of cloud radiative effects in current models, investigated in the Cloud Feedback Model Intercomparison Project (CFMIP) by Williams and Webb (2009), can be as high as ± 20 Wm^{-2} in the tropics, and between -50 Wm^{-2} and -15 Wm^{-2} elsewhere (Baran et al. (2014b)).

1.2 Cirrus Clouds

High altitude clouds, cirrus (figure 1.3) in particular, are an area that needs improvement due to the importance of their radiative contributions, which in

Figure 1.3 – Cirrus clouds (upper quadrants) on a cold day, Wilcox Pass, Jasper National Park, Canada 22nd June 2013 (left). Air traffic contrails with fall-streaks and convective development, Hatfield 25th September 2014 (right).

turn are determined to a large extent by the basic scattering properties of the ice crystals the clouds consist of.

They typically appear as wispy, flimsy streaks and normally form above 6 km altitude in the upper troposphere. Sometimes they give rise to optical phenomena such as halos, sun dogs (parhelia) or colourful arcs. But they can also be 'optically thin' and invisible to the human eye.

They contribute up to about 30% of the high cloud cover globally, with areas of up to 60%-80% in the tropics (Sassen et al. (2008), Stubenrauch et al. (2006), Eleftheratos et al. (2007) Spichtinger et al. (2003) and Baran (2012)). Studies from Guignard et al. (2012) reveal that cirrus make about 25% of all high clouds, and Heidinger and Pavolonis (2005) show that in between 60°N and 60°S cirrus occurs about 40% of the time of the day between January and July, overlapping clouds beneath. This makes cirrus important also in terms of atmospheric coverage.

Several factors need to be understood in order to improve the representation of cirrus in models: size, shapes, spatial and number distributions of the ice crystals in cirrus and how these are linked to the observable variables such as temperature, pressure and water content, and the processes involved in the formation and the changes over the life cycle of the crystals. There are two main ingredients to a comprehensive understanding of the radiative effects of cirrus: understanding the cloud microphysics and improving the understanding of light scattering properties of small particles in the atmosphere.

1.2.1 Cloud Microphysics

The first step is understanding the ice particle formation. This includes a detailed view on the development pathways ice particles are known to follow in clouds. Some of the mechanisms are well understood, others less.

Homogeneous ice nucleation, one possible process involved in the formation of a cirrus cloud, is the process when enough water molecules form a cluster that ultimately grows into a bulk solid. This generally happens only at very low temperatures. Small micrometer sized pure water droplets can remain liquid down to about -41°C, which is the homogenous ice nucleation temperature.Metastable bulk liquid water has been found to exist as low as -46°C (Sellberg et al. (2014)).

Several studies have investigated the formation of water clusters from vapour using molecular dynamics (Matsumoto et al. (2002)), and laser based spectroscopy or electron diffraction (Bartell (1986)) to learn more on the structure and conditions when this happens. A good review on cold small water clusters is in Buch et al. (2004). They investigate clusters of a size range of n=20-931 molecules computationally and experimentally and find that only the bigger clusters have a well ordered lattice structure in the interior, but a disordered surface. This is interesting, because this suggests that an ordered lattice structure is only reached at a later stage when more molecules have become part of the bulk.

How already formed liquid water droplets grow from surrounding available water vapour is reasonably well understood (Wallace and Hobbs (2006), Hegg and Baker (2009)). In essence this is related to the free energy of the surface of a droplet and the connected water vapour pressure, which can be formulated in terms of the energy needed to accept a molecule or remove a molecule from the bulk. From this, the dynamics of the growth of a droplet ensemble can be described by several mechanisms— growth from vapour or by collection of other droplets. If the liquid droplets freeze they become part of the ice fraction of the cloud.

The heterogeneous nucleation process involves a third agent, an ice nucleating particle or IN, aiding crystal formation and is less well understood (see e.g. Hoose and Möhler (2012), a review on experiments and Murray et al. (2012), a review on immersion freezing). Ice nucleation particles include small mineral dust

particles (mostly clay minerals), biological material or aerosols containing organics, and soots (Vali (1996)). They all vary in their abundance, concentration and nucleation efficiency. The importance of IN altered cloud microphysics becomes evident if one considers the abundance of anthropogenic and natural particles in the atmosphere; for mineral dusts a flux of 1000 to 3000 Tg yr^{-1} is estimated (Zender et al. (2004)). Once in the atmosphere these particles can stay airborne for weeks and travel great distances between continents before they are released out of the atmosphere. At present, several pathways are distinguished: immersion and (vapour) deposition mode nucleation and contact nucleation. In the first case an IN is in contact with the liquid phase of water, in the second water molecules start to attach from the vapour phase onto the surface of the IN and grow into an ice crystal, nucleation through contact involves a IN initiating the freezing of a droplet.

The influence of IN on nucleation and freezing kinetics of water is large. Certain mineral dusts, such as feldspar have been shown to be extremely efficient ice nucleators and to increase the freezing temperatures of droplets by many degrees (Atkinson et al. (2013)). The best known ice nucleators are biological, the cell membrane proteins facilitate the freezing of small droplets at temperatures as high as just below 0 °C or -2 °C in the case of *Pseudomonas syringae* (see review in Morris et al. (2004)), steroids are effective (Fukuta and Mason (1963)) and organic molecules can change ice nucleation behaviour as well (Vali (1996)). The presence of any IN has the ability to change how the clouds form and how the particles and their size distributions develop.

Although some progress has been made to fundamentally understand the chemical-physics mechanisms involved (early requirements are outlined in Pruppacher and Klett (2010)), it is yet not possible to compute or predict a material's ice nucleation behaviour. Hu and Michaelides (2010) for example investigated the adsorption of water onto a kaolinite surface using physical-chemistry codes: kaolinite, a clay mineral, is an experimentally proven effective heterogeneous ice nucleator. But the modelling studies did not succeed in answering the fundamental question as to why. They show that the perfect kaolinite surface is polar and hypothesize that only through incorporating external atoms can good attachment of water molecules be achieved. They, in fact, also show (Hu and Michaelides (2008)), that although water effectively wets a kaolinite surface, the formed bilayer is actually hydrophobic and does not

favour the further formation of hexagonal ice. This is just an example to illustrate, that the fundamental mechanisms that make a material a good ice nucleator are still not understood.

Also the idea that a close lattice spacing of the bulk material with I_h would result in good ice nucleation behaviour is still disputed (references in Feibelman (2008)) and, basing on Monte Carlo computations (Cox et al. (2012)), it has been suggested to use the O–O spacing as an indicator instead. Originally, β-AgI, a material with a lattice constant within 1% of the I_h, was suggested as an ice nucleator for cloud seeding purposes — the process of introducing a substance into the atmosphere to aid formation of clouds, or modify existing clouds ultimately resulting in precipitation (Vonnegut (1947), Bruintjes (1999)). Studies on other materials, with close lattice spacings showed that BaF_2(111) is a poor nucleator (Conrad et al. (2005)) and sapphire (α-Al_2O_3(0001)) particles did not preferentially nucleate (Thomas (2009)).

Also not well understood is the influence of the nucleation material or shape on the macroscopic manifestation of the ice crystals, which strongly affects their radiative properties, when they have grown. This leads to the second component outlined below.

1.2.2 Single Ice Crystal Properties

The variety of shapes and their distribution inside the clouds, determines not only the bulk properties of the clouds but also their radiative properties (McFarquhar and Heymsfield (1997), McFarquhar et al. (2000)). The variety of shapes — referred to as habits — ranges from simple hexagonal prisms to more complicated geometries such as hollow columns and rosettes, needles and even aggregates. The shapes, sizes and their relative numbers depend on the temperature and humidity which has been available during the growth periods (Lynch (2002)). The more complex shapes tend to appear in denser clouds and at the cloud bottom (Baran (2012)). Early work investigating the dependence of atmospheric ice crystal shapes with temperature and supersaturation was done by Ukichiro Nakaya (Furukawa and Wettlaufer (2007)) and is represented in the famous Nakaya crystal habit diagram, updated diagrams were subsequently presented by Kobayashi (1961), and an updated version is in Bailey and Hallett (2009). Much work was done by Hallett and Mason (1958); a classification of

crystal shapes is given by Magono and Lee (1966) and an updated version is in Kikuchi et al. (2013), which extends Magono and Lee's 80 variants to 121 different shapes.

The light scattering properties of single crystals varies strongly depending on their size and the complexity of the crystal and the mesoscopic surface structures. One approach to derive cloud radiative properties, as needed for climate models, is to measure or compute the single crystal light scattering properties, represented in the particle's scattering phase function. The phase function $p(\overrightarrow{\Omega_{inc}}, \overrightarrow{\Omega_{sca}})$ describes the probability of an incoming photon along $\overrightarrow{\Omega_{inc}}$ being scattered into $\overrightarrow{\Omega_{sca}}$, with the scatterer at the centre of the coordinate system. Once this is known, it can be used to express the scattering properties of an ensemble of (randomly oriented) particles with a phase function only dependent on cos(Θ), with $\cos(\Theta) \equiv \overrightarrow{\Omega'_{sca}} \cdot \overrightarrow{\Omega_{inc}}$ where Θ is the scattering angle. Simplifying this further, the asymmetry parameter g is defined as

$$g =< \cos(\Theta) >= \frac{1}{2} \int_{-1}^{1} p(\cos(\Theta))\ \cos(\Theta)\, d\cos(\Theta) \tag{1.1}$$

as a measure of the ratio of forward to backward scattered amounts and represents how much radiation is reflected back to space as opposed to being transmitted downwards. A low value makes a cloud look bright as seen from space, a high value makes it transparent.

Formally, g can have a range from -1 to 1 (fully backwards to fully forwards) and frequently is used in climate models (for example in the Edwards et al. (2007) scheme to model the radiative influence of cirrus) to represent cloud forcing. Another frequently used parameter, especially in energy-balance calculations, is the single-scattering albedo $\omega = \sigma_s/(\sigma_\alpha + \sigma_s)$, with σ_s the scattering coefficient and σ_α the absorption coefficient (Kiehl and Ramanathan (2006)).

The main problem is to derive phase functions for particles occurring in the atmosphere. For spherical particles such as a droplet, Maxwell's equations become separable and an exact solution was computed by Mie (1908), but for other geometries it is more complicated. Many approaches are used: Mie theory, Rayleigh scattering, geometrical optics with or without various enhancements, analytic models based on solving Maxwell's equations such as T-matrix, and various numerical approaches based on discretization in the space and/or time

domain. Which regimes are applicable depends on the size of the particle in relation to the scattered wavelength: the size parameter

$$x = \frac{2\pi r}{\lambda} \tag{1.2}$$

with r being a typical length of the particle and λ the wavelength. The exact meaning of the size parameter is author dependent. Some authors use r/λ. Choices for r vary between the diameter, height (of a hexagonal column for example), or for non uniform geometries, a diameter d is chosen to be the greatest distance of the points and $r = d/2$.

Nevertheless, they allow us to determine if the particle is sufficiently small (typically $r < \lambda/10$) relative to the wavelength. If so, Rayleigh scattering on a dipole is used. If the particle is large relative to the wavelength, a geometrical optics approach involving ray-tracing can be used to get approximations of the scattering phase functions (Petty (2006), Macke et al. (1998), Yang and Liou (1998)).

If the particle is small enough, the wave propagation can be computed numerically using a discrete dipole approximation (Yurkin and Hoekstra (2011)). Because in this method particles are represented as dipoles on a numerical grid with spacing $a < \lambda/10$, the solvable particle sizes quickly are limited by the computational resources.

For an intermediate size in which diffraction plays a non-negligible role, hybrid methods are developed, such as the ray-tracing with diffraction on facets (RTDF) (Hesse and Ulanowski (2003)).

The resulting phase functions are then used to derive the scattering properties of an ensemble, as for example outlined in Labonnote et al. (2007) and Baran et al. (2014a): a Monte Carlo integration (Macke et al. (1996)) is used to predict the scattering phase function for the ensemble, by randomly orientating the ensemble crystals.

All methods require a representation of the single crystal, and surface effects are difficult to incorporate, but most essentially the shapes and surfaces need to be linked with the atmospheric relevant temperatures, humidities and dynamics of the particles.

1.3 Evidence for Roughness, Observations and Experiments

Several observational methods are in use to inform the parameterisation schemes for cirrus (and other clouds) in climate models: remote sensing methods such as satellite observation or laser based light detection and ranging (LIDAR), and in-situ methods, in which instruments are flown into the clouds. Within the in-situ methods, the main group are cloud particle instruments which are mounted below the wings of aircraft; balloon-sondes or unmanned aerial vehicle (UAVs) are other, less frequently used options.

The cloud probes are based primarily on optical imaging methods and the newer designs have an open air sampling volume since it has been shown that air inlet geometries skew the particle density functions, because ice particles shatter on the inlets and then get into the detection volumes. Jensen et al. (2009), who use an open geometry probe and compare results to other frequently used cloud probe models, give an overview. Korolev et al. (2010) studied the impact of ice particle shattering in a cold wind tunnel experiment in more detail and came to the same conclusion. They also suggested probe tips shape changes as a remedy, especially when used in combination with data processing algorithms based on inter-arrival time, which can remove potentially shattered particles. Some of the previously retrieved particle size data needs to be revisited in the light of these findings.

In addition, imaging probes are limited by the resolution limit of the optics they use. The probes cannot usually image very small ice crystals or their mesoscopic surface structures (Schmitt and Heymsfield (2007), Connolly et al. (2007)).

The small ice detector family of cloud probes, the Small Ice Detector Mark-2 (SID-2) and Mark-3 (SID-3) developed in our group at UH[1] (Kaye et al. (2008), Cotton et al. (2009)), is largely free from this limitation. It records the light scattering patterns of particles instead of images, and so is not limited in the same way by the wavelength of the laser used. An intensified charge-coupled device (CCD) camera collects light scattering patterns scattered from particles in an open sampling volume for forward angles of 6° to 25° in an annular shape (<6° a laser beam stop limits the recording). Scattering patterns are captured at a rate

[1] University of Hertfordshire

of up to ≈30 frames/s and particle size histograms collected every second, based on sampling scattering intensities at rates that can be higher than 5 K particles per second.

Although a direct retrieval of the crystal shape is not possible, as the inversion of scattering pattern into a geometrical shape cannot be solved unambiguously, the scattering patterns represent the main characteristics that need to be known. Using this novel cloud probe, recent in-cloud measurements during the CONSTRAIN campaign have shown that most of the ice crystals encountered could be classified as rough (Ulanowski et al. (2014)). The recorded light scattering patterns indicate the presence of a fine structure on the surface of observed crystals or complex overal geometries, which leads to the formation of light speckle patterns.

Recent satellite based observation using PARASOL (Polarization and Anisotropy of Reflectances for Atmospheric Sciences coupled with Observations from a Lidar) find roughness in observation from all latitudes, with higher incidence of rough particles in the tropics (Cole et al. (2014)).

Neshyba et al. (2013) suggest that photographs of falling ice at the South Pole Station in Walden et al. (2003) "are suggestive of trans-prismatic roughening on the exterior prismatic surfaces of hexagonal crystals", as a direct in-situ evidence.

Other evidence has been presented by Shcherbakov et al. (2006a) and Shcherbakov et al. (2006b), who measured ice crystals by combining a polar nephelometer, which records angle dependent light scattering properties, with a cloud imaging probe, further to the evidence found in laboratory experiments.

1.3.1 Aerosol Chambers and Flow Tubes

Aerosol chambers and flow tubes are the best available experimental setups to investigate atmospheric processes. They can be physically large and have means of controlling humidity, temperatures, pressures and vapour supersaturation. Instrumentation to monitor these parameters as well as means to introduce trace gases, additional aerosols or particles form part of these experiments. Examples are the Manchester Ice Cloud Chamber (MICC), the cloud simulation chamber Aerosol Interaction and Dynamics in the Atmosphere (AIDA), a 84 m^3 volume large vessel for cloud related experiments (Möhler et al. (2006)) or the

Leipzig Aerosol Cloud Interaction Simulator (LACIS), which is a thermostated laminar flow tube with a length of up to 10 m and residence times up to 60 s (Stratmann et al. (2004) Hartmann et al. (2011)) or CLOUD (Cosmic Leaving Outdoors Droplet) a more recent facility at CERN with a volume of 26.1 m^3(Kirkby et al. (2011); Almeida et al. (2013)).

In experiments done in the AIDA cloud chamber, and using a laboratory version of the small ice detector instrument, showed that growth conditions with high supersaturation are connected to the formation of rough and complex crystals (Ulanowski et al. (2014), personal communication). Highly supersaturated regions have been found in cirrus (e.g. Gierens et al. (2000), Spichtinger et al. (2003)).

In experiments using a laminar flow tube design based on LACIS and a laboratory version of the SID-3 (also known in its laboratory version as the Particle Phase Discriminator or PPD) with an added optical microscope, ice crystals are grown from a single ice nucleus attached to a fine glass fibre in varying thermodynamic conditions. Optical microscopy images and light scattering patterns are recorded and analysed to obtain crystal size and roughness as described in Ulanowski et al. (2012). The experiments find correlations of ice crystal growth rates with a higher surface roughness. In addition, repeated growth-sublimation cycles have an impact on the development of roughness (Chou et al. in preparation, Voigtlaender et al. (2014)). The latter finding is relevant as in cirrus clouds the conditions, especially saturations, can vary. Krämer et al. (2009) for example find that supersaturations with respect to ice vary from sub- to supersaturated within cirrus clouds and high resolution cloud models predict particle trajectories that cycle repeatedly through sub- and supersaturated regions (Flossmann and Wobrock (2010)).

1.3.2 Halos

Halos appear when the geometric shape of ice crystals in an ice cloud refract light in a regular way due to the presence of a particular shape of crystal. The most commonly observed halo is a ring around the light source (typically the sun or the moon) at a distance of 22° from the viewing direction, and is caused by the hexagonal geometry of the ice crystals (Sassen et al. (1994), Sassen et al. (2003)). If plate crystals are aligned by the air drag force when falling towards the

ground, they can additionally cause bright spots (parhelia) at the 9 and 3 o'clock positions. These effects can easily be reproduced with a computational geometric optics treatment, such as the framework proposed by Tape and Können (1999), but for a more complete description and better description of intensities, diffraction must be taken into account (Berry (1994)). Observations of diversions from the commonly observed patterns has given clues to the shapes and compositions of the ice crystals (Neiman (1989)). Observed halos with an angle of 27.46° for example indicate the presence of atmospheric cubic ice (Riikonen et al. (2000) or Whalley (1981)). Shcherbakov (2013) investigates why a 46° halo that is expected to occur conjointly with the 22° one, occurs far less often and finds that if roughness is added to the raytracing code by Macke et al. (1996), the 46° is lost, because the phase function becomes smooth in this region. Developed roughness could be an explanation for the relative rarety of ice halos (Ulanowski (2005), Ulanowski et al. (2006),Yang and Liou (1998)).

1.3.3 Ice Analogues

Ice analogues are crystals grown from sodium fluorosilicate, they are grown into hexagonal prisms with similar shapes and aspect ratios, as hexagonal ice crystals (Ulanowski et al. (2003), Ulanowski (2005)). Their advantage is that they are solid at room temperature, together with their nearly identical refractive index to ice they are well suited for studies investigating scattering properties of single crystals or as a standard for instrument calibration (Connolly et al. (2007)). Early experiments using an electrodynamic balance to levitate the particles have shown that the asymmetry factor (equation 1.1) of smooth and rough analogue ice crystals can be 0.8 and 0.63, respectively in the visible spectrum (Ulanowski et al. (2006)). This would translate into twice as much backscattering for the rough particles, implying significant impact on cloud radiative properties and forcing.

1.4 Rough Surface Formation

The formation of surface microstructures on the ice surface is a consequence of the molecule kinetics on and the environment near the surface, but it is also affected by the bulk lattice structures and in many cases the processes are

happening at thermodynamical states that are far away from an equilibrium and, for water ice are unfortunately not very well understood at the molecular level.

The gas-ice interface system is further complicated by the presence of a disordered ice (DI) layer, which forms at the interface between the ordered bulk lattice and the vapour phase. The thickness is believed to be between 0.5-100 nm (Bartels-Rausch et al. (2012)), but questions remain unanswered as the reported thicknesses depend strongly on the experimental or computational methods. There is agreement though, that: the structure of the interface layer is different from a supercooled liquid phase; the structure is important for chemical reactions and adsorption and uptake of other atoms or molecules; and is also important by changing the mobility of water molecules residing inside the layer and thereby overall affecting the growth and sublimation kinetics of crystals (Bartels-Rausch et al. (2014)). Key questions, such as: does the layer extend evenly along the air-ice interface, or, how does the thickness depend on the temperature, remain currently unanswered.

There is experimental evidence that the layer affects the roughening transition (Elbaum (1991), Elbaum and Wettlaufer (1993), Maruyama et al. (1999), Dash et al. (1995), Sazaki et al. (2010) , Voss et al. (2005), Henson et al. (2005)). One key problem is to establish how exactly the melting process is connected to the roughening of the surfaces (Furukawa and Wettlaufer (2007)).

The other question is how the processes at molecular level are related to macroscopic effects, which have been observed by optical methods, scanning tunnelling microscopy and cryo SEM studies (e.g. Domine et al. (2003), Rango et al. (1996), Rango et al. (2003), Wergin et al. (2002), Zimmermann et al. (2007)). From investigating water ice using SEM techniques one can summarize the suggestions for formation of roughness as follows.

1.4.1 Sublimation

Several observations of rich surface structures after a crystal sublimation process have been made (e.g. Cross (1969, 1971), Chen and Baker (2009), Waller et al. (2005), Nelson (1998)). The exact mechanisms remain unclear, but a large difference of the environmental pressure to the vapour pressure of the ice leads to fast sublimation. In this process molecules detach from all locations of the bulk crystals, especially also from flat surfaces and not only from the edges,

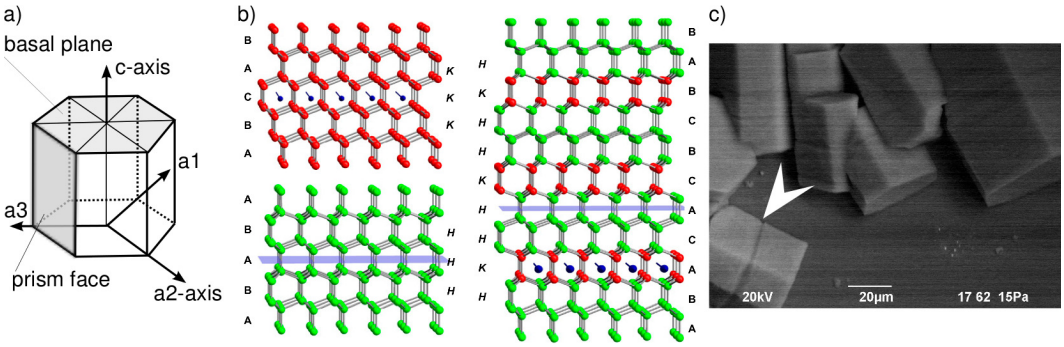

Figure 1.4 – a) Main crystal axis for hexagonal ice lattice. b) Ball-and-stick model with oxygen atoms shown, connected with hydrogen bonds. Pure hexagonal stacking (lower left) and cubic (upper right) of ice and a stacking sequence with fault. Letters H and K denote local sequences of hexagonal (H) and cubic (K) sequences, defined by a mirror plane: layers surrounded by two identical layers (ABA for example) denote an H sequence. Example of a stacking disorder sequence (right). c) SEM image of a water ice crystal with a kink (denoted by white arrow). Middle figure from Kuhs et al. (2012).

leading to relatively homogeneous roughness of the crystals on all facets.

1.4.2 Impurities

Several authors suggest that solutes, such as NaCl or sulphuric acid, as well as small insoluble dust particles in the crystals may be the underlying cause for the macroscopic structures that develop during sublimation (Cross (1969, 1971), Rosenthal et al. (2007), Mulvaney et al. (1988), Barnes et al. (2002), Cullen and Baker (2001)).

1.4.3 Stacking Faults

Using x-ray diffraction Malkin et al. (2012) demonstrated that ice crystallized from supercooled water is disordered in one direction (c-axis) containing layer stacking 'faults', with neither exclusively cubic (I_c) or hexagonal (I_h) structure. Stacking faults are departures from the normal layer stacking arrangement along the c-axis of the crystal, which is ABABAB in the case of I_h, and ABCABC for cubic ice. A stacking disordered ice will contain sequences such as ABACACBCBAB (Kuhs et al. (2012)). Hexagonal ice is the more stable configuration at warmer temperatures and I_c relaxes into the I_h configuration

after several hours. Using neutron diffraction Kuhs et al. (2004) find that above 240 °K (-33 °C) all stacking faults are lost.

This could be the mechanism that leads to the observed kinks (see figure 1.4) and stripy roughness seen on hexagonal columns, which are also reported in Neshyba et al. (2013) and Pfalzgraff et al. (2010). A change in the attachment kinetics at these layers would change the vapour pressure or equally the energy needed for a molecule to leave or attach to the bulk at this location.

Murphy and Koop (2005) estimate the vapour pressure of I_c to be 3-10% higher than the vapour pressure of I_h at 200 °K, which broadly agrees with measurements from Shilling et al. (2006) who find the values to be around 10% higher for their measurements. If one considers this difference during sublimation at these locations molecules detach more easily.

This is especially important as it might be possible that a substantial part of the atmospheric ice is not pure hexagonal ice. Moore and Molinero (2011) conducted a molecular dynamics (MD) simulation of freezing from liquid at 180 °K and found that the ice contains a 2:1 ratio (volume) of cubic to hexagonal ice.

1.4.4 Growth

There have been a great many experiments and efforts to describe and investigate ice crystal growth from the vapour phase in a small scale (as compared to large cloud or flow chamber experiments). Most of them have used optical microscopy for imaging and therefore cannot resolve very fine structures. Some of this work was done by Kuroda and Gonda (1984), Nelson and Knight (1996), Kuroda (1984), Gonda and Yamazaki (1982) and Kobayashi and Higuchi (1957), as well as by Lamb and Hobbs (1971), Nelson and Knight (1996) and Libbrecht and Morrison (2008).

Fukuta and Takahashi (1999) find asymmetries of freezing droplets as they fall through a vertical fall tube. The downward, in fall direction pointing sides of the spheres, show clear additional rough structures.

Other experiments concerning thin films of water and imaging in these experiments rely on scanning tunnelling microscopy, such as the work from Thürmer and Bartelt (2008), who discuss screw dislocation developing into macroscopic features.

Lakhtakia and Messier (2005) and Cartwright et al. (2008) used environmental SEM (ESEM) to investigate ice films grown from the vapour phase at temperatures down to 6 °K and low pressures, corresponding to astrophysical conditions. They identify five zones, occupying the temperature, pressure space: a porous morphology with tapered columns and voids with cauliflower shapes, a matchstick morphology with parallel columns and domed tops, a transition zone with no long range structure, a columnar crystalline grain structure and a re-crystallized crystalline structure.

1.5 Research Questions

The experimental setup I developed is designed to study surface morphology development of small water ice crystals at temperatures and pressures relevant to atmospheric ice. Experiments using this setup investigate the effect of changes in water vapour supersaturation, pressure and temperature on the growth and sublimation of small ice crystals. The questions that I investigated are:

- which changes in environmental parameters cause development of surface roughness,
- what is the structure of the roughness,
- does fast growth lead to formation of roughness or complex crystals,
- what is the effect of sublimation on surface morphology,
- what is the effect of repeated growth and sublimation cycles, i.e. is there an influence of growth history on crystal morphology

Chapter 2

Methods

In the following section I will outline the experimental setup and the preparatory procedures I developed to investigate the growth of small water ice crystals. This includes a description of instruments used, electronics and data acquisition software I developed and materials and protocols used for the preparation of samples and growth surfaces.

2.1 Experimental Setup Overview

The main component of the setup is a small diffusion chamber, which is placed inside the specimen vacuum chamber of a scanning electron microscope (jcm-5700, JEOL[1], JP). Additional signal conditioning and control electronics to measure and set temperatures and pressures are located outside the vacuum and complemented with software running on a micro controller and a personal desktop computer (PC).

A commercial Peltier based thermoelectric cold stage (Ultracool, Deben, UK) is mounted on the XYZ-platform of the SEM tray and forms the base and main mechanical support for the small diffusion chamber (figure 2.1 and 2.8). The cold stage can cool specimens to a temperature of -49 °C when supplemented with an additional chiller bath and is typically used to reduce vapour pressures in specimens containing water or other liquids, such as biological cells, for imaging in low vacuum conditions. Here it is used to control the temperature of the small

[1] Japan Electron Optics Laboratory

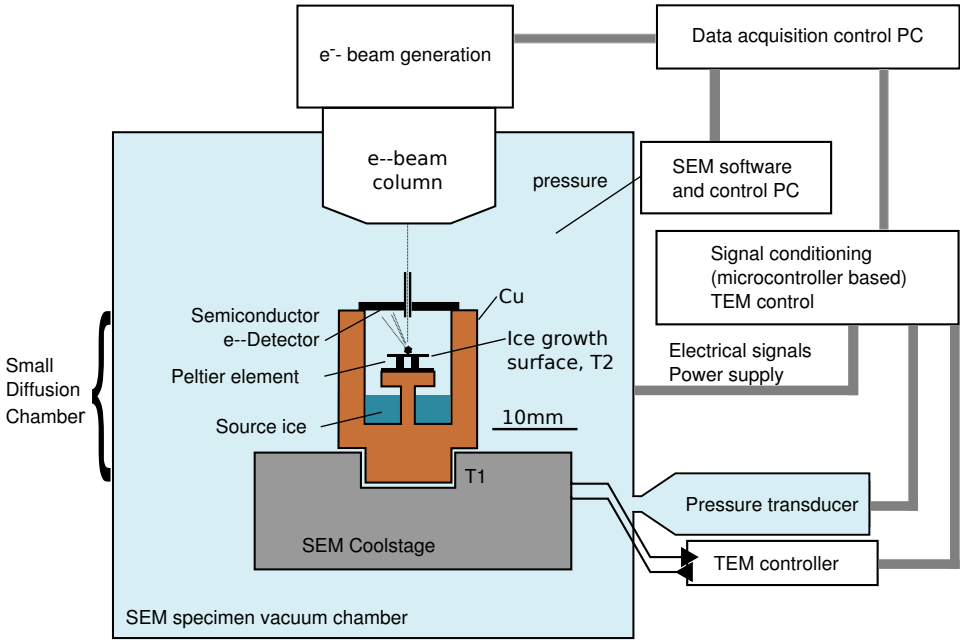

Figure 2.1 – Schematic of the experimental setup inside the vacuum chamber of a scanning electron microscope (SEM). A small diffusion chamber is mounted on a water cooled Peltier based thermoelectric element (TEM). The cold ice growth surface is provided by an additional, second, small Peltier element. A back scattered e^-–detector, with an entry hole for the electron beam, forms the top of the diffusion chamber.

diffusion chamber. All required connections into the vacuum environment are made through a vacuum feed-through situated on the stage tray.

The small diffusion chamber is fitted on top of the first cold stage. A back scattered electron detector (BSE) forms the top and closes the chamber. The detector element (custom design, Centronic, UK) has an ≈0.5 mm diameter hole to allow the scanning electron beam to enter the diffusion chamber and reach the ice growth surface. The back scattered electrons then reach the detector element inside the small chamber, which is mounted on anXY-platform to allow the position of the beam entry hole with respect to the ice growth surface to be adjusted.

Temperatures, pressures and imaging are managed by the data acquisition and control system (DACS) outside the vacuum chamber. This consists of three parts: a micro controller based circuit, a software client extending the SEM software interface and a standard desktop computer.

The different sub systems of this setup are described in detail in their respective

sections below.

2.2 Environmental Scanning Electron Microscopy

Scanning electron microscopy (SEM) was chosen as the imaging method. By scanning a narrowly focused electron beam across the target and collecting the 'reflected' electrons for image formation, fine details at a resolution which is far greater than could be achieved using optical methods can be observed: The wavelength of $\lambda_\nu = 400\,nm$ for light compares to the equivalent de'Broglie wavelength ($\lambda = h\,p^{-1}$) of a 20 keV electron which is: $\lambda_e = 0.0086\,nm$ and isobtained as follows:

$$\lambda = \frac{h}{p} = \frac{h}{m_e v} \tag{2.1}$$

$$E = qU = \frac{1}{2} m_e v^2 \tag{2.2}$$

v after the electron has passed the acceleration field,

$$v = \sqrt{\frac{2qU}{m_e}} \tag{2.3}$$

and

$$\lambda_e = \frac{h}{\sqrt{2 m_e q U}} \tag{2.4}$$

U acceleration voltage, q_e electron charge[2], m_e electron rest mass[3], h Planck's constant[4], c speed of light[5] neglecting relativistic effects.

Typically, a high vacuum environment (10^{-5} to 10^{-7} Pa) is necessary, to allow the electron beam to reach the target, and specimens need to be coated to be electrically conducting, so any charge deposited by the imaging beam into the specimen can flow off. Strong electric fields build up otherwise and deflect the beam electrons away from the target, which distorts the generated image. A high

[2] q_e=1.602 10^{-19}C
[3] m_e=9.109 10^{-31}kg
[4] h=6.63 10^{-34}m^{2}kg s^{-1}
[5] c=2.998 10^{8}m s^{-1}

vacuum environment however is unsuitable for water ice at most temperatures except very low ones; water ice reaches a vapour pressure of 10^{-5} Pa only at -112 °C. For the temperature ranges of interest (above -80 °C), the water vapour pressure is orders of magnitudes higher. In addition, it would require cooling with liquid nitrogen or similar methods to reach the low temperatures, which would complicate the experimental setup.

Environmental scanning electron microscopy (ESEM) is an extension of the conventional scanning electron microscopy pioneered by Ernst Ruska in 1931[6]. The method makes it possible to image specimens at low vacuum conditions by separating the high vacuum in the electron beam column from a low vacuum in the specimen chamber by one or several pressure limiting apertures. Various variants and commercial implementations have been available since the 1970s (Stokes (2012)) and imaging has been demonstrated up to 2.7 kPa (Danilatos (1988)).

Although the presence of a gas inside the specimen chamber reduces the mean free path of the beam electrons, the scattering does not dramatically affect the focusing behaviour and the path length. It mainly reduces the beam current slightly and adds a slight blurring to the image, as the scattered electrons form a skirt around the main beam.

Thiel et al. (1997) investigated electron transport behaviour for ESEM application using Monte Carlo simulation and experiments and provide mean free path data for the primary electrons in water vapour, based on

$$l_{mfp} = \frac{k_B T}{\sigma P} \tag{2.5}$$

with T temperature, P pressure, k_B the Boltzmann constant[7], σ the electron–gas scattering cross section. The authors rely on literature values for the cross sections for different electron beam energies; numerical values are given in table 2.1.

The fraction of unscattered electrons for a gas at pressure P is computed using the Beer-Lambert relation:

[6] Nobel Prize in Physics 1986 for 'his fundamental work in electron optics and for the design of the first electron microscope', together with Gerd Binnig and Heinrich Rohrer 'for their design of the scanning tunnelling microscope'.

[7] $k_B = 1.38\,10^{-23}$ J K^{-1}

		Mean Free Path (mm)				
keV	σ(Å^2)	1 Pa	10 Pa	100 Pa	1 kPa	$f_{2\,mm}$@100 Pa
0.5	2.51	163	16.4	1.6	0.16	16%
1	1.45	284	28.8	2.8	0.28	34%
2	0.80	513	51.3	5.1	0.51	56%
5	0.36	1144	114.3	11.4	1.14	77%
10	0.20	2122	212.2	21.2	2.12	87%
20	0.10	3932	393.2	39.3	3.93	93%

Table 2.1 – The mean free path of electrons (in mm) in water vapour for different pressures and electron energies, cross section of the interactions and the fractions of electrons remaining after a travel distance of 2 mm through gaseous environment (Thiel (2001)).

$$f \propto e^{\frac{-\sigma L P}{k_b T}} \tag{2.6}$$

L distance travelled, f fraction of the electrons not scattered. The values given in table 2.1 demonstrate that for the higher accelerating voltages the path length is several 100 millimetres and the fraction of electrons that are scattered out of the beam is small.

Besides being able to image non conducting specimens containing high vapour pressure materials, the advantage of having a gas present in the imaging chamber is that excess charge building up in the specimens is neutralized by the gas, which becomes ionized. This allows specimens to be imaged that are not coated with an electrically conducting layer such as carbon or gold, which are frequently used in sample preparation.

Various gases have been investigated as an imaging gas, using it to amplify the imaging signal through a charge avalanche cascade effect. In an additional external electrical field at the detector, back scattered electrons ionize molecules of the imaging gas, which in turn are accelerated and create multiple new ions. The amount of ion delivered charge is recorded at a target electrode and is used as the imaging signal. Water vapour has been found to be very efficient (Fletcher et al. (1997)) due to its ionization properties (Thiel et al. (1997), Biagi (1999)).

This ion production is also an unwanted effect when studying ice growth: During my experiments I found a series of unexpected growth behaviours, such as needle formation and rectangular wall build ups. They can be attributed to

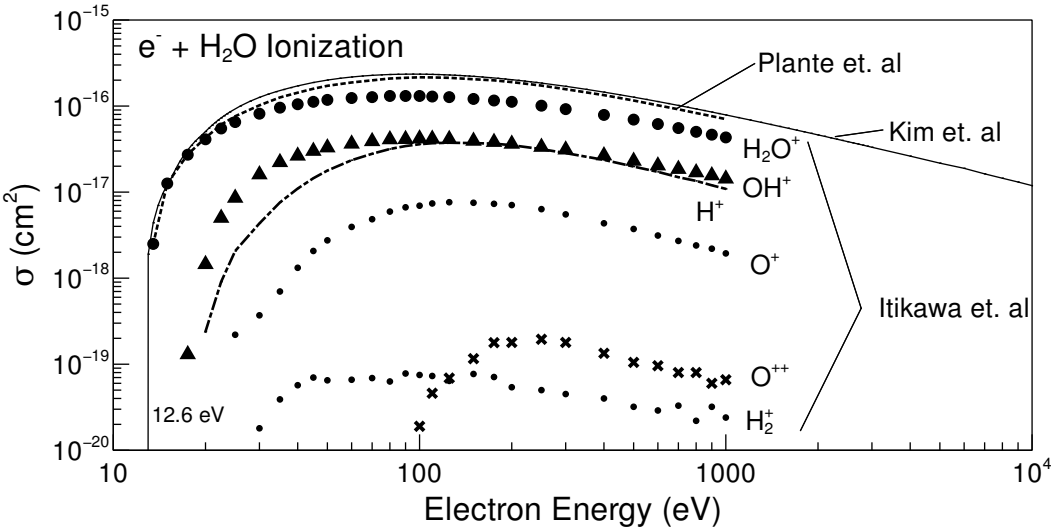

Figure 2.2 – Ionization cross section for electron-H_2O collision. Data from Kim and Rudd (1994), available via Kim and Koo (2005), Plante and Cucinotta (2009) and partial cross sections for different channels from Itikawa and Mason (2005).

changes in the electric fields through charging at the specimens, and also to the formation of ions from electron-H_2O collisions (see section 3.2). Electrical surface charge of ice crystals is also known to be affected by growth and sublimation rates (Dash and Wettlaufer (2003), Saunders (2008)).

The ionization cross sections for ion production on electron-H_2O collisions are summarized in figure 2.2. The energy threshold for ionization of an H_2O molecule to occur is 12.6 eV. Further to the listed ionization pathways (channels), dissociative attachment leads to the production of O^- and OH^-, but cross sections are low. Energy transfer in the form of elastic scattering, excitation with subsequent emission of a photon and energy transfer into vibrational and rotational states of the H_2O molecule occur as well but do not create free ions. The low ionization threshold means that ionization in the presence of the imaging beam is inevitable. And because the water ions change the attachment of molecules to the bulk material, they can affect the growth of ice crystals substantially. As this effect is unwanted I avoided this by only using the electron beam for image acquisition and disabling it all other times.

The energy distributions of the backscattered electrons are examined in a study from Yadav and Shanker (2007) and Matsukawa et al. (1974) for different bulk materials. An analytic expression (equation 2.8) for the backscatter coefficient with dependence on the atomic number (Z) is given by Staub (1994), being in

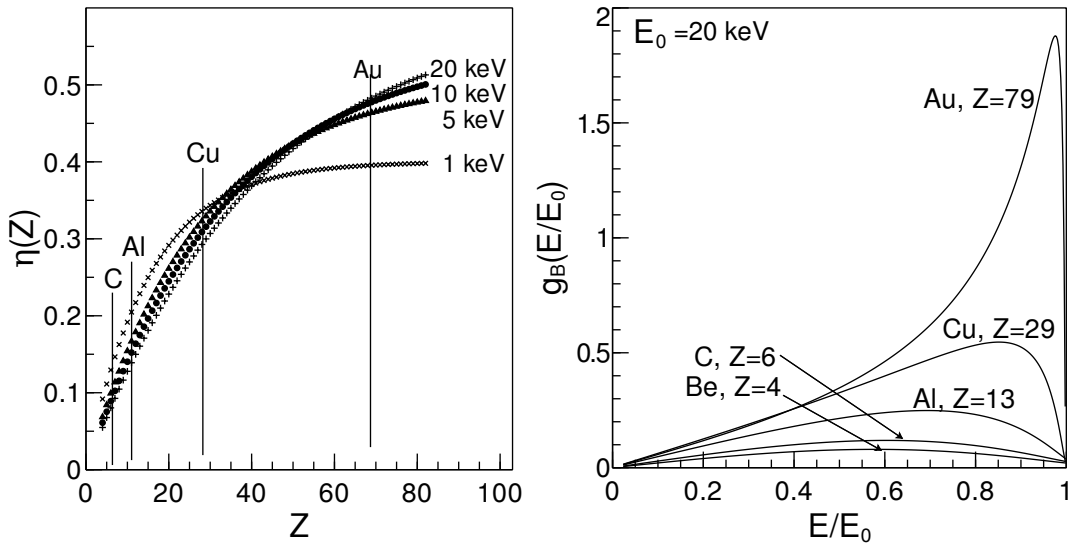

Figure 2.3 – Fraction of back scattered electrons (backscatter coefficient η) for different incident beam energies (left). Back scattered electron energy distribution for a 20 keV (E_0) incident beam with orthogonal angle ($\Theta = 0$) into different bulk materials: Be, C, Al, Cu, Au (right) using expressions given in Staub (1994). Beryllium (Be) is close to the suggested Z_{eff} of water ice.

good agreement with experimental data for $0.5 \leq E_0 \leq 30\,keV$, for $Z \geq 4$ and incident beam angle $0 \leq \Theta \leq \frac{\pi}{3}$, with

$$\beta = 0.40 + 0.065\,ln(E_0) \tag{2.7}$$

$$B_0 = \eta = \beta\,[1 - exp(-6.6 \times 10^{-3}\beta^{\frac{-5}{2}}\,Z] \tag{2.8}$$

E_0 (keV) incident electron energy, Z atomic number (left figure of 2.3). Staub (1994) also gives an expression for the energy distribution of the back scattered electrons, which he finds to be in 'reasonable' agreement with measurements.

$$g(E/E_0) = -\frac{\partial\eta(E/E_0)}{\partial E} \tag{2.9}$$

$$\eta(E/E_0) = S\,exp\left[-\left(\frac{K}{1-\gamma(E/E_0)^{\alpha}}\right)^{p}\right] \tag{2.10}$$

$\eta(E/E_0)$ fraction of electrons with energies greater than E after interaction, Θ angle of the incident beam, $\kappa, \alpha, p, \gamma, S, K$ parameters that are determined solely from the backscatter coefficient B_Θ as follows:

$$\kappa = 1 - exp(-1.83\, {E_0}^{1/4}) \tag{2.11}$$

$$B_\Theta = {B_0}^{(1-\kappa(1-cos\,\Theta))} \tag{2.12}$$

$$K = 70\,|ln\,B_\Theta|^4 \tag{2.13}$$

$$\gamma = 1 - exp(-6\,|ln\,B_\Theta|^{-3/2}) \tag{2.14}$$

$$S = B\,exp(K^p) \tag{2.15}$$

$$p = 0.27, \quad \alpha = 2.0 \tag{2.16}$$

The atomic number of beryllium ($Z = 4$) is the smallest Z for which the expression (2.10) is valid and is also close to the improved effective atomic number for water ice of $Z_{eff} = 3.4$ (Taylor et al. (2012), p. 1776), which is an improvement upon the frequently used $Z_{eff} = 7.68$ given by Mayneord (1937). The backscattered electron signal yield is small for low Z elements and the energies of the backscattered electrons is distributed across the energy range, with a maximum at $0.58\,E_0$ (figure 2.3). This makes imaging more difficult.

For investigating the penetration depth of the electron beam into the specimen, the definition of the mass-range (Kanaya and Okayama (1972), eq. 9) is widely used in the scanning electron microscopy literature. The equation gives an estimate of the interaction volume radius, with

$$R = \frac{5.025 \times 10^{-14}\, A\, E^{\frac{5}{3}}}{\lambda_S\, Z^{\frac{8}{9}} \rho} \tag{2.17}$$

R (m) radius of hemisphere, A (g mol^{-1}) atomic weight, Z atomic number, ρ (g cm^{-3}) density of the bulk material and E (eV) beam energy. Using the provided $\lambda_S = 0.182$ and Taylor's Z_{eff} for H_2O, the result for water ice ($\rho = 0.92$ g cm^{-3}) for a 20 keV beam is ≈27 µm and ≈8.4 µm for a 10 keV beam. This is higher than the results from Barnett et al. (2012) who give an estimate of ≈2 µm for a 10 keV

beam based on Monte Carlo scattering simulations (CASINO[8] code, Drouin et al. (2007)). The authors compared their values with experiments, in which they found that the simulations underestimate the depth and are not very accurate for low energy electrons (<2 keV) that do not pass through an ice layer thicker than 300 nm.

The JEOL jcm-5700 Carryscope has a maximum imaging magnification of $300\,000\times$, a specified resolution of 5 nm — which can only be achieved for certain sample materials and under ideal conditions in high vacuum using the secondary electron (SE) detector for imaging. Further, the SEM is equipped with a multi segment silicon back scattered electron (BSE) detector. The details of the low vacuum system of the jcm-5700 are described in detail in the next section on the vacuum system (section 2.3).

During normal operation the SEM is operated from a desktop computer and communicates via a custom electronic bus interface. A standard video signal frame grabber is used to read images generated by the scanning beam, into the computer and some of the post processing such as averaging is performed in the digital domain. The XY electron beam scanning signals with different timings for the different video modes are generated by a scanning pattern generator inside the microscope electronic. Beam location can alternatively be controlled externally by supplying an analogue X and a Y signal — similar to an oscilloscope in XY-mode. This interface is used for the simultaneous multi-signal readout I developed and is described in the section on 3D surface reconstruction (section 2.18). There is no electronic input to control beam blanking, the beam can only be switched on or off using the software client.

To allow pressure changes and image acquisition to be controlled from an external experiment control software, I extended the SEM client software with a network socket interface that can receive pressure set and 'acquire image' commands via a network port (figure 2.4).

2.3 Vacuum System

The microscope provides two vacuum modes for imaging: a high vacuum ($\approx 10^{-4}$ Pa) and a low vacuum with a specified range from 1-100 Pa.

[8] www.gel.usherb.ca/casino

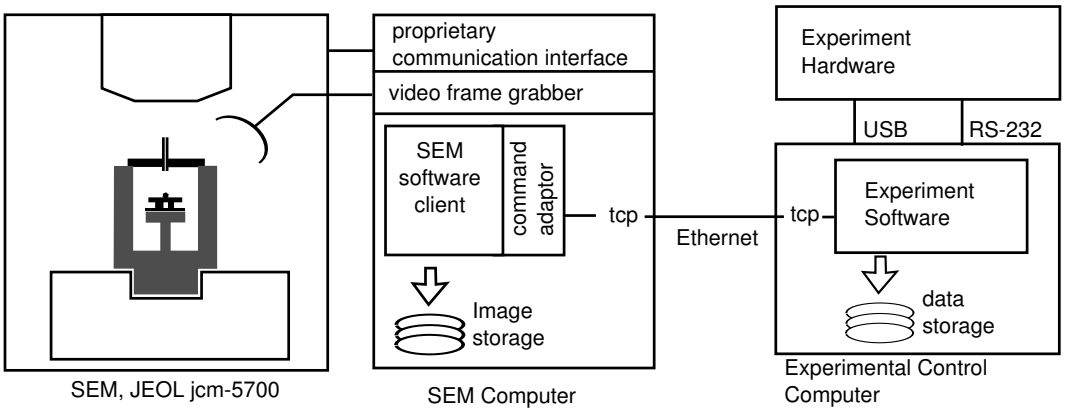

Figure 2.4 – A standard windows PC runs the SEM interface (middle), the SEM is connected via a custom bus to the computer, a standard video frame grabber digitizes the analogue image signal. The SEM client is instrumented to receive control commands via a network socket, they are issued from a second experiment control PC (right) that also stores data.

A schematic of the vacuum system is shown in figure 2.5; non essential valves and bypasses are omitted: two pumps, a rotary pump (RP) preceding a turbo molecular pump (TMP) maintain a constant pumping rate. A set of valves is used to manage the different flow configurations for the different pumping stages during evacuation and also to reconfigure the system into the two different vacuum modes.

In the low vacuum mode the electron beam column is pumped by the turbo molecular pump and the 6.5 l specimen chamber (Ch) is only pumped by the rotary pump, while the TMP is disconnected from the specimen chamber. The resulting pressure difference between the beam column and the main chamber is maintained by the aperture and a sectioned beam column.

To regulate the pressure in the specimen chamber a motorized needle valve (V6) bleeds ambient air into the system and the pressure in the specimen chamber is controlled by changing the amount of air inflow. An internal digital algorithm links the pressure readings from a sensor (Pi1), measuring the specimen chamber pressure, with the commands to the servo valve (V6).

In the low vacuum configuration any gas that enters through V6 is immediately removed by the pumping system. This made my early attempt to introduce water vapour into the specimen chamber via this pathway unsuccessful. I subsequently decided to use ice itself as a water vapour source, and designed a diffusion chamber which can reside inside the specimen chamber of the microscope.

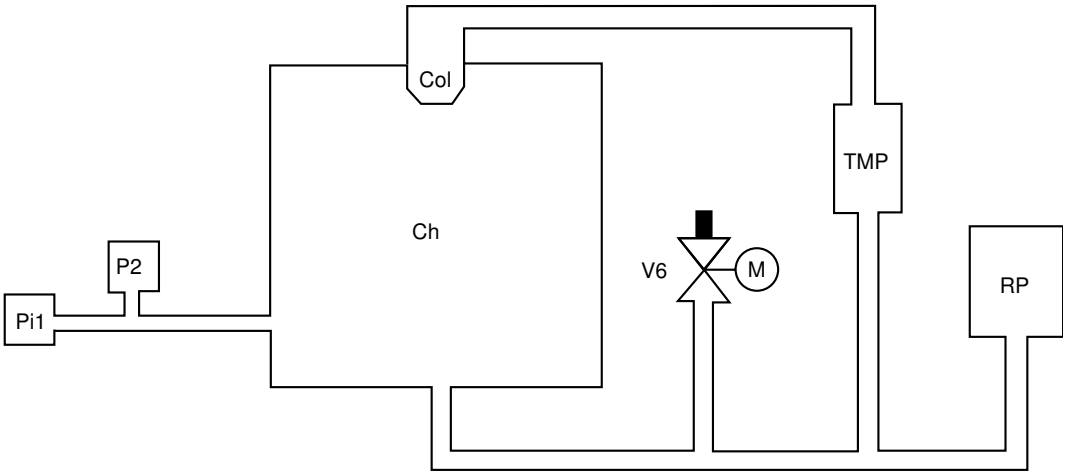

Figure 2.5 – Schematic of the vacuum system of the SEM (adapted and only relevant components are shown for the low vacuum (LV) configuration). The specimen chamber (Ch) is pumped by a rotary pump (RP), a turbo molecular pump (TMP) maintains the high vacuum in the electron beam column (Col). The pressure sensor (Pi1), a Pirani gauge, is part of a closed loop system controlling a servo valve (V6) that bleeds ambient air into the system. P2 is a membrane capacity based second pressure sensor.

The microscope's own pressure sensor is a Pirani gauge (PSG-1, Diavac, JP), which measures the heat loss of a resistive wire into the gas to derive the pressure. Readings are therefore strongly affected by the presence of water vapour, which results in an overestimation of the pressure value.

As a remedy, I introduced a second sensor (Barocel W655, Edwards, UK) — a high precision capacitance manometer (P2, figure 2.5) — and used it for pressure measurements throughout. This sensor measures the capacitance between a deformable membrane and a counter electrode and is therefore independent of the measured gas. The sensor has been UKAS calibrated (Chell, UK) and has a calibrated maximal deviation of better than $\pm 0.05\%$ over the 20-100 Pa range against the calibration standard. Output format is an 0-10 V analogue signal mapped to the sensor's measurement range of 0-100 Pa. This signal is digitized using a micro controller.

To investigate the response and settling behaviour of the pressure control loop I recorded the responses to a number of pressure change commands and found that the system reaches the set pressure after roughly 200 s in most cases (figure 2.6). Several runs were required to find the response times needed (time until the pressure does not change more than 2% for 60 s or the cut-off time of 300 s is

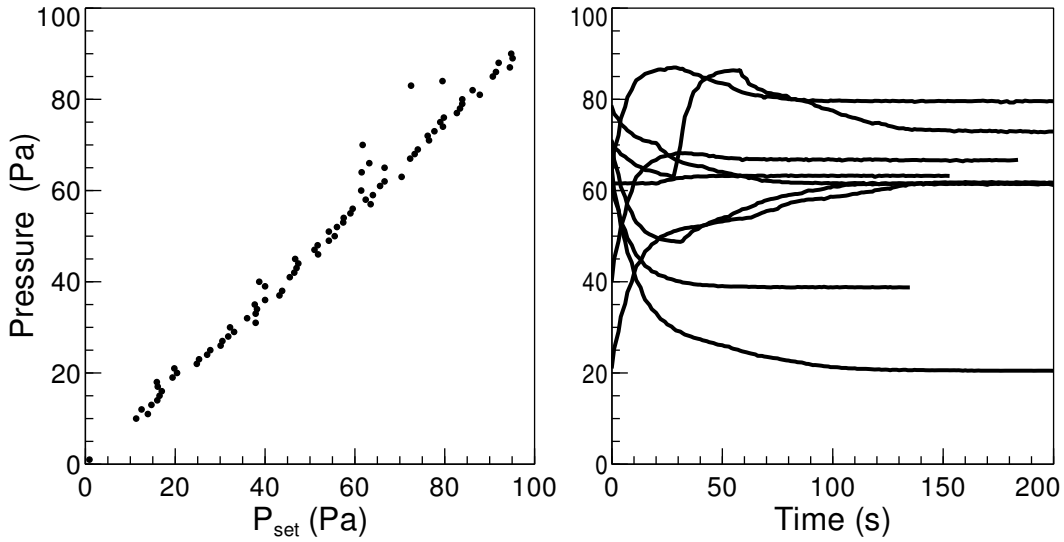

Figure 2.6 – The behaviour of the vacuum control system to external pressure set commands. The settled pressures for a number of changes are recorded and plotted against the pressures, the systems settled on within t<300 s (left). Time response curves for individual different pressure changes (right).

reached; whatever comes first). To understand if there is a time dependence on the pressure step size and if the time depends on the starting pressure (P_{start}), the response time is mapped for random step sizes (figure 2.7). From the distribution of the circle sizes it can be seen that there is no strong dependence on the starting values and the pressure change step size. The pressures were measured with the capacitance manometer and no water vapour was present in the chamber.

If water vapour is present, the internal Pirani gauge overestimates the pressure, and a lookup table derived from my observations is required to find the pressures that need to be set within the SEM software to achieve the desired real pressures. This can be improved by replacing the Pirani pressure signal with a copy of the signal from the capacitance manometer (a 4-40 mA current loop interface), so the microscope control loop receives readings that are not affected by water vapour. Unfortunately, the reported currents from the PSG-1 are non-linear, so linear mapping using a current loop interface such as the AD694 (Analog Devices, US) is not straightforward.

I therefore set the specimen chamber pressure to values (see appendix B.2) that match exactly the water vapour pressures of the source ice by means of an experimentally determined lookup table.

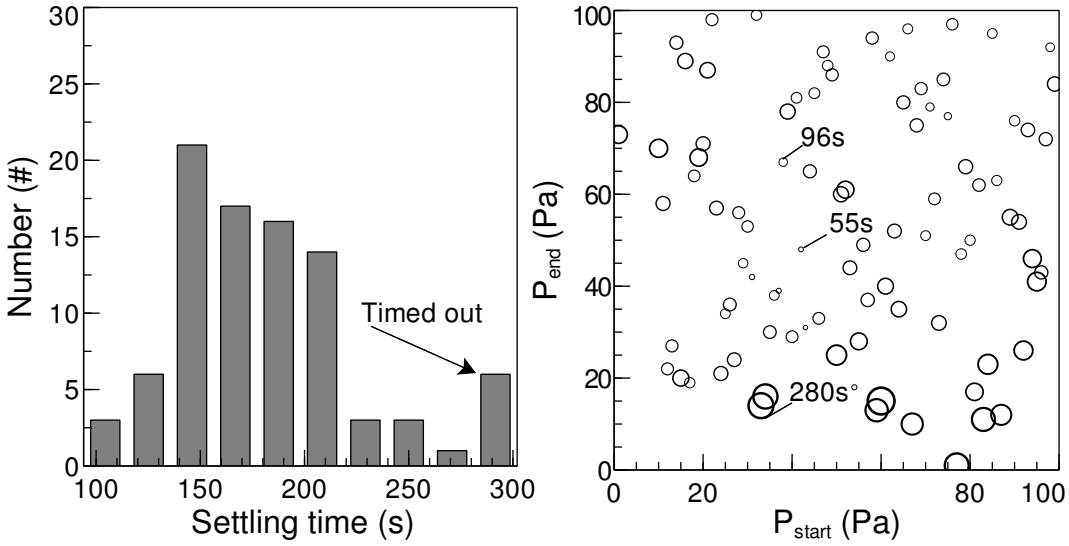

Figure 2.7 – The responses of the vacuum pressure control loop to set pressure commands. The settled pressures: a number of changes are recorded and plotted against the time the system needs settle to within 2% (left). Mapping of the settling time (circle radius) of different pressure changes (P_{start} to P_{end}) (right).

When the pressure outside of the small diffusion chamber is the same as the water vapour pressure inside the chamber, outflow of water vapour into the specimen chamber is minimised and therefore source ice in the small diffusion chamber can be maintained over several hours.

2.4 Diffusion Chamber Design

The main experimental chamber, the small diffusion chamber, is mounted into the 10 mm diameter aluminium support of the main cold stage (figure 2.8) adding a silicon thermal pad to increase thermal contact . This diffusion chamber (≈23 g copper, ≈170 µl chamber volume; $R = 5$ mm, $H = 11$ mm) is closed with a plastic positioning stage carrying a detector element that has an ≈ 0.5 mm opening to allow electron beam entry.

The middle copper support stub, within the small chamber (right, figure 2.9), is used to mount the second Peltier element, which provides the cold ice growth area on its upward ceramic surface. The small amount of excess heat is dissipated, conducted through the copper support and removed by the cold stage, which is how the Peltier element maintains a temperature difference between the diffusion chamber and the ice growth surface when a voltage is

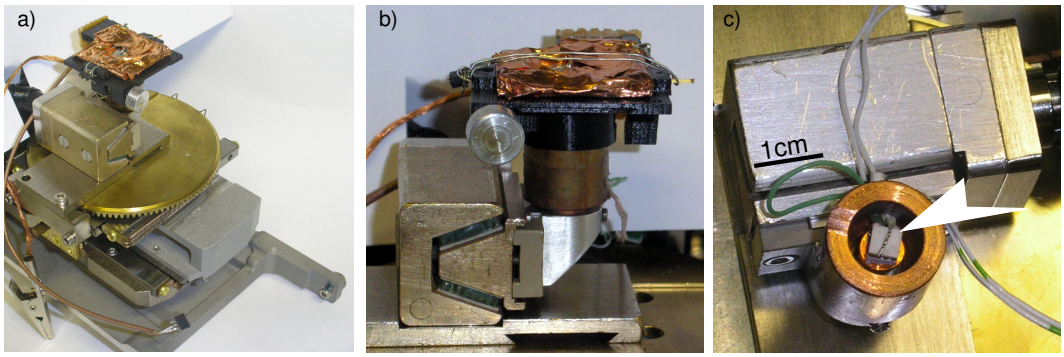

Figure 2.8 – Diffusion chamber installation on the SEM sample tray (a), close-up of the copper chamber mounted onto the cold stage with lid, carrying the detector element (wrapped in Cu) on top (b), view inside the chamber; white arrow marks the ice growth surface (c).

applied. The thermal connection between the Peltier element and the copper stub is made using a thin silicon pad and cyan acrylate adhesive, and manually applying downwards pressure until the glue sets. Other variants of bonds I tried (thermally conducting epoxy for example) did not withstand the changes in temperatures and pressures.

The bottom of the small diffusion chamber holds an amount of ≈ 0.5 ml of ultra pure water (18.2 MOhm cm, Neptune, Purite, UK) which is frozen prior to evacuation of the specimen chamber and is the water vapour source (source ice).

Two thermocouple junctions are used to read the temperature difference between the source ice and the ice growth surface.

Wires for the Peltier power and the thermocouple junctions are routed through a small hole on the side of the chamber which is sealed with a silicone rubber compound. To prevent ice growth inside the small Peltier element, the side is wrapped with a Teflon band.

The top of the chamber is a 3D printed XY-stage I designed (figure 2.8b and left, figure 2.9), and is made of an acrylonitrile butadiene styrene variant (ABS) using this rapid prototyping technique. The three individual parts that form the positioning stage are sealed with a low vapour pressure vacuum grease (M Grease, Apiezon, UK) and hold the electron detector element, which itself is fixed with silicone rubber.

In this setup the ice growth surface can be positioned at a working distance (WD) of about 15 mm (as reported by the microscope's software). The path of the

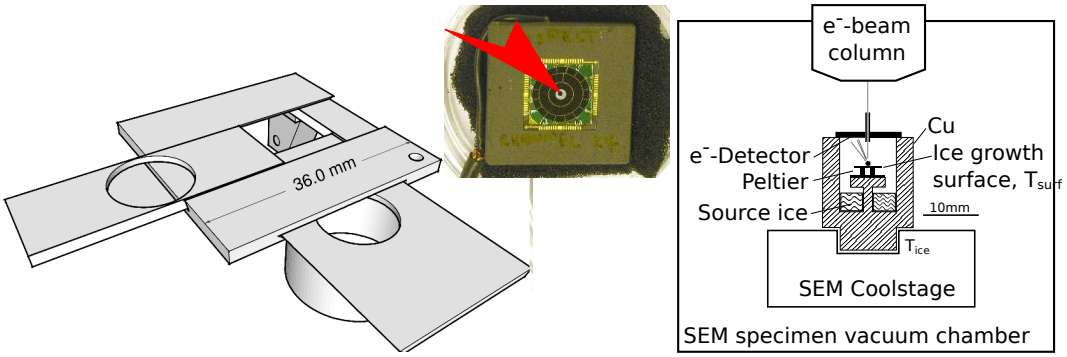

Figure 2.9 – Engineering drawing of the diffusion chamber lid and XY-stage detector mount (left). Custom segmented semiconductor back scattered electron detector on ceramic (right), red arrow marks the hole for electron beam entry.

backscattered electrons is shorter, about 6 mm, because they only need to travel from the ice growth surface back to the custom detector which is inside the small diffusion chamber.

For an experiment the bottom of the diffusion chamber is filled with ultra pure water and the temperature lowered to the desired temperature; after the water has frozen it forms the source ice. The chamber is closed with the detector assembly and the main SEM specimen chamber can be evacuated.

2.5 Water Vapour Diffusion

For a cylindrical chamber, water vapour diffusion is described by the diffusion equation (Crank (1975)) with a constant diffusion coefficient D, for the concentration Φ (g m^{-3}),

$$\frac{\partial}{\partial t}\Phi(t;\rho,\varphi,z) = D\,\triangle_{cyl}\Phi(t;\rho,\varphi,z) \tag{2.18}$$

$$\triangle_{cyl} := \frac{1}{\rho}\frac{\partial}{\partial\rho}\left(\rho\frac{\partial}{\partial\rho}\right) + \frac{1}{\rho^2}\frac{\partial^2}{\partial\varphi^2} + \frac{\partial^2}{\partial z^2} \tag{2.19}$$

and D the diffusion coefficient. Because the ice is frozen on the bottom of the chamber the concentration is only a function of z which reduces the equation to

$$\frac{\partial}{\partial t}\Phi(t,z) = D\frac{\partial^2}{\partial z^2}\Phi(t,z) \tag{2.20}$$

assuming that the source ice keeps the vapour concentration at $z = 0$ constant through outgasing, resulting in the boundary condition

$$\Phi(t, 0) = \Phi_0 \tag{2.21}$$

and using the initial condition of no vapour present in the rest of the diffusion chamber at $t = 0$,

$$\Phi(0, z) = 0, \ z > 0 \tag{2.22}$$

the solution found, using a Laplace transformation for example (Crank (1975), p. 21), is

$$\Phi(t, z) \coloneqq \Phi_0 \, erfc\left(\frac{z}{2\sqrt{Dt}}\right) \tag{2.23}$$

$$erf(z) \coloneqq \frac{2}{\sqrt{\pi}} \int_0^z e^{-\xi^2} d\xi \tag{2.24}$$

$$erfc(z) \coloneqq 1 - erf(z) \tag{2.25}$$

The factor $L_d \coloneqq 2\sqrt{Dt}$ is referred to as diffusion length and is a measure of how far the concentration front has moved along z after time t.

To obtain a numerical value, the diffusion coefficient of water vapour in air is computed using a 2nd order polynomial fit to the values provided by Bolz and Tuve (1973) (p. 545, table 5-46); who give values for $0 \leq T \leq 80$ °C.

$$D(T) \coloneqq -2.7754 \times 10^{-6} + 4.4794 \times 10^{-8} \, T + 1.6558 \times 10^{-10} \, T^2 \tag{2.26}$$

assuming that the relation is valid for temperatures $T < 0$ °C with temperature T in (°K), for a system at -40 °C the diffusion coefficient is
$D(233) = 1.6651 \times 10^{-5}$ m^{2}s^{-1}.

Using this coefficient and times of 1, 4 and 10 seconds results in an $L_d = 5.8, \ 11.5$ and 18.2 mm. This demonstrates that a water vapour concentration change can propagate through the entire chamber ($H = 11$ mm)

in the order of about 4 s by diffusion only.

2.6 Vapour Pressure

The water vapour pressure over ice describes the pressure the water vapour reaches when a closed system of ice and a volume above is in thermodynamic equilibrium at a certain temperature. Comparably, the water vapour pressure over a liquid interface is defined and often referred to as water vapour pressure.

The parametrisation used throughout is based on the Clausius-Clapeyron equation (e.g. Wexler (1977)) but a more recently improved version is available and used here throughout (Murphy and Koop (2005), eq. 7 and 10):

$$P_{ice}(T) = \exp(9.550426 - 5723.265/T + 3.53068\ \ln(T) - \tag{2.27}$$
$$-0.00728332\,T) \tag{2.28}$$

$$P_{liq}(T) = \exp(54.842763 - 6763.22/T - 4.210\ \ln(T) + \tag{2.29}$$
$$+0.000367\,T + \tanh[0.0415 \cdot (T - 218.8)] \cdot (53.878 - \tag{2.30}$$
$$-1331.22/T - 9.44523\ \ln(T) + 0.014025T) \tag{2.31}$$

for $T > 110$ °K (P_{ice}) and $123 < T < 332$ °K (P_{liq}), temperature T in Kelvin and pressure P in Pa (figure 2.10).

There is a small difference in the vapour pressures of ice and (supercooled) water for a given temperature. As a consequence ice can grow at the expense of water droplets if they coexist as for example in mixed phase clouds (the Wegener-Bergeron-Findeisen process).

By moving the temperature of the ice growth surface the supersaturation (Korolev and P. (2003)) is changed. The supersaturation is defined as

$$S = \frac{e - E_s}{E_s} \tag{2.32}$$

where e is the vapour pressure and E_s is the saturation vapour pressure.

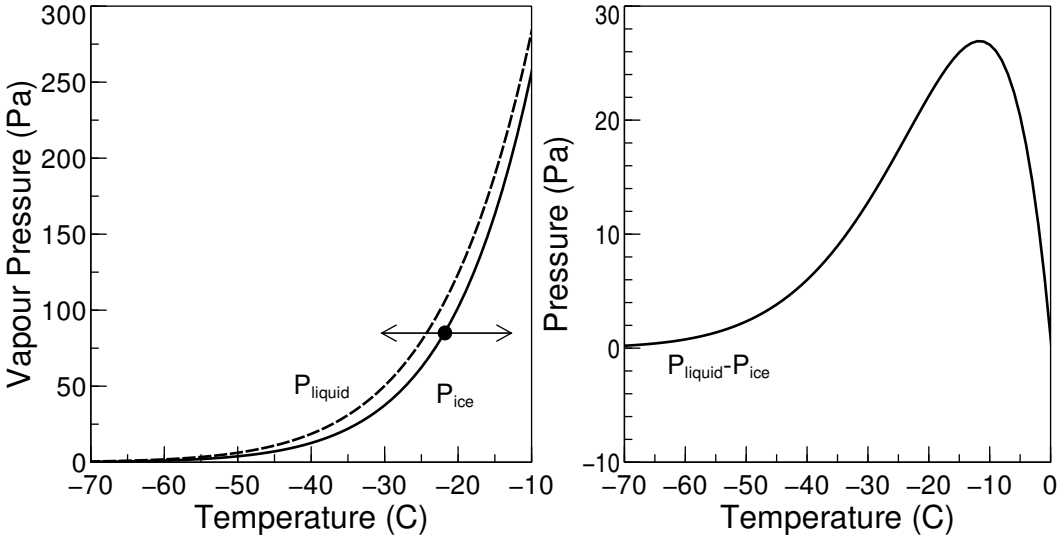

Figure 2.10 – The water vapour pressures for ice and supercool water (left), difference $P_{ice} - P_{liquid}$ (right). The arrow indicates movement of the system (black dot) into supersaturation (←) and subsaturation (→). Murphy and Koop (2005).

Another measure is the saturation ratio defined as

$$S_i = \frac{e}{E_s} \tag{2.33}$$

2.7 Cooling System

The following section describes the components and the setup of the cooling system I developed and used to control the required temperatures for the diffusion chamber and on the ice growth surface.

The cooling system consists of a Peltier effect based cryo-SEM sample holder (Ultra Coolstage, Deben, UK) supplemented with an additional Joule-Thomson based circulation bath refrigerator (RP890, Lauda, DE). Both systems have their own closed loop temperature regulation and work independently.

The coolstage removes excess heat from the Peltier element's hot side inside the vacuum chamber using a circulating water cooling circuit. To increase the accessible temperature range, this coolant circuit is pre-cooled using the circulation bath. The coolant used in the circulation bath is a silicone oil (Kryo 85, Lauda, DE), which avoids safety problems associated with the use of ethanol and can be operated to temperatures as low as -89 °C.

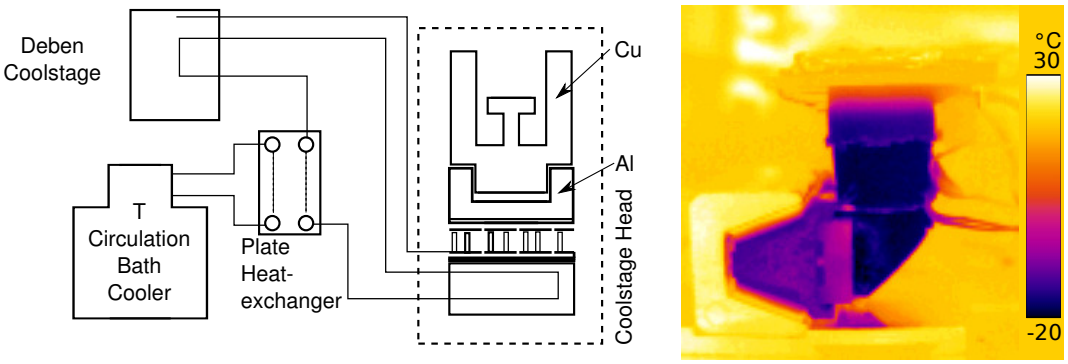

Figure 2.11 – Schematic of the cooling system components, left, and an infra-red thermal image (compare image b, figure 2.8) of the mounted small diffusion chamber (right). A circulation bath is coupled with the SEM cryostage cooling circuit using a plate heat exchanger to separate the circuits. The coolstage is set to -15 °C for the thermal image, which is taken against the room background (≈27 °C).

The two cooling circuits are separated using a standard 7 kW gas boiler plate heat exchanger. The coolstage circuit is pre-cooled using a set temperature of 1°C (see figure 2.11). This improves performance of the coolstage and also permits to rapidly reduce the temperature down to -49 °C, which due to the heat load of the chamber is otherwise not possible. The coolstage is connected using its RS-232 interface to the control PC, for measuring and setting the temperature of the source ice (T_{ice}) in 1 °C steps. The readout has a precision of ± 0.2 °C and is summarized in table 2.2.

From the thermal image in figure 2.11, it can be seen that the detector is more or less at ambient temperature and there is a temperature gradient in the closing lid. The picture was taken at ambient pressure at room temperature. When measuring the detector temperature inside the SEM specimen chamber and under different vacuum conditions, I found that for a diffusion chamber temperature of -45 °C the upper side of the detector is at ≈20 °C at high vacuum, and slightly lower at higher pressure (≈15 °C). An improvement, implemented towards the end of this project, is to link the detector's copper shield (intended for electron and noise shielding) with the diffusion chamber by connecting the copper lead thermally. The detector temperature then can be brought down to 6 °C. This is still high and might lead to radiative effects on particles residing on the growth surface.

The small Peltier element is driven via the micro controller interface; the driver circuit is described in section 2.10.

Device	Temperature accuracy (°C)	Step size (°C)
Deben Ultra Coolstage (-45 – 0 °C)	+0.2, -0.6[a]	1
Lauda Proline RP 890	±0.02	0.01
I²C-Thmod interface	0.1 °C	0.05 °C
Total		

[a]calibrated; specification: ±1.5 °C

[b]tolerance class one

Table 2.2 – Vendor specified temperature accuracies and resolutions.

2.8 Experiment Control

This section describes the electronic and hardware parts I engineered to control the diffusion chamber experiment. This includes the control and automatization of the scanning electron microscope, reading environmental parameters such as temperatures and pressures as well as the infrasturcture for conducting unsupervised experimental runs.

The set-up is mainly based on a micro controller platform which receives commands and can output data via a universal serial bus (USB) to an experiment control computer and a second part that communicates with the SEM control software via Ethernet network. The control computer runs the software that stores data and manages the experimental runs.

2.9 Controller

The sensor readout and Peltier control is built upon an 8-bit micro controller (328p, Atmel, US). This is an 8-bit RISC architecture, 32 KB EEPROM, 2 KB SRAM microcontroller with 20 million instructions per second (MPIS) when running at 20 MHz clock frequency.

I developed a message based scheme that serves as a simple operating system (OS), written mostly in C, and consists of three core parts: a regular timer overflow interrupt every 200 µs, a message stack and a main processing loop which processes the messages in the stack. This scheme enables non-blocking execution of code segments, such as requesting a sensor reading or responding

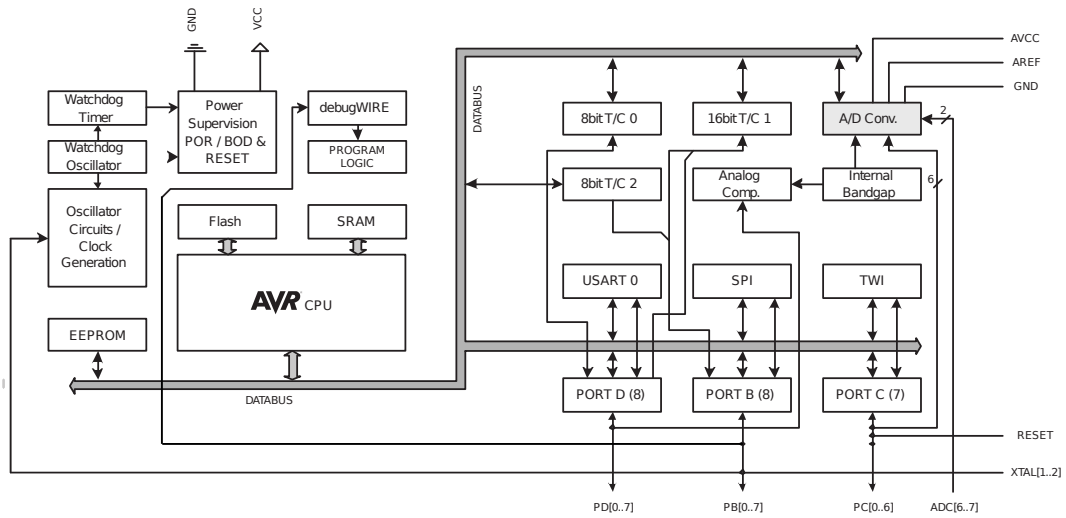

Figure 2.12 – Left: Functional blocks of the Atmel 328p 8-bit microcontroller (reproduced with permission from Atmel corporation, US). The main central processing unit (CPU) is complemented by two 8 bit and one 16 bit timer/counter (T/C), a 6 channel 10 bit analogue to digital converter (A/D) with internal semiconductor bandgap voltage reference (Bandgap), a programmable serial universal asynchronous receiver/-transmitter (USART), a dedicated serial peripheral interface bus (SPI) and a 2-wire interface (TWI) which can be used to connect to I^2C peripherals. Several digital 8 bit wide ports are also available.

to external commands. This message based approach has proven to be very flexible when introducing new features or changes, can be very easily ported to a different hardware platform and works very reliably in operation.

I complemented this OS with an implementation of a simple communication protocol, for which I chose a subset of the Standard Commands for Programmable Instruments (SCPI) protocol[9] (SCPI (1999)) defined in the IEEE 488.2 specification. It is an American Standard Code for Information Interchange (ASCII) character based protocol and widely used in laboratory automatization devices and software. The physical link layer is not defined in the specification and the implementation here uses a serial communication over a USB link.

A typical set of commands sent over a virtual serial connection from a host computer to the controller looks like:

```
*RST
*IDN?
MEASure:VOLTage0?
```

[9] www.scpiconsortium.org

```
SET:PID ON
WAVeform:STATUSus?
```

The controller responds with an identification string to the `*IDN?` command, resets all internal states to a default on `*RST`, returns a one off voltage reading of channel 0 for `MEAS:VOLT0?`, changes the internal mode for the PID controller to on for `SET:PID ON` and more similarly.

In my implementation, the individual characters are received by the controller USART and an interrupt routine adds them to a small input ring-buffer. If a complete command (e.g. `MEAS:VOLT0?, '\n'` terminated) is received, an internal system message indicating the reception of the command is generated and put onto the main message stack. The message triggers the further processing of the command such as invoking the code to obtain a voltage reading from an analogue input pin and sending a response.

At any time, and in nearly any part of the code, messages can be generated, which makes this approach very versatile. A good example is the non-blocking behaviour when requesting a sensor reading for which the sensor needs some time to deliver the response (e.g. 100 ms) after the request is made: instead of waiting and polling the sensor for completion of the request, one simply re-issues the read-sensor-value message. Meanwhile the system can continue processing other messages. On successful completion of the read-sensor-value command a different new message is emitted which triggers output of the controller response via its serial communication line.

The functionality I implemented using the controller includes:

- Thermo electric driver circuit for the ice growth surface Peltier element,
- digital PID closed loop control for the temperature difference between source ice and ice growth surface,
- sampling of the capacitance manometer pressure output,
- two potential free switching contacts (reed relays),
- two temperature readings,
- one additional general purpose 0-10 V analogue input.

These are described in more detail in the following sections.

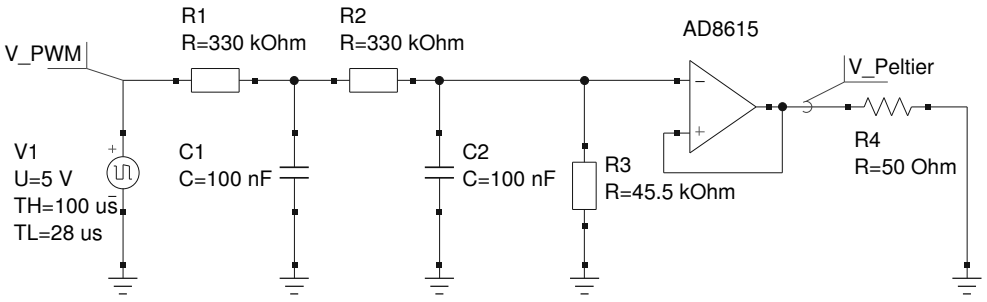

Figure 2.13 – The schematic of the output stage of the Peltier driver. To implement a simple 10 bit precision digital to analogue converter, a digitally generated pulse signal is filtered with a two pole low pass RC-filter. A high output current operational amplifier is used to buffer the signal and provide the drive current for the thermoelectric element. R3 forms a voltage divider which scales the maximum voltage .

2.10 The Peltier Driver

The Peltier element used to control the temperature of the ice growth surface is a 4 W, 4x4 mm module[10] with 14 junctions and a ceramic surface.

To control the temperature of the surface, the voltage across the junctions is controlled using a voltage source. Because the power consumption of the element is small, for simplicity of the circuit I used a unity gain stable, high output current, rail-to-rail operational amplifier (op-amp) (AD8615, Analog Devices, US) to directly drive the Peltier element as shown in figure 2.13. This avoids the electrical noise associated with transients when driving the Peltier element with a pulse width modulated (PWM) signal directly, which is the conventional approach to a Peltier driver circuit design.

Instead, I implemented a PWM digital to analogue converter (DAC) scheme, in whichthe drive voltage and consequently the temperature is selected with a software command (`SET:AOUT nnnn`, $0 \leq nnnn \leq 1024, n \epsilon \mathbb{N}$).

In this PWM technique a pulse train with a fixed frequency (f=7.8 kHz) is generated by the microcontroller. The width of the signal high time is proportional to a timer counter variable (a register) inside the microcontroller. Similar to a lab timer, the value of this register is decreased in constant time steps and a change of state is initiated — the output pin is switched to low, when the value reaches zero — the timer expires. The timer register is then reloaded

[10] RS order no: 693-5132, Farnell: 105-940

with a new value and the process restarts. The resolution of the timer counter used is 10 bit, so 1024 (=2^{10}) different values for the duty cycle (the time the signal is high) can be selected. To convert these values into a stable and mostly constant output voltage the signal is filtered using a two pole RC low pass filter to remove the high frequency components of the pulse signal. The smooth output voltage is then proportional to the chosen timer register value.

The base frequency of the pulse train needs to be chosen such that the low pass filter removes enough of these frequency components of the signal.

The design process for the second order filter is outlined below. Starting with a general voltage divider:

$$V_{out} = \frac{Z_1}{Z_1 + Z_2} V_{in} \tag{2.34}$$

$Z_1 = R$ and $Z_2 = \frac{1}{j\omega C}$ being the impedances of the resistor and capacitor respectively, the transfer function is given as the ratio:

$$H_1(j\omega) = \frac{V_{out}}{V_{in}} = \frac{\frac{1}{j\omega C}}{R + \frac{1}{j\omega C}} = \frac{1}{1 + j\omega RC} \tag{2.35}$$

R (Ohm) resistance, C (F) capacitance, ω (rad^{-1}) the angular frequency of a sinusoidal input voltage and $j^2 \coloneqq -1$. Rewriting this in terms of the complex Laplace transform variable $s = j\omega + \sigma$ (we ignore phase shift as it is irrelevant for this application) and using a filter time constant $\tau \coloneqq RC$ and $k = 1$ (for a passive circuit) the single pole transfer function is

$$H_1(s) = k\frac{1}{1 + s\tau} \tag{2.36}$$

The 2nd order filter transfer function is obtained by successive application of the single order filter transfer functions:

$$H_2(s) = H_1(s) \cdot H_1(s) = \frac{1}{(1 + s\tau)^2} \tag{2.37}$$

To find the amplitude behaviour, while ignoring phase shift

$$|H_2(j\omega)| = \frac{1}{\sqrt{1 + (\omega\tau)^2}} \tag{2.38}$$

The cut-off frequency ω_c, defined as the frequency where the signal power delivered is reduced to $\frac{1}{2}$, or by 3 dB, we solve for ω_c and a gain g of -3 dB

$$g = 20\, log_{10}(|H_2(j\omega)|) \tag{2.39}$$

$$|H_2(j\omega_c)| = 10^{-\frac{3}{20}} \tag{2.40}$$

which results in a cut-off frequency of $f_c \approx 3$ Hz, for the chosen values of R=330 kΩ and C=100 nF. This is sufficient to suppress the base frequency components of the PWM input train.

2.11 Temperature Measurements

Several temperatures in the experiment require measuring and recording in the setup. Some are readily available in a digital format, such as the source ice temperature (T_{ice}), which can be read from the coolstage via a serial data link, and the pre-cooling circuit temperature accessible through a serial interface from the circulation bath refrigerator. The temperature difference (ΔT) of the ice growth surface (T_{surf}) to the temperature of the source ice (T_{ice}) is the most challenging one to measure.

When choosing a measurement technique several factors need to be considered: small heat load on the growth surface, fast response time and an easy wiring scheme, as signal lines need to be passed to the outside of the vacuum through an electrical feed-through.

From a physics perspective, there are two main possibilities (radiative or density based methods are ruled out): using a thermocouple junction or using a resistive element, both well established techniques in temperature metrology.

For the temperature ranges of interest (broadly $-100 < T < 50$ °C) the most accurate and precise option is a platinum resistive (PTR) element such as a Pt100[11] element. Problems with this choice for very small probes are: self-heating of the platinum element during the measurement, and that for recording a temperature difference one needs two measurements. To guarantee a robust electrical readout the connection would need to be a 4-wire interface,

[11] 100 Ohm at 0 °C

which by design cancels measurement errors from the wire's (non constant) resistances. This results in 8 wires for two measurement points. In addition, although there are some small elements available (SMD 0805 package, $1.9 \times 1.2 \times 0.5$ mm) they still are difficult to incorporate into the growth surface.

The second option is using a thermocouple junction for measurements. Thermocouples are appreciated for their ease of use and robustness and are the main sensor for industrial and process temperature measurements. Thermocouples are standardized and are classified into groups according to the metal junctions they consist of, and into accuracy tolerance classes 1, 2 and 3.

The document containing the relevant specifications is the British Standard (BS) EN 60584-1:2013, which is partly based on the National Institute of Standards and Technology of the USA (NIST) Monograph 175 (Croarkin et al. (1993)), which itself is based on the definition of the temperature scale as set out in the International Temperature Scale 90 , ITS-90, (Preston-Thomas (1990)). It also contains the polynomial coefficients needed to relate a thermocouple junction voltages to temperatures (table 2.3, computer readable version in footnote[12]).

The most common general purpose thermocouple with a sensitivity of ≈ 41 µV °C^{-1} is the K-type, which is a chromel-alumel junction (alloy with 90-10%, Ni-Cr and 95-2-2-1%, Ni-Mn-Al-Si respectively). The type T thermocouples are Cu-constantan (55-45%, Cu-Ni), the most accurate type, with a sensitivity of ≈43 µV °C^{-1}. They can also conveniently be used in a differential configuration (see figure 2.14, left) where the two copper sides connect to the voltage measurement instrument. The high thermal conductivity of copper and the resulting heat outflux needs to be considered.

In the standard measurement set-up of one thermocouple junction, the two connections of the thermocouple to the voltage measurement circuit will add two different new metal-Cu junctions (figure 2.14, right). The classic arrangement is to use a differential setup with two junctions and maintain one junction at a precisely known temperature, 0 °C using an ice bath for example (figure 2.14, middle). Modern circuits replace the ice bath, by compensating it numerically and measuring the temperature of the connector block with a PTR element.

The junction voltages for different thermocouple types are then computed and

[12] http://srdata.nist.gov/its90/download/type_k.tab

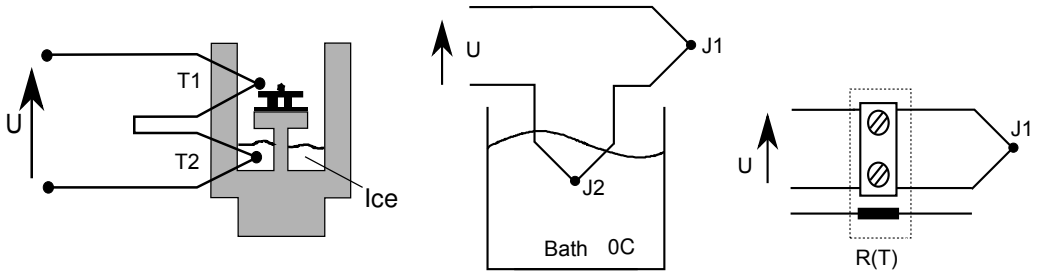

Figure 2.14 – Thermocouple setup variants used to measure the temperature (T_1) of the free (J1) metal-metal junction. Left: Differential configuration to measure the temperature difference of the ice growth surface (T_{surf}) and the source ice (T_{ice}) inside the small diffusion chamber. Middle: first principle cold junction reference and, right, a configuration used to simulate cold junction (right) as it is used in many hand-held devices. In the first case the measurement is related to a water ice bath to give a 0 ºC reference. In the second case a resistive element (Pt-100, typically) is used to measure the temperature of the connection block and the voltages that would be introduced by a junction at 0 ºC using the inverse ITS-90 polynomials derived and added to the loop voltage.

subtracted. The accuracy of the values critically depends on the correctness of this temperature reading.

Previously, junctions from wires with a diameter as small as 25 µm and 13 µm have been successfully used (Hall (1990), Wildmann et al. (2013)) for temperature measurements. Fish et al. (1995) even describe how to manufacture sub-micron sized Au-Pt junction thermocouples using a glass micropipette pulling technique.

In my exploratory experiments with a very thin thermocouple (ø=25 µm, Labfacility, UK[13]) junction, though, I found that from the instruments or interfaces that were available in our lab (e.g. U2351, Agilent, US) none of them would read any junction voltage. The current the small junction can generate is too small.

Interestingly, I could not find any data or literature on the current a metal-metal junction can provide for a thermocouple junction.

Later, I could demonstrate a functional frontend using two ultra low input current (typ. 2 fA) operational amplifiers in instrumentation amplifier configuration (LMC6042, Texas Instruments, US). When developing this circuit I found that even leakage currents of a small capacitor would 'short' out the

[13]RS order no 397-1573

junction's potential difference when placed across the thermocouple contacts as part of a low-pass filter. This demonstrates that only an extremely careful design, layout and choice of the components in the section in front of the first amplifier stage results in a functional circuit.

At the time, and also because the 25 µm wires are difficult to manipulate I used a larger diameter type K thermocouple, configured as two differential junctions (figure 2.14). Because of their larger diameter, the junction contact area is larger and the amount of charge separated there can easily drive a standard frontend. The frontend[14] I chose (Thmod-I^{2}C-300, Conrad, UK), offers a I^{2}C digital interface for reading out the measurements, which makes passing the signals through the vacuum feed-through simple. It has 15 bit ($2^{15} = 32768$) resolution, which results in a 2 µV (≈ 0.05 °C, theoretical) resolution for the measurement range of -12.5 mV to 20.268 mV. The circuit element resides inside the vacuum.

One thermocouple junction (T_2) is isolated with a teflon band and directly frozen in to the source ice, the second junction is glued onto a kerb of the ceramic of the Peltier element. A temperature difference between the source ice and the cold surface of the Peltier element results in a voltage difference on the output of the two configured junctions which is collected digitally by the controller (at a rate of 100 ms).

Conversion of the thermocouple voltage to a temperature or its inverse is done using polynomials given in equations 2.41-2.43 using the coefficients for the respective thermocouple type (coefficients for type K are in table 2.3 and 2.4).

$$T(U) = d_0 + \sum_{n=1}^{9} d_n U^n \tag{2.41}$$

$$U(T) = c_0 + \sum_{n=1}^{N} c_n T^n,\ T < 0 \tag{2.42}$$

$$U(T) = c_0 + \sum_{n=1}^{N} c_n T^n\ + a_0\, e^{a_1 (T - a_2)^2},\ T \geq 0 \tag{2.43}$$

T is the junction voltage in °C, U the voltage in mV.

Using these polynomials the ice growth surface temperature (T_{surf}) can be computed from the measurements as follows:

[14] based on a ZMD3105 (ZMD, DE)

	ITS-90 K-Type Thermocouples Temperature to Voltage		
	-270–0 °C, eqn 2.42	0–1372 °C, eqn 2.43	
c_0	0.0	-0.17600413686e-01	
c_1	0.39450128025e-01	0.38921204975e-01	
c_2	0.23622373598e-04	0.18558770032e-04	
c_3	-0.32858906784e-06	-0.99457592874e-07	
c_4	-0.49904828777e-08	0.31840945719e-09	
c_5	-0.67509059173e-10	-0.56072844889e-12	
c_6	-0.57410327428e-12	0.56075059059e-15	
c_7	-0.31088872894e-14	-0.32020720003e-18	Exponential coefficients
c_8	-0.10451609365e-16	0.97151147152e-22	$a_0 = 0.11859760$
c_9	-0.19889266878e-19	-0.12104721275e-25	$a_1 = -0.11834320\ 10^{-3}$
c_{10}	-0.16322697486e-22		$a_2 = 0.12696860\ 10^{3}$

Table 2.3 – The NIST ITS-90 coefficients for type K thermocouple polynomials, given for two sub temperature ranges for conversion of a temperature into the equivalent junction voltage.

	ITS-90 K-Type Thermocouples Voltage to Temperature -200–0 °C, eqn 2.42
d_0	0.0
d_1	2.5173462e+01
d_2	-1.1662878e+00
d_3	-1.0833638e+00
d_4	-8.9773540e-01
d_5	-3.7342377e-01
d_6	-8.6632643e-02
d_7	-1.0450598e-02
d_8	-5.1920577e-04
d_9	0.0
	Error: -0.02 – 0.04 °C

Table 2.4 – The NIST ITS-90 coefficients for type K thermocouple polynomials for conversion of a junction voltage into temperature for T<0 °C.

$$T_{surf} = T(\, U(T_{ice}) + \Delta U \,) \tag{2.44}$$

$$\Delta T \coloneqq T_{ice} - T_{surf} \tag{2.45}$$

2.12 Temperature Feedback Loop

Originally, the growth surface temperature was controlled only by maintaining the voltage across the Peltier junctions, making the assumption that for a given drive voltage the Peltier would maintain a certain temperature difference ΔT. During the course of the experimental runs I established that the temperature difference maintained by the Peltier for a given voltage can decrease with the total time the experiments are conducted. The cause for this is not well understood. One reason could be that ice starts to grow inside the element on the cold side of the junctions' blocks, as these are the coldest points in the chamber. This might subsequently thermally short circuit the hot and cold ceramic surfaces and lead to a loss of efficiency. It seems unlikely that the water vapour can diffuse into the semiconductor material and change its properties — frequently bismuth tellurid (Bi_2Te_3) is used, but the exact material used in the element is unknown. The effect is reversible as the element will recover overnight in the evacuated chamber.

As a remedy I added a proportional-integral-derivative feedback loop (PID) to be able to set the temperature instead of the driving voltage and which at the same time increases the accuracy of the temperature control. A digital PID controller, implemented in software on the microcontroller links the measured thermocouple voltage $\Delta U(t)$ and adjusts the voltage for the growth surface Peltier, driving and maintaining the temperature to the set temperature.

A PID controller changes its output according to internal terms in equation 2.50 depending on the difference, or error, $e(t)$ of the measured current state of the system $U(t)$ and an externally provided set point U_{set}.

$$e(t) \coloneqq U_{set} - U(t) \tag{2.46}$$

$$P(t) \coloneqq k_p e(t) \tag{2.47}$$

$$I(t) \coloneqq k_i \int_0^t e(\tau)\, d\tau \tag{2.48}$$

$$D(t) \coloneqq k_d \frac{d}{dt} e(t) \tag{2.49}$$

$$U_{out}(t) = P(t) + I(t) + D(t) \tag{2.50}$$

with $k_p, k_i, k_d \epsilon \mathbb{R}$ factors for the proportional, integral, and differential terms.

The discreet implementation uses numerical integration and finite differences for the derivatives which are computed inside an update function that is invoked at constant regular time intervals. Additional limitations are:
$0 \leq U_{out}(t) \leq U_{outmax}$ and $0 \leq I(t) \leq U_{outmax}$. This clamps the possible output to the maximum of the digital to analogue converter ($U_{outmax} = 1023$). The same limit is enforced for the integral term to avoid what is referred to as "controller wind up" — the situation when $I(t) \to \infty$.

The implementation schedules a call to the update function every 100 ms from within a timer interrupt. A current reading of $U(t)$ is taken and all values are updated and a new drive voltage $U_{out}(t)$ written to the digital to analogue converter (DAC).

Several algorithms exist to find the parameters $k_p,\ k_i$ and k_d, a process which is referred to as "tuning the controller". Important methods for tuning are presented in Ziegler and Nichols (1942), Cohen and Coon (1953), Rivera et al. (1986).

They all involve means to learn more about the system's transfer function by either looking at the open loop step response, at a response of the system to periodic input changes or a combination thereof.

I used the Ziegler-Nichols method. In this method one needs to find the value of k_p for which the system starts to oscillate. This is done by running a parametric study. Once the critical k_p (=k_{crit}) is found, the oscillation period τ_{osc} is measured.

Using $k_i = k_d = 0$, leaves only the proportional term k_p which is increased in steps and the system's response recorded (see figure 2.15). $k_p = 50$ leads to

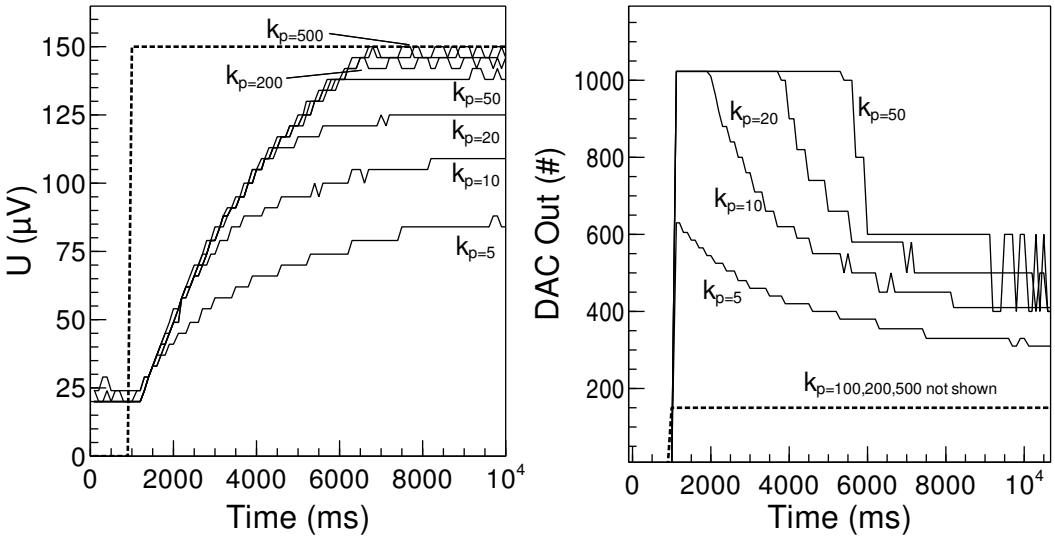

Figure 2.15 – Closed-loop system response to a step command for $k_p = \{5, 10, 20, 50, 100, 200, 500\}$, $k_i = k_d = 0$ (left); 10 bit resolution DAC controller output (right).

oscillation with period $\tau_{osc} \approx 500\,ms$ of the output and therefore marks the critical value $k_c = 50$. k_i and k_d are adjusted using the values in table 2.5.

Figure 2.16 shows the Peltier response to a step change input and demonstrates that the objective of controlling the temperature has been achieved.

	k_p	k_i	k_d
P	$\frac{k_c}{2}$	0	0
PI	$\frac{k_c}{2.2}$	$\frac{1.2}{\tau_{osc}}$	0
PID	$\frac{k_c}{1.7}$	$\frac{2}{\tau_{osc}}$	$\frac{\tau_{osc}}{8}$

Table 2.5 – Ziegler-Nichols method parameters for the respective controllers; values for the 'closed loop' tuning method (Ziegler and Nichols (1942)).

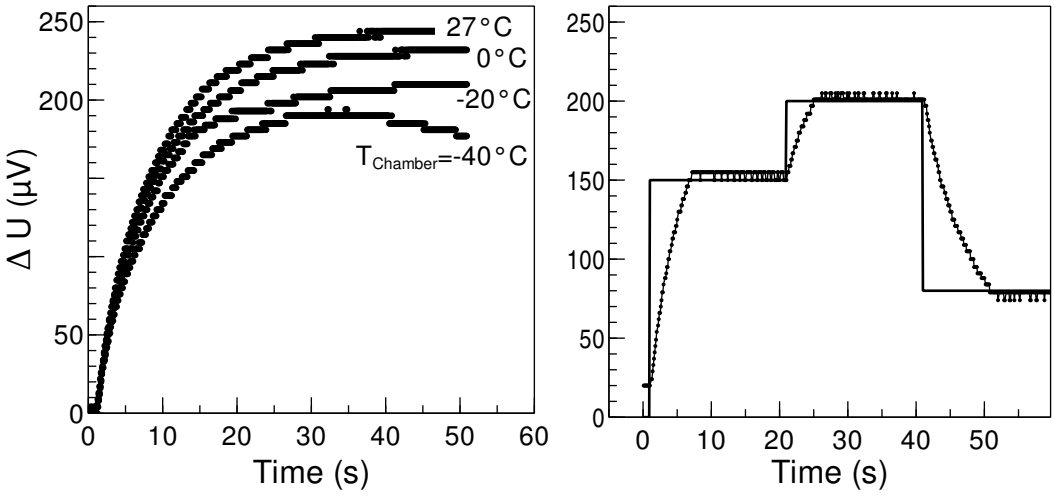

Figure 2.16 – Step response open loop for different chamber temperatures (left): note that the same voltage applied does lead to different ΔT for different diffusion chamber temperatures. A closed loop (PID controlled) response example for the system at room temperature (27 °C) (right) .

2.13 Control Computer

The control computer, a standard desktop PC running windows, runs the central data acquisition and sets the experimental parameters and triggers imaging. My experiment software is written in C++ and uses the Qt library[15], an open source cross platform application framework, for its graphical user interface.

Hardware communications channels (USB, virtual serial via USB, and a RS232) to instruments are accessed through an installation of the virtual instrument systems architecture (VISA), a library jointly developed by HP/Agilent and National Instruments (NI). This has evolved into an industry standard and is now maintained by the IVI foundation[16]. This library allows the application to access connected instruments regardless of their physical bus requirements. A C application interface (API) (Agilent Technologies (2001)) to send commands and receive responses to virtual instruments is provided. Every installed instrument and available communication bus is uniquely enumerated and can be accessed by an identifier, such as `USB0::0x0957::0x1318::TW49462520::0::INSTR`, which represents the identifier of a USB connected DAQ device. In a networked

[15] `www.qt-project.org`
[16] `www.ivifoundation.org`

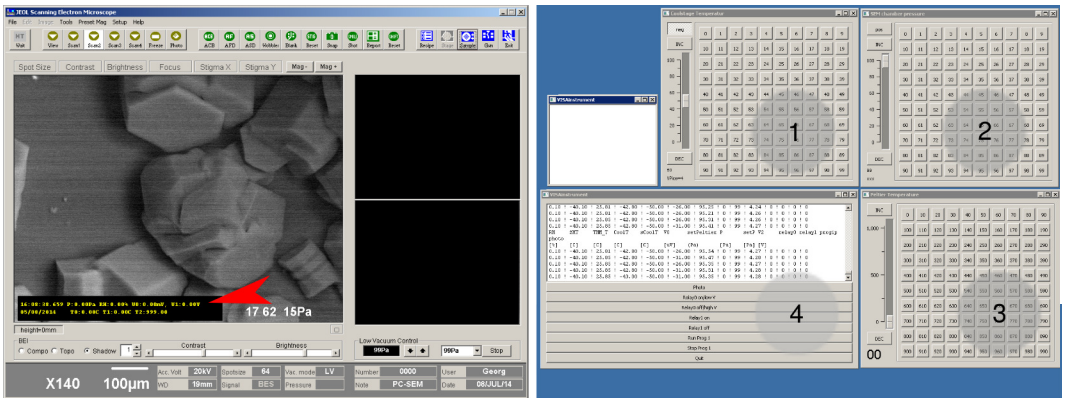

Figure 2.17 – SEM client user interface with the overlay (red arrow) to present a time-code and parameters (left). The experiment software interface (right): source ice temperature control (1), SEM chamber pressure control (2), ice growth surface temperature control (3) and the main window with buttons to trigger imaging, start/stop experimental programme runs and logging output of all system values (4).

installation transparent access to instruments connected to different computers is provided. Device identifiers can be found in the connection manager application which is part of every VISA installation or frequently in the front panel setup menus of the instruments. For communicating with an instrument from within a software application one obtains a handle to the instrument using this identifier, opens the connection, and then reads and writes to it using the functions from the VISA API.

The experiment software is central to executing experiments: it records all measurements with a time resolution of 500 ms to file and can play back experimental programme schemes. It controls the ice growth surface temperature (T_{surf}) by communicating temperature settings to the controller. It reads and sets the source ice temperature (T_{ice}) via a serial RS-232 (using a USB to RS232 adapter) interface with the coolstage. It further communicates over Ethernet with the SEM control PC and the network interface extension I wrote for the SEM client software to set chamber pressure and trigger image taking as sketched in figure 2.4. In addition, a central timebase is distributed and can be displayed with a small client window and superimposed onto live images on the SEM control software. This adds a time base and realtime parameters to a screen capture video.

The software is able to play back programmes. In this way several experimental runs can be conducted automatically. A programme can, for example, go

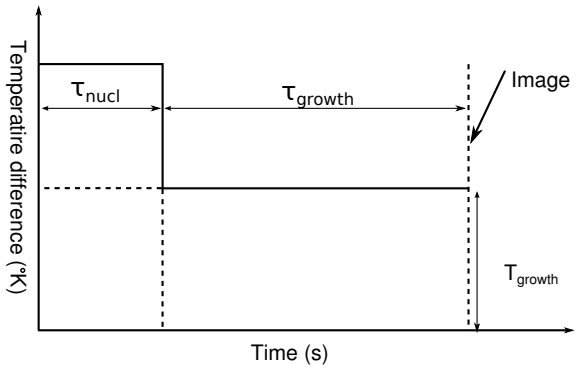

Figure 2.18 – Example of a temperature profile for one experimental run. In an initial nucleation phase lasting for τ_{nucl} seconds a higher temperature difference of T_{nucl} is maintained, then a τ_{growth} seconds crystal growth phase follows with a temperature of T_{growth}. Then the electron beam is activated and imaging is triggered. A program can repeat such a profile and also map one or several parameters by changing the value between different runs.

through a temperature profile (figure 2.18) and automatically take images of the resulting crystals. Parameters can be changed between runs. For example the length of the growth phase (τ_{growth}) can be increased in every run resulting in a time series study, where images are taken at different, increasing, times in the growth phase. Mapping the influence of other parameters, such as pressure changes is equally possible. Every parameter that is controlled by the experiment software can be included in the programme which is defined in C++ code and added at compile time.

2.14 Tools for Particle Handling

A variety of tools are useful to pick up, place and otherwise manipulate micron sized particles: small fine tips are useful to manually interact with the particles. They are mounted onto a 3-axis hydraulic micro manipulator (MHW-103, Narishige, JP), for fine movement control of the samples while they are viewed under an inverted optical microscope (CK2, Olympus, UK).

Moving particles along a surface (such as a glass cover slip) is straightforward, picking them up and transferring them is less so: electrostatic and van der Waals forces can bind particles stronger to the surface than to the tips of the tools, and picking them up and subsequently transferring them to a different target becomes difficult. Three techniques can be used to aid particle release from the

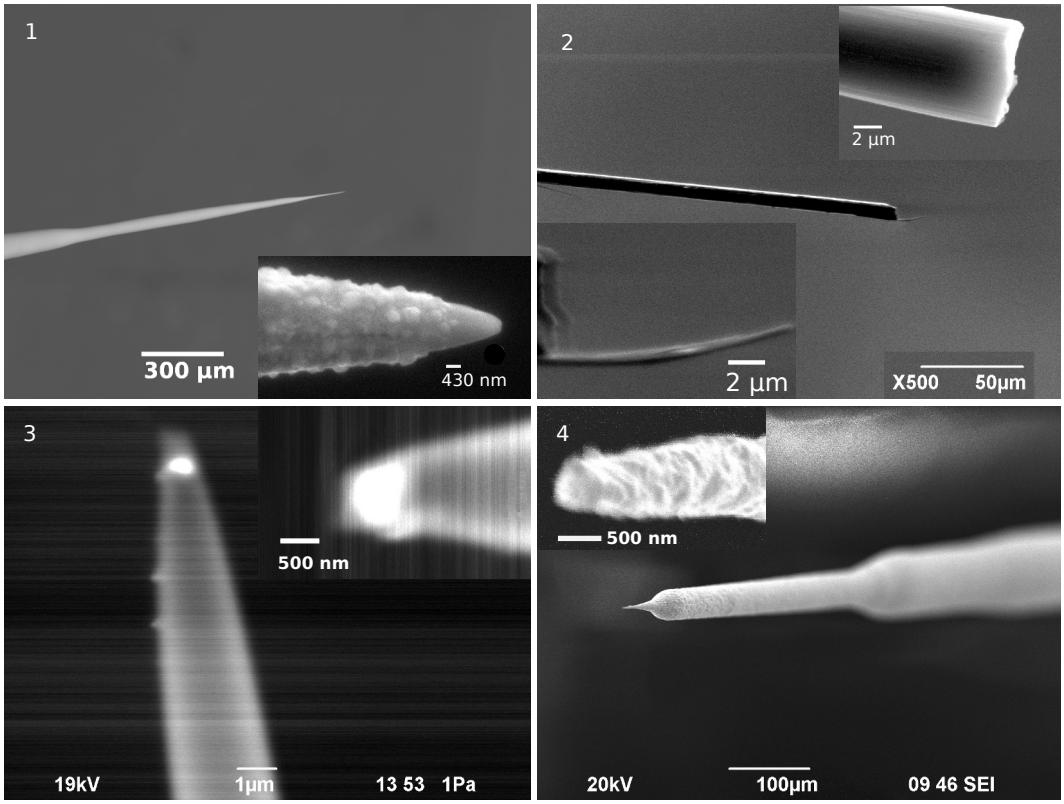

Figure 2.19 – Different manufactured micro probe tips: 1) tungsten (inset: $r_{tip} = 215\,nm$), 2) composite of a glass mounted onto a carbon , upper inset: end of carbon tip, lower inset: fine glass end of the composite , 3) pulled glass tip, 4) etched copper tip.

surface: one is to use a charge gun (Zerostat 3, Sigma Aldrich, UK), designed to neutralize collected and built up static charges by creating a stream of positively and negatively charged ions in air, which deposit and neutralize existing charge. Alternatively one can use two opposing tools to create a counter force, or a solution of glycerol (3% in IPA[17]) to increase stickiness of the tips. Forcibly ejecting particles from a tip can be achieved using electrical charge pulses, for which a potential difference between the optical table and the tip is applied. I found the ejection trajectories to be unpredictable and particles would either go too far or not move at all. In addition, because of polarisation and charging effects, the particles develop a 'memory' for the charge seen, meaning repeating a pulse with the same settings will not repeatedly result in the same behaviour. Small tips became necessary both to manipulate small particles and to grow ice

[17] isopropyl alcohol

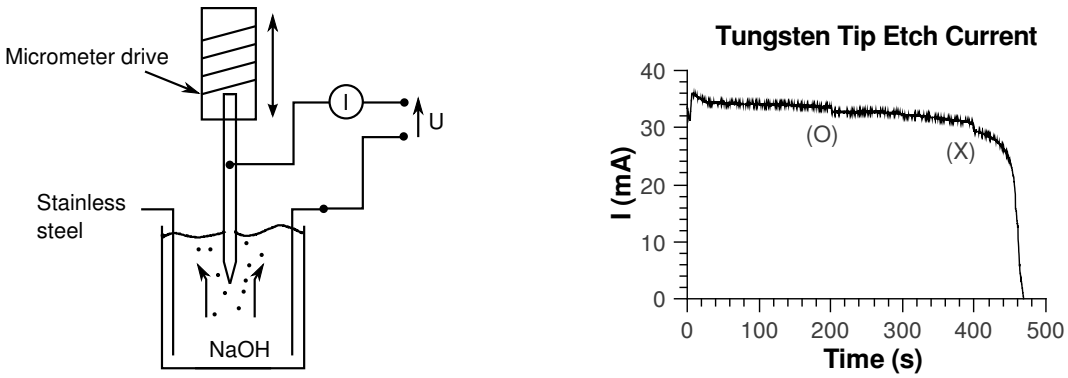

Figure 2.20 – Schematic of the setup used to electro-chemically etch fine metal tips (left). A micrometer drive is used to insert a fine wire into to the caustic etching solution (NaOH, 1 M). An electrical potential U (typically 3.5 V) is applied between a cylindrical stainless steel counter electrode and the tip. The current reduces with decreasing diameter of the wire (right) and a sharp drop indicates the end of the etching process. The wire was lifted a small amount at times (O) and (X), which results in diameter steps seen in figure 2.19 (image 4).

on their micrometre-sized tips.

In the following section, I will describe the procedures used for producing small tungsten, copper, glass and carbon tips (see figure 2.19). The methods I used are electro etching, glass pulling and cutting. These methods were developed in the fields of scanning tunnelling microscopy (STM) and electro physiology where glass micropipettes (openings of <1 µm) are used to investigate electrical potentials of cells firstly developed by Ling and Gerard (1949) for patch clamping application. Further, I developed tips combining materials such a as carbon and fine glass fibres.

I manufactured the tips made of tungsten (W) and copper (Cu) according to ideas and protocols in Vitus et al. (1994), Ibe et al. (1990), Wei-Tse et al. (2012) and glass needles using a micropipette puller, as used for producing micro glass needles. Metal tips can be stored in IPA to limit oxidation.

2.14.1 Tungsten and Copper Tips

The raw material for a tungsten tip is a 0.2 µm wire (Agar Scientific, UK). To produce fine tips, I used the following electro-chemical etching setup: A cylindrical stainless steel mesh counter electrode is placed into a beaker with a

caustic solution (100 ml) of 1 M sodium hydroxide (NaOH)[18], a power supply and an oscilloscope to monitor the etching current.

After applying a potential of ≈3.5 V, the end of the tungsten source wire is inserted about 4 mm into the solution. The etching process starts, gas production at the electrodes creates an upward flow, which aids shaping the meniscus of the electrode Lucier (2001).

To detect the size of the tip the current is monitored (figure: 2.20) and a sudden drop in the current indicates the end of the etching process.

Using the same setup as used for etching tungsten tips, copper needles with a tip radius of <500 nm can be reliably reproduced, using a single thin thread of a flexible copper wire.

It is possible to etch the tip into different size steps (see figure 2.19, picture 4) by lifting the wire out of the solution after different time.

Carbon tips are made out of a woven carbon fibre thread as used for carbon coating samples in preparation for SEM imaging. A support wire with glue is moved to attach to a single carbon fibre and left to cure. The tips are then shortened using a scalpel.

2.14.2 Glass Needles

A standard neurophysiology micropipette puller (720, David Kopf Instruments, USA) was used to pull hollow as well a solid glass tips. The source materials are borosilicate solid rods 1.0 ODx100 L mm, (GR100-10, Harvard Apparatus, UK) and capillary glass tubing 1.5 OD, 0.86 ID, 100L mm (G150F-4, Warner Instruments, USA), as used for the fabrication of patch-clamp pipettes. The settings used are solenoid 5, power 8.5 and the light gate gap (upper end) 22 mm. The tip shape and tapering is excellent, they are long and thin enough and rigidity is very good. They are easy to reproduce and manufacture once the settings for the pulling process are established. Visibility for optical microscopy can be increased by sputter coating (SC7620, Quorum, UK) the needles with gold.

The second method used to manufacture small glass needles was to create a composite of differently sized fibres. Firstly, a support material, such as a carbon is glued to a big wire and shortened. A small amount of epoxy (EpoTek 353ND,

[18] 1M NaOH: (23+16+1)=40 g NaOH in 1 l of H_2O, dissolved in a small amount and then diluted to desired volume.

Intertronics, UK) is picked up and a piece of a micro filter (AP40 010 00, Millipore, US) is taken out of the filter membrane. The carbon with the epoxy is then moved to attach to a fine filter glass and the epoxy cured in place. The tip can then be pulled out and will have a very fine glass end. Although the diameter and the size of this version is small, they are not rigid enough to overcome forces needed for manipulation.

2.15 Heat Shield

The ice growth limiting heat shield consists of a 50 µm copper foil with a 500 µm aperture. It is heated by two 150 Ω ceramic resistors (smd 0805). A supplied voltage of 500 mV results in $P = I^2 R^{-1}$ power (3.3 mW) converted to heat. This configuration successfully limits unwanted ice growth (same figure). This is the best way I found to prevent ice growth on most of the unwanted areas. The downsides are that the aperture affects the electron backscatter path and that the radiative heating is also likely to affect the growth dynamics. The heat shield is software controlled and can be turned off using a software command, for example after a nucleation phase.

2.16 Materials

A variety of materials are needed in the design of the chamber, as well as for the experiments. A main difficulty when choosing materials is their vacuum compatibility, a second factor are the low temperatures if materials are in contact with the small diffusion chamber or the ice growth surface.

Materials used for thermal designs, such as heat conducting silicone pads or pastes to improve heat conductivity in electronic designs, are widely available. But even if their temperature range is suitable, they may not be vacuum compatible. Standard thermally conducting pastes for example have a very high vapour pressure and would outgas, used inside a vacuum, and contaminate the system.

As an adhesive, a vacuum compatible epoxy is used. In the following section I will describe my preparation methods for a vacuum compatible thermal paste,

thermal considerations for a diamond powder loaded epoxy and the procedures I used to prepare a siliconized glass ice growth surface.

2.16.1 Thermal Pastes

As a vacuum compatible paste is not available, I developed a thermally conducting paste based on silver particles. Many commercial pastes are based on zinc oxide, diamond or silver particles, which are mixed into silicone greases but versions with diamond powders (Dow Corning, TC-5026) exist. They are not easily available in small amounts and also do not meet the vapour pressure requirements.

The process to generate a vacuum compatible thermal paste is as follows: particles are extracted from silver paint (G3191, Agar, UK), centrifuged three times for 1 min at 10,000 rpm, washed two times in iso-butyl methylene ketone (R1272, Agar, UK) and then one time in acetone. To form the paste, the silver particles are then mixed into ultra high vacuum grease with a vapour pressure of 9.3×10^{-9} Pa at 20 °C (M Grease, Apiezon, UK). This paste is used to improve the contact between the Peltier element and the ice growth substrate and was found to be working well.

2.16.2 Vacuum Epoxies

Standard epoxies have a low thermal conductivity of < 1 W m^{-1}K^{-1} (Ouellette and Harris (2010)). In a comparison of two epoxies, the authors found that for low temperatures ($-20 < T < -15$ °C) diamond loading did not improve the thermal conductivity. For high temperatures (121 °C) the diamond loading improved thermal conductivity approximately tenfold. Two reasons were given: the low diamond concentration (<10%) and bond thickness. Finally, I used the vacuum specified EpoTek ND353 (Intertronics, UK) without modifications. Hysol 1C (Loctite, UK) is another vacuum compatible epoxy.

2.16.3 Diamond Powders

Small diamonds were extracted from diamond suspensions containing 0.25 µm and 9 µm sized diamonds (MetPrep, UK). 50 ml of the suspension were

centrifuged for 30 min at 3,000 rpm and washed with ultrapure water three times to remove the chemical additives in the suspension liquid. Then the water was left to evaporate in a clean air hood.

2.16.4 Glass Surface Preparation and Cleaning Procedures

Siliconized glass coverslips, 220 µm thick (HR3-215, Hampton Research, US), were cut into 4×4 mm pieces under a water jet using a diamond cutting tool. They were washed and cleaned using ultrapure filtered water (18.2 MΩ cm, Neptune, Purite, UK). The water is filtered again through a cellulose nitrate membrane filter, 0.2 µm pore size (no. 7182 002, Whatman, UK). The slides are then cleaned in an ultrasonic bath (≈40 kHz, Kerry, UK) for 10 min and rinsed again with filtered water.

Remaining debris can be removed with lens cleaning paper (no. 2105 841,105, Whatman, UK). Then the slides are dried on a hot plate at ≈80 ºC for 10 min.

2.17 Imaging

This section describes the backscattered electron detection and amplification circuit I built for the simultaneous multi-channel detection readout. An alternative option for imaging one channel is to connect the custom-made solid-state detector to the microscope input. This has the benefit that, like with the built-in detector, one has access to the full range of image acquisition and processing options offered by the microscope and its software.

In the signal path of the image formation, the first part is the detector element. It converts the impacting backscattered electrons into a signal. If a solid-state element is used this consists of a large area pn-diode junction. Often a variant, a reverse biased p-i-n diode is used (Nikzad et al. (2006)), which includes an additional lightly ('intrinsic') doped layer sandwiched between the p and n layers: this improves response times and quantum efficiency by increasing the interaction volume.

When a diode junction is used for electron detection, the signal is a result of three parts: the incident electron flux, the number of electron-holes generated (average electron-hole generation energy is 3.71 eV in Si) by each incident

electron and the efficiency with which they are detected. The resulting diode current, which is in the order of 10 pA to several nA, can then be amplified.

In general a quantum efficiency of up to 100% can be achieved with solid-state detectors (Funsten et al. (1997)), which indicates that no electron-hole pairs recombine. Off-the-shelf p-i-n diodes (e.g. S3590-08, Hamamatsu, JP) have efficiencies of 85%. An element optimised for electron detection usually has a thinner passivation interface layer than a photodiode designed for photon detection; example include 60 Å, SiO_2 (Funsten et al. (1997)) or a layer of silicon nitride (Si_3N_4) for the custom Centronic element. Funsten et al. (1997) demonstrate, that for electrons with energies above 1.5 keV the influence of the passivation layer on impacting electrons is mainly a loss of beam energy by back scattering. The reduction in sensitivity is therefore proportional to the passivation layer thickness, as electrons undergo several scattering events in this dead layer.

A single channel of the amplifier I built is shown in figure 2.21. The first stage of the circuit is a current-to-voltage converter stage, followed by amplification ($\times$7.5) and a low pass filter ($f_c = 1/2\pi CR$=125 kHz, gain $\times$4.6).

When amplifying signal currents generated by large area photodiodes, problems arise due to their large capacitance, which for the Centronics element is in the $\approx$500 pF. The dark or leakage current is an additional issue if the diode is biased. Additionally, the large capacitance affects the noise behaviour and stability of the feedback loop, which I approached with a trans-impedance amplifier configuration for optimal noise performance. A useful analysis of noise behaviour, and theoretical and practical designs of trans-impedance circuits for photodiodes are discussed in Kim and Koo (2005), Hamstra and Wendland (1972), Hamilton (1991), Brisebois (2006) and the Burr Brown Application Note BOA035.

Figure 2.22, right illustrates how the amplification circuit's four channels are connected to four combined areas of the detector element, and how the signal output is connected to four ADC channels of a USB DAQ instrument (U2335A, Agilent, US).

A C program generates the XY-control waveform for the SEM beam (figure 2.22, left), loads the waveform into the sample buffer (4 MSa) of the DAQ device and plays the pattern back while simultaneously reading the four channels of imaging data. This results in four 2048$\times$2048 pixel intensity fields originating

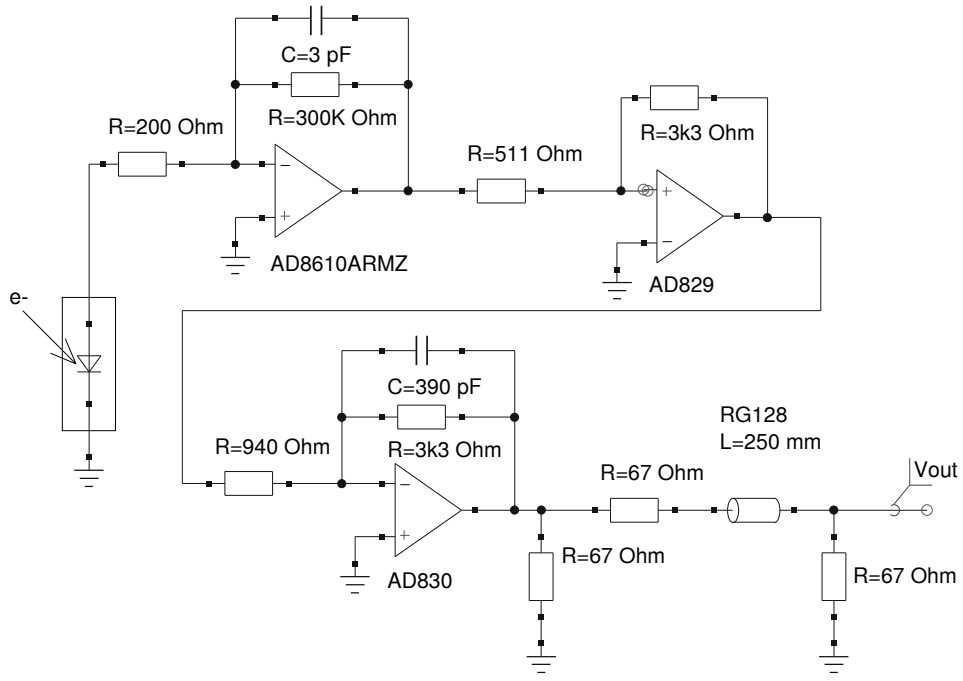

Figure 2.21 – One of four channels of the electron detector amplifier. A current-to-voltage stage followed by an amplification and low pass filter stage. Power supply capacitors, offset correction and feedback compensation are omitted.

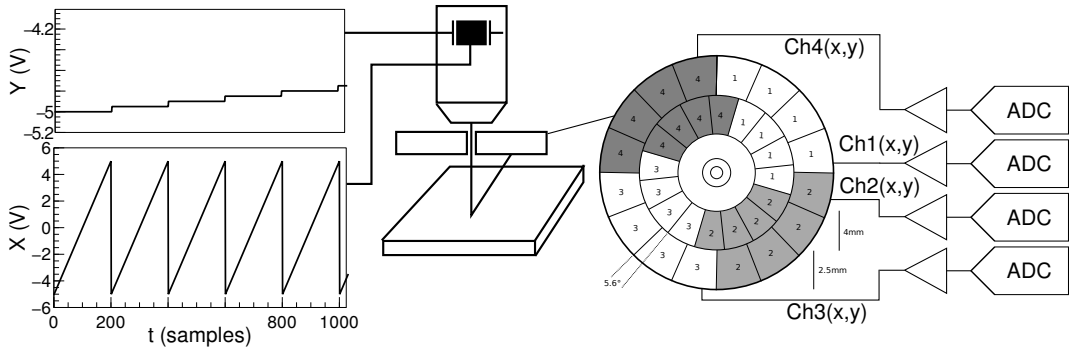

Figure 2.22 – The line scanning signal (X and Y) is produced with a DAQ interface in order to move the electron beam across an area and to read an image with 2048×2048 pixels. While the electron beam is moved across the surface, an ADC records the backscattered electron signals.

from the respective detector areas, stored in an HDF5[19] file. These data can be used to derive information on the normal vectors of the surface at the beam positions.

2.18 Three Dimensional Surface Structure Retrieval

The following section describes the development of a 3D surface structure retrieval system for SEM. I developed two approaches: an intensity based algorithm and a second method based on a photometric stereo algorithm which is used in computer vision and robotics applications. This latter algorithm relies on a simultaneous read out of several imaging signals from different viewpoints. The electronics I developed and the algorithms used are explained in the following section, a preliminary reconstruction result is in figure 2.25.

Firstly, I executed a preliminary test to establish if the method can be used to reproduce surface height (z) using an SEM for imaging: I manually recorded a known target using the rotating stage and the built in detector element. The built in BSE detector has three regions: A, B and C+D as indicated in figure 2.23. The idea is to use the signal of the C detector, as this is at an angle of $\vartheta = 40°$ (for a working distance of 12 mm and distance d =13 mm), and an interchanging light source (detector) and camera (electron beam) to obtain a set of images with virtual light sources from different directions.

[19] www.hdfgroup.org

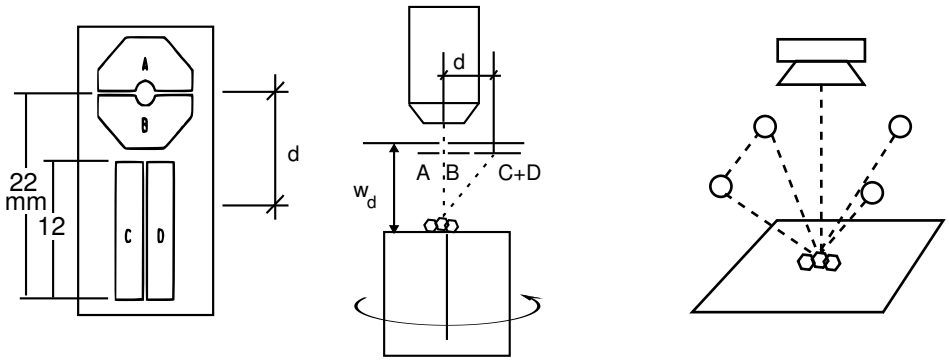

Figure 2.23 – Left: The geometry of the built-in backscattered electron detector element inside the SEM. Elements C, D are used for imaging in topographic modes, (A-C+D, 'shadow' imaging mode). Centre: Setup of the element under the beam column with a working distance w_d to the specimen which can be rotated). Right: The standard setup to take photometric imaging. A camera on top ($\vartheta = 0$) and four light sources. Images are taken by sequential illumination using a single light source and by taking a picture with the camera.

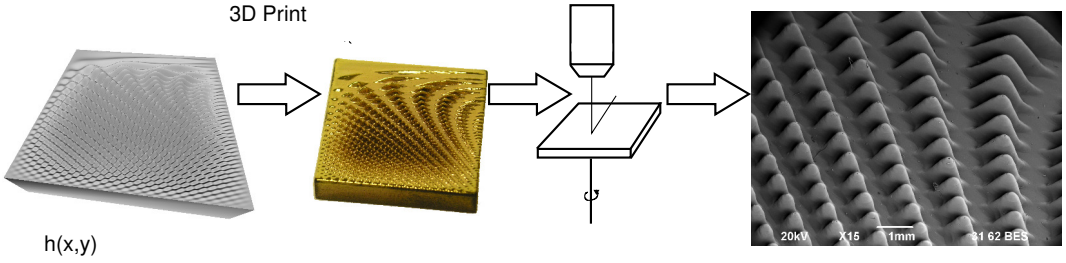

Figure 2.24 – A surface description $h(x, y)$ is generated numerically (left), 3D printed and sputter coated with gold (middle). SEM image of the target surface (right).

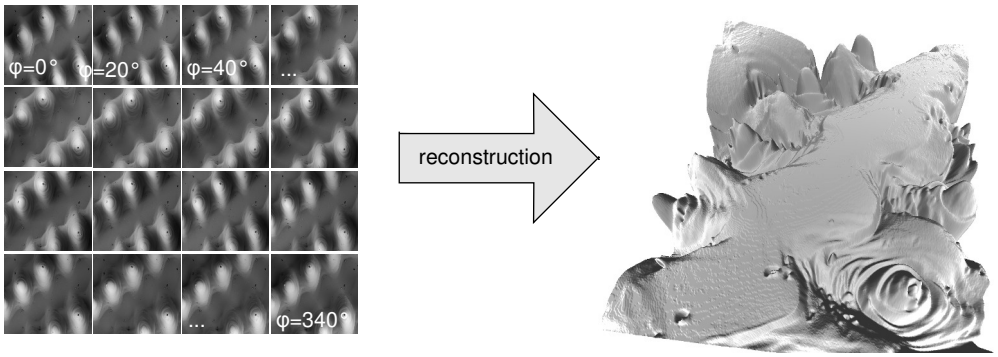

Figure 2.25 – Sequence of images taken of an example target in 'shadow' mode, rotated by $\Delta\varphi = +20°$ and computationally rotated back to simulate the different positions of the light source (left). Preliminary reconstructed surface (right).

I created a 3D target surface ($20 \times 20 \times 4$ mm) with $1/100$ mm grid resolution using the following expression,

$$z(x,y) := \sin\left(\frac{f_{max}}{2\pi}\,\frac{y}{y\,N_y}\,x\right)\cos\left(\frac{f_{max}}{2\pi}\,\frac{y}{y\,N_y}\,y\right) \tag{2.51}$$

The resulting geometry is triangulated and stored using the Stereo Lithography (STL) file format with a script I developed. The surface is then printed in plastic using a 3D printer (Object24, Stratasys, US) and gold coated using a sputter coater, then imaged in the SEM.

When the SEM imaging mode 'Shadow'[20] is selected, the microscope electronics adds signals of all regions ($A + B + C + D$). Taking an image in this mode, and then rotating the target by $\Delta\varphi = +20°$ using the stage, results in the desired image sequence which carries the difference in the (C+D) signal. Images need to be rotated back computationally, so that all images have the same orientation, and only the direction of the virtual 'light source' changes for running them through the reconstruction algorithm.

One practical problem is that the exact rotation centre in the images is not known. I used the following simple search algorithm to find it: first all images are overlayed to find an approximate centre area by inspection. Then, using a window of 50×50 pixels near the approximate centre, I compute the cumulative intensity of the difference between one picture and the next for every pixel in this search window, rotated back for all different 50^2 rotational centre points. The location for which this difference is minimal is chosen as the rotational

[20] Mode 'compo' is (A+B) and 'topo' is (A-B).

Algorithm 2.1 Photometric stereo algorithm (shape from shading, Forsyth and Ponce (2003), Algorithm 5.1, p. 85) to retrieve a height map using images with different illumination directions.

Obtain many images in a fixed view under different illuminants.
Determine the matrix V from source and camera information.
Create arrays for albedo, normal (3 components),
    p (measured value of $\frac{\partial f}{\partial x}$) and
    q (measured value of $\frac{\partial f}{\partial y}$)
For each point in the image array
    Stack image values into a vector i
    Construct the diagonal matrix$I$
    Solve $IVg = Ii$ to obtain g for this point
    Albedo at this point is $|g|$
    Normal at this point is $\frac{g}{|g|}$
    p at this point is $\frac{N_1}{N_3}$
    q at this point is $\frac{N_2}{N_3}$
end
Check: is $\left(\frac{\partial q}{\partial y} - \frac{\partial q}{\partial x}\right)^2$ small everywhere?
Top left corner of height map is zero
For each pixel in the left column of height map
    height value = previous height value + corresponding q value
end
For each row
    For each element of the row except for leftmost
        height value = previous height value + corresponding p value
    end
end

centre and used as origin in all operations.

The images are then run through a reconstruction algorithm, known as "photometric stereo", which I implemented using the Matlab compatible free software package GNU Octave[21]. The algorithm is given in Algorithm 2.1 (Forsyth and Ponce (2003), Algorithm 5.1, p. 85).

Several workers have previously investigated the use of multiple detectors to derive topographic information: Kaczmarek (1998) demonstrates a system to retrieve topographic information using several angled detectors; Spranck et al. (1995) have detailed data on the angular distribution of back scattered electrons; Lindqvist et al. (2011) use stereo photogrammetry from a pair of angled SEM

[21] www.octave.org

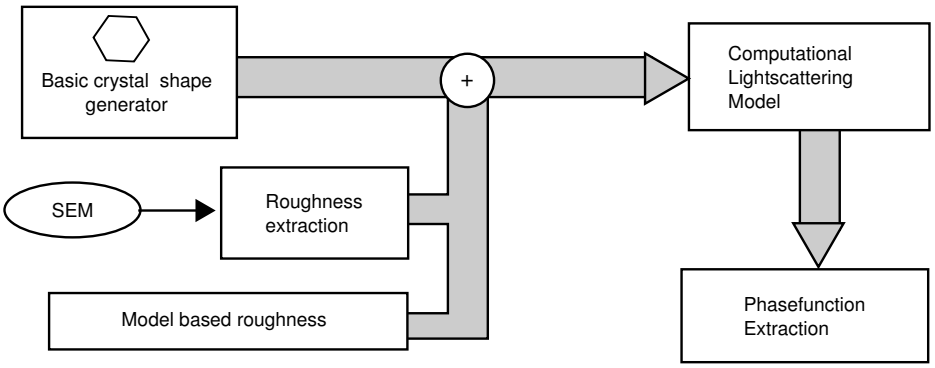

Figure 2.26 – The scheme used to computationally derive light scattering phase functions from crystal models. Virtual crystals are generated using roughness input which is derived from either SEM readings or based on a numerical model. These shapes are processed and then run through a computational light scattering code. As a result phase functions are obtained.

images, Vynnyk et al. (2010) use a two detector version of the photometric algorithm, Paluszynski and Slowko (2009) demonstrate a four detector system with the application to micro roughness measurements and Barsky and Petrou (2003) present an improved 4 source photometric stereo algorithm which separates highlights and shadows from the gradient information. A commercial system, based on a 4 quadrant detector, is available from Zeiss as an option under the name 3D Surface Modelling (3DSM).

2.19 Numerical Crystal Generation

The aim of this section is to outline how light scattering phase functions can be derived from results obtained from experiments on the crystal morphology. I demonstrate here how to numerically generate rough surface crystal models that can be used as input to computational light scattering codes. Consequently, in principle the phase functions and asymmetry parameters can be computed.

The work flow (see figure 2.26) in the modelling algorithm is as follows: In a first step a computer code generates a triangulated mesh of a hexagonal column crystal with optional surface roughness on the facets. The surface roughness can be derived from either experiments, computationally generated using a physical model or derived using a pure mathematical model. In the future it might be

even possible to base the generation on computational models based on a diffusion limited aggregation approach (Witten and M. (1981), Witten and Sander (1983)), or applying mesoscopic approaches such as the model described by Barrett et al. (2012) or the model suggested by Gravner and Griffeath (2009) that replicates most observed snow crystal morphologies, including ridges, sandwich plates and hollow columns.

The resulting crystal geometry model (figure 2.29) is then converted from a triangulated mesh into a uniform Cartesian grid representation with a simple raytracing code that I developed. Every grid point carries a dipole description and a solid body is represented by the different dipole properties on dipoles inside and outside the structure. In this way it is also possible to describe different refractive indices inside the object. This gridded data set can then be used as an input to the Amsterdam discret-dipole approximation (A-DDA) code which numerically solves the electromagnetic scattering field.

Using a triangulated hull, as opposed to using a grid-based approach for generation the crystal geometry models can also be run in the hybrid light scattering code developed in our group (Hesse and Ulanowski (2003)) as this code takes a polygonal description as an input. Also, the conversion of a triangulated mesh to a volumetric grid is easier than the other way round, as the grid representation can be found by simply raytracing through the mesh and placing points when the ray is inside.Finding a triangulated convex hull of a set of points is more difficult.

Because this approach relies on solving a crystal geometry using a dipole approximation code, the size limit for the biggest crystals is dictated by the computational resources available to solve the light scattering for a given geometry. It is in the order of magnitude of 512^2 grid points, which limits the particles size to only small ones as ADDA requires a grid resolution of 10 to 15 dipoles per wavelength λ (incoming).

As soon as enough data or a verified model for the dynamic behaviour of the surface roughness is available, using this work flow the link between the input variables of the roughness models, such as temperature and pressure and the phase functions and asymmetry parameters can be established.

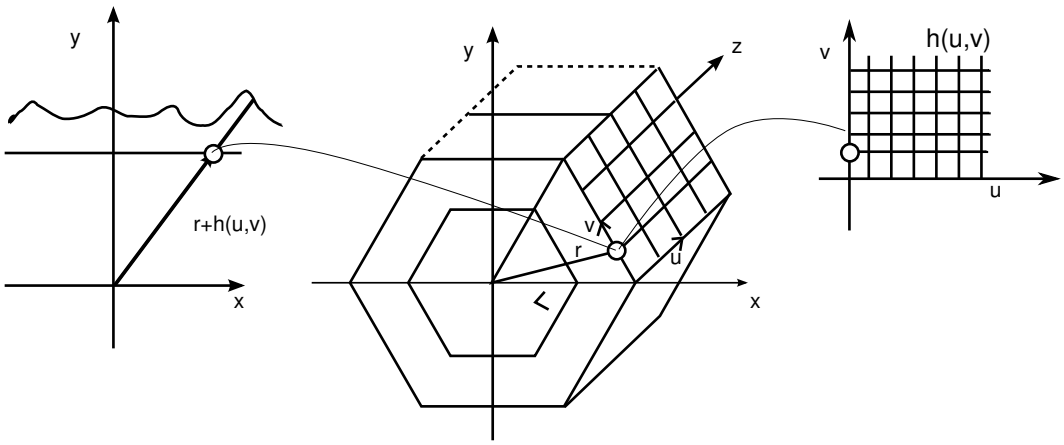

Figure 2.27 – Generation scheme of numerical representation of a hexagonal column with a surface roughness field $h(u, v)$ on the facets.

2.19.1 Crystal Generation

The numerical representation is obtained in form of a triangulated convex hull of a hexagonal column. Surface roughness can be added by supplying a 2D scalar field containing the roughness information (figure 2.27).

Assuming that the roughness is small compared to the diameter of the crystal geometry (length l and face side length a), roughness is added to one facet by displacing the according vertex along the radial r direction by taking values from a 2D scalar field $h(i, j)$ containing the roughness:

$$j, i = 1, 2, 3, ... \quad N_u, N_v \epsilon \mathbb{N}$$

$$1 \leq j \leq N_u, \quad 1 \leq i \leq N_v$$

$$\Delta u = \frac{a}{N_v}, \quad \triangle z = \frac{h}{N_u}$$

For the j^{th} point on one facet slice (fixed z)

$$h_j = ((j-1)\,\Delta u)\, cos\left(\frac{\pi}{6}\right), \quad d_j = ((j-1)\,\triangle u)\, sin\left(\frac{\pi}{6}\right)$$

$$r_j = \sqrt{h_j^2 + d_j^2}$$

$$\varphi_j = \begin{cases} j = 1, & 0 \\ j > 1, & \Phi_f + atan\left(\frac{h}{d}\right) \end{cases}$$

with $\Phi_f = f_n \frac{2\pi}{6}$ for selecting the facet number f_n. Adding the displacement field with a scale factor α,

$$r_{i,j} = r_j + \alpha\, h(i,j), \quad \alpha \epsilon \mathbb{R}$$

and finding the z coordinate for the slice,

$$z_i = i \triangle z$$

the Cartesian position of the vertex is obtained:

$$P_{i,j} = \begin{pmatrix} r_{i,j}\, cos\left(\varphi_f\right) \\ r_{i,j}\, sin\left(\varphi_f\right) \\ z_i \end{pmatrix}$$

This is repeated for all six facets. To avoid discontinuities on the facet boundaries the roughness field $h(i,j)$ is constructed by appending its mirrored self, or by using trapezoidal windowing functions and adding windowed fields together with an overlap, thereby creating a 'mix' at the facet boundaries (figure 2.28).

Deriving surface roughness from an ice crystal in a simple way is achieved by taking an SEM reading from a horizontal facet. The image intensity is used as the height field after some processing (noise filtering and level correction) and applied with a scaling factor to the crystal facet. An example of a crystal model that readily can be used as an input to the light scattering codes is given in figure 2.29.

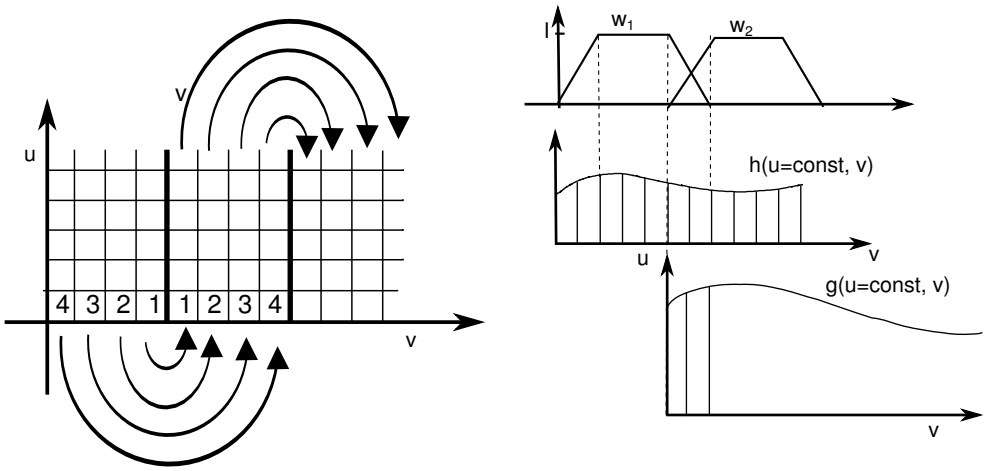

Figure 2.28 – To avoid discontinuities on the facet boundaries, a crystal roughness field h is generated by appending the field for one facet and its mirrored self for the next facet (left). If different fields are used, a trapezoidal windowing function ($w \leq 1$) is used for an overlapping region and the fields h and g which are mixed by adding them weighted with the windowing function (right).

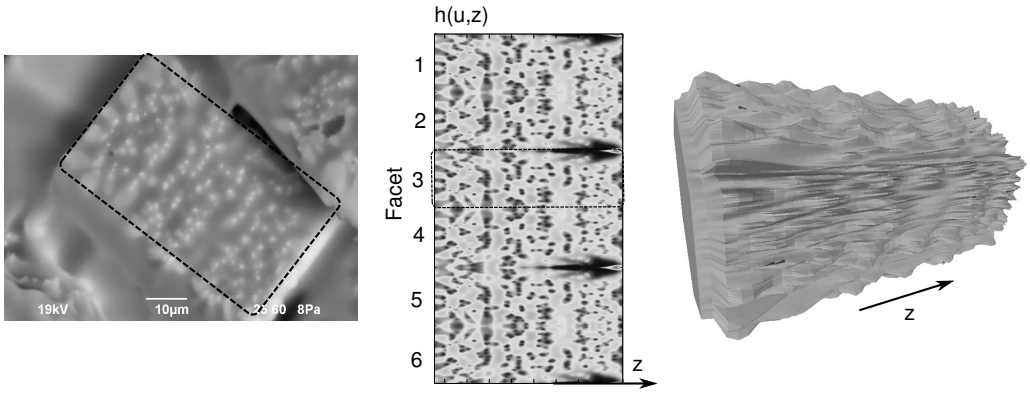

Figure 2.29 – SEM image of roughness developed after sublimation and part regrowth (left). Reconstructed height field, using the roughness indicated by the borders and mirrored for all six facets (middle). Generated crystal mesh with applied roughness from measurement with a lower resolution in z direction and a trapezoidal window applied along the z direction to bring vertex positions to 0 (right).

Chapter 3

Results

The initial experiments I will discuss in this chapter were aimed at exploring whether it was possible to confine ice growth to a small localized region. Materials investigated to limit ice growth are presented and effects related to the technique of SEM imaging discussed. I will present my findings on nucleation targets, such as geometrically patterned surfaces, small needles and mineral dust grains. Further experiments were aimed at studying the relationship of growth rate and the formation of roughness or complex crystals. Finally, I will discuss the effect of sublimation and repeated growth and sublimation cycles.

3.1 Electron Beam Damage

Exposure of the ice surface to the scanning beam causes damage to the crystal surface due to the deposited energy. Because the thermal conductivity of ice is small with 2.4 $Wm^{-1}K^{-1}$ (near -20 °C), the energy is not conducted away from the surface easily, which causes a localized increase in the temperature and sublimation. The patterns of damage are mainly a representation of the line scanning patterns of the beam.

In cases where there are other crystals near the exposed area, the freed excess water vapour is taken up in the surroundings and deposited onto the crystals. Examples of a typical rectangular damage to an ice film is given in figure 3.1. The energy of the beam can also be used to selectively manipulate crystals, which works especially well on very low thermal conductivity surfaces such as acrylic polymer or glass (figure 3.1).

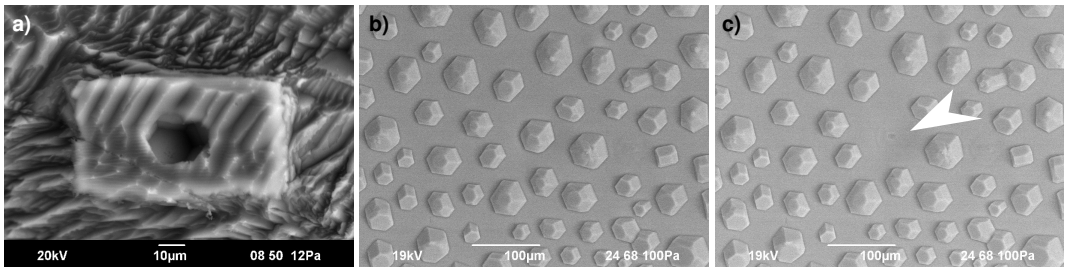

Figure 3.1 – a) Effects of exposing of an ice surface on a ceramic surface held at -44 °C to a 20 keV beam for several seconds. Complete sublimation of the ice can be seen in the middle — rectangular structure originating from a change of the exposed area by a change in magnification. b,c) Ice crystals on an acrylic polymer surface. The beam is used to selectively sublimate a crystal at the centre.

3.2 Effects of Charge and Ionization on Crystal Growth

Crystal growth is strongly affected by the effects caused by the imaging beam. The electron beam not only ionizes the water vapour gas inside the chamber (details in section 2.2) but also electrically charges the growth surface and the crystals themselves.

In general, the ionized chamber gas helps to reduce surface charging and permits imaging of non-conducting specimens. However in doing so, foreign ions, such as oxygen and nitrogen, may be introduced into a growing ice's surface. Because, in addition, at lower pressures not enough ions are available to neutralize all excess charge, strong electrical fields lead to changes in the way new molecules and ionized molecules are attached, especially at sharp edges and corners.

Some unusual crystal shapes and growth effects can be observed (figure 3.2). The effects are less prominent if an electrically conducting growth surface is used, such as copper, and the field of view is large, as when the beam is swept across a wider area and the charge delivered per area onto the surface is smaller.

The only way to rule out any ionization or charging effects affecting the experiment's outcomes is to record only one single image at a time (a high resolution scan can take up to 20 s), as after that it has to be assumed that charging is no longer negligible for the further development of the growth or the sublimation phase of a crystal. If a time series was imaged, I attempted to avoid charging effects by restarting the experiment several times, whilst increasing, for example, the duration of the growth phase before taking a single picture. The time development is established in this way, rather than imaging the same

Material	Outcome
Siliconized glass slide	Complicates imaging due to charging, does not seem to prevent ice nucleation
Copper needle (glass sandwich)	Fails to nucleate at the needle tips
Copper needle (polymer coated)	No difference between the coating and the free tip end
Diamond surface, polished	Not very effective in preventing growth
Acrylic polymer (nail varnish)	Nucleates strongly, easy to apply, brittle
Opticlean (most likely collodion based)	Creates smooth surfaces and is somewhat successful in preventing ice growth; outgassing contaminations are a concern, easy to apply
Patterend silicon	Reduces the number of ice crystals, but thermal conductivity is low
Teflon coating	Difficult to apply, very brittle, does not prevent nucleation

Table 3.1 – List of a variety of materials tested for their nucleation prevention effectiveness.

crystal several times at different times.

If enough time is left between experimental runs, the system will stabilize and ions should either have recombined or have been removed from the chamber gas. Throughout, I used a stabilizing time of 300 s in all experiments before re-running a cycle.

3.3 Limiting and Preventing Ice Growth

One problem in conducting the growth experiments is that ice crystals can nucleate and grow on any sufficiently cold surfaces. I tested a variety of materials to find a material that effectively limits or even inhibits ice nucleation at all locations except for the small imaged region. The general idea was to use a hydrophobic surface or very clean surface and place a nucleation target in the centre of it. Clean siliconized hydrophobic glass was expected to be a very good candidate as it has been successfully used in flow cell experiments and immersion freezing experiments (Murray et al. (2012)).

I found no material that efficiently controlled unwanted ice growth (for a list see

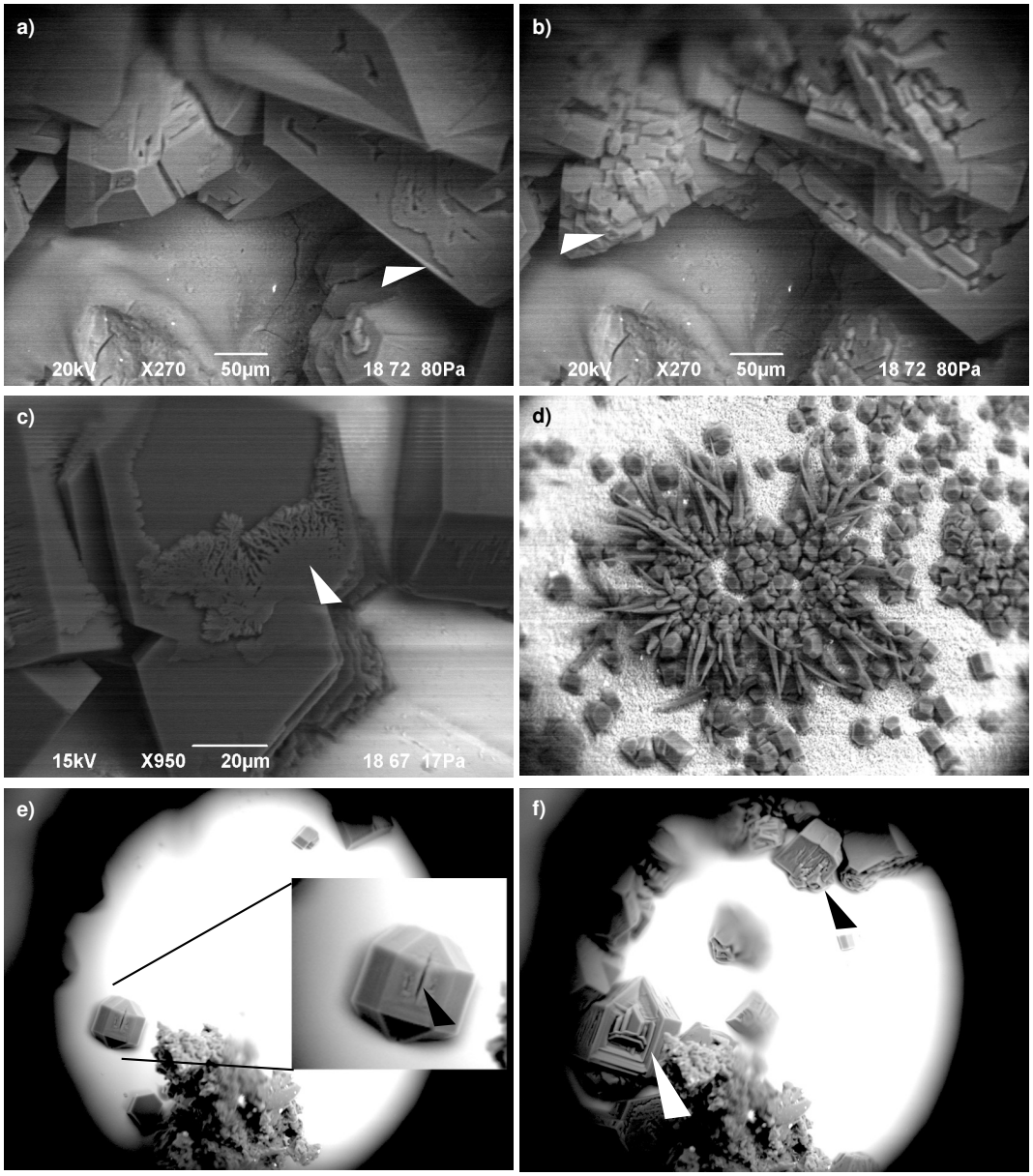

Figure 3.2 – Effects of electrical charging and water vapour ionization due to the imaging beam. The two main effects are charging of the growth surface and crystals, and ionization of the water vapour. a) Formation of a wall on a crystal edge during crystal growth. b) After a further growth period rectangular bulk blocks developed — as imaging changed the conditions. c) Dentritic growth structure on a basal plane. d) Development of spikes on a highly electrically insulating surface (ceramic). e,f) Growth pattern which develops into a macroscopic structure (f bottom left) and surface effects (f top right).

table 3.1). In the end, as high thermal conductivity is important, so the nucleation site is held at the same temperature, a polished clean diamond plate (Element Six, UK) was used as a growth surface together with a heat shield (section 2.15). Furthermore, in the future the optical quality, high thermal conductivity diamond may form the basis for an experiment to investigate the light-scattering on the ice crystal.

3.4 Nucleation Sites

To study the influence of growth conditions while imaging crystals at high magnification, it is necessary to be able to conduct repeated experiments under the same conditions. We hoped that the introduction of a very localized nucleation site in combination with growth preventing measures would limit the ice crystal growth to a small area or even allow us to grow one single ice crystal at always the same location (within a few µm) for imaging. This was only partly successful.

The commonly known good nucleators, such as the clay minerals kaolinite or feldspar, turned out not to nucleate earlier or better in vapour deposition mode. Nucleation would happen at roughly the same time on the surface near a set of mineral dust grains, for example. This might be due to the not ideal thermal contact of the grains and/or their radiative properties: they might have been slightly warmer than the growth substrate due to absorbed radiation emitted by the relatively warm chamber cover.

Other attempts to generate a modified surface to facilitate the ice nucleation, comprise: a laser-altered siliconized glass surface; introducing small diamond grains with defects into a copper surface; and causing localized damage to polymer coatings using an e^-- beam, and damage to siliconized glass surfaces using a laser. For an overview see figures 3.3 and 3.4.

For the laser-altered glass surface, I attempted to melt a micron sized hole into the glass surface to create a pore as a nucleation site. The attempt, with the available UV laser equipment failed, as not enough power at a laser wavelength of about 370 nm could be generated using an up-converted pulsed laser setup. In a second attempt a commercial CO_2 laser cutter (S300, Trotec, US) with a wavelength of 10.6 µm, 60 W was used to puncture the surface. This destroyed

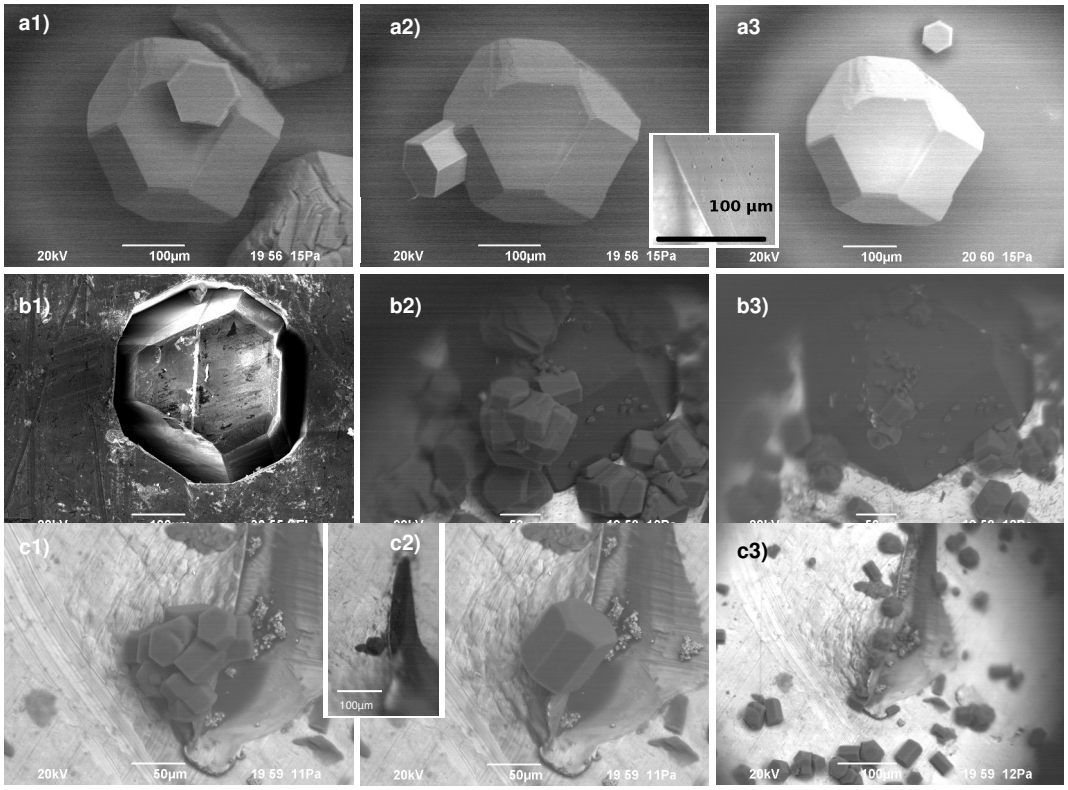

Figure 3.3 – Nucleation sites overview panel I: a) Diamond on diamond surface. Ice would only sometimes grow directly on the diamond, which has some $\approx$ 1 µm size hole defects (inset) on its facets. b) Diamond mechanically pressed into a copper surface. The nucleation happens at the copper surface as well as on the diamond. Some crystals nucleating on the diamond are smaller. c) A copper surface with a spike produced using a scalpel, then parylene coated. The extremely hydrophobic parylene coating does not prevent crystals from growing. Inset: using the electron beam, the parylene coating was removed, but no nucleation would occur on the copper of the exposed tip; instead, nucleation would occur at some edges and corners.

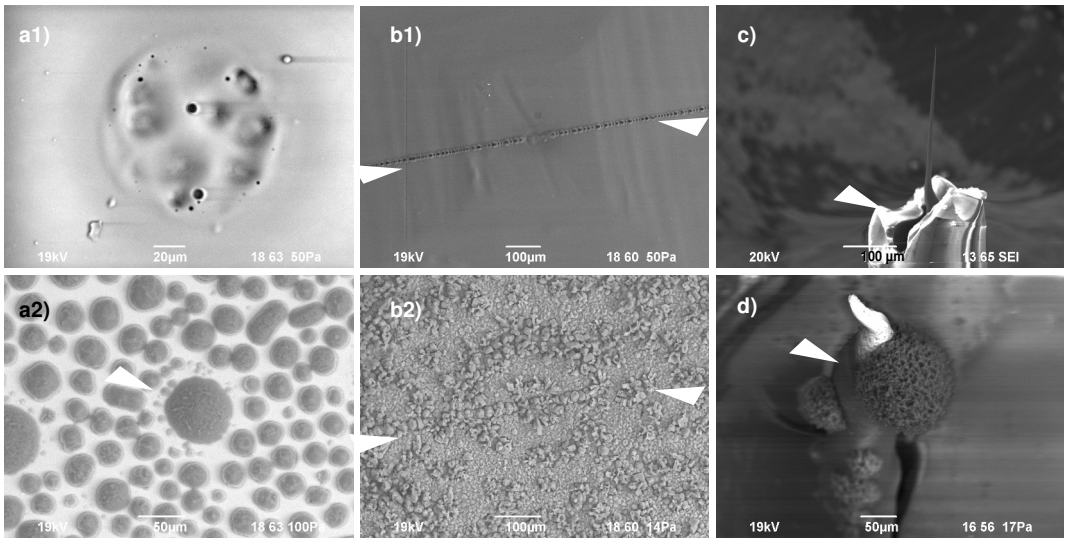

Figure 3.4 – Nucleation sites overview, panel II: a1) A laser was used to destroy the silane coating of a glass slide, removing the hydrophobic coating. a2) Crystal formation on the glass slide (likely via super cooled droplet). The damaged area is seen as the larger crystal in the middle. b1) Copper coated with an acrylic polymer and a line of small holes created using the electron beam. b2) Nucleation occurs similarly over the whole area, but along the the line and the centre edges larger crystals are visible. c) A copper needle sandwiched inside a glass micropipette, no ice would nucleate on it. d) A copper needle coated with a soft polymer (Opticlean) with exposed tip. Ice nucleates along the whole needle, not only at the tip.

the silane coating over an area of 100 µm and also led to the formation of micrometer sized pores, when the glass melted and formed small bubbles that burst. However there was no big difference on crystal growth between the intact coating and the destroyed coating, so this option was not further pursued.

Further, I tested a variety of tip setups as nucleation sites. The methods for manufacturing described in section 2.14 were used. The tips were mounted (soldered) onto a small copper plate and then the assembly is coated using two different polymers: Opticlean (no longer manufactured[1]), which stays soft, and a hardening acrylic one[2]. A different copper needle was manufactured by inserting the copper wire into a fine glass micropipette, creating a glass coating. In general, if the tips were too thin, they would not nucleate at all. Copper tips coated with a polymer would grow ice crystals on the coating, as well as on the tips. A similar result was obtained with the glass needle, where the ice develops on the glass and the borders between materials.

Another type of tip was manufactured using a scalpel to raise a small spike from a copper plate. The plate was then parylene coated to make it hydrophobic and the coating at the tip was destroyed by long exposure of this area to an electron beam, exposing the original copper. Also this target did not perform as hoped: ice would grow at the surface instead of the tip, preferably on the edges. After destroying a part of the coating mechanically, exposing the copper, crystals would grow side by side on the coated and exposed areas. The parylene coating technique is promising, as it is easy to apply (at room temperature) and can also be controlled in thickness. So it might well be possible, with further trials, to find a suitable geometry and material combination to manufacture a growth target.

3.4.1 Mineral Dusts

Kaolinite is a clay mineral known to be a good ice nucleator (IN). It is widely used as an IN standard in the research community, as it can make up a considerable fraction (up to 50%, together with illite) of airborne dust particles (Claquin et al. (1999)). Recently, it has been shown that for immersion freezing ice, feldspar is more efficient (Atkinson et al. (2013)). So this material was considered a good candidate as a nucleation target. Particles were glued with epoxy onto a

[1] A peel-off nail varnish for children by Claire's, UK might be a similar material
[2] Transparent nail varnish

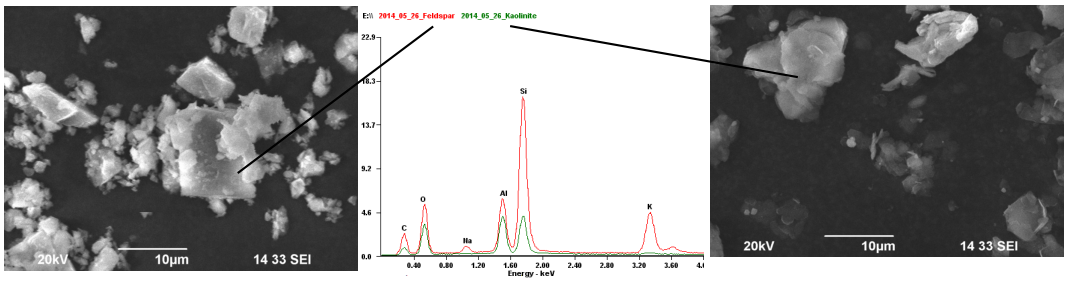

Figure 3.5 – SEM micrograph of feldspar (left) and kaolinite (right). Energy-dispersive X-ray spectroscopy composition analysis (middle) shows that the two materials are not easily distinguished from their structure, but their Al/Si ratio is substantially different (feldspar in red, kaolinite in green).

siliconized and hydrophobic glass slide and mechanically transferred onto the diamond surface.

For an inter comparison experiment I asked the question if was possible to distinguish feldspar ($KAlSi_3O_8$-$NaAlSi_3O_8$-$CaAl_2Si_2O_8$) and kaolinite ($Al_2Si_2O_5(OH)_4$) easily when the powders are mixed. It is not possible from the pure shape or structure of the two minerals (see figure 3.5), but energy-dispersive x-ray spectroscopy (EDAX) allows us to distinguish between the minerals quite clearly (figure 3.5) by their Al/Si ratio and the presence of a potassium peak.

Using epoxy to fix one or several grains on a siliconized surface does not work very well, as the epoxy does not bond with the surface layer of the siliconized glass and grains do not attach well, which makes the transfer from a microtip to the epoxy dot difficult. Grains can simply be washed off, including the cured epoxy, by simply rinsing the slide with water.

In a sequence using different growth times, crystals would nucleate in the surroundings of a small area of kaolinite placed on a diamond surface, but only in one case directly on a grain (figure 3.6). The cause of this is not understood, but could again be linked to the grains being warmer than the surrounding area.

3.4.2 Beam Exposed Area on Diamond

A growth sequence (figure 3.7) was recorded after a section of the diamond surface had been exposed to the electron beam, which accidentally was not switched off for several minutes. The recorded sequence clearly shows that ice

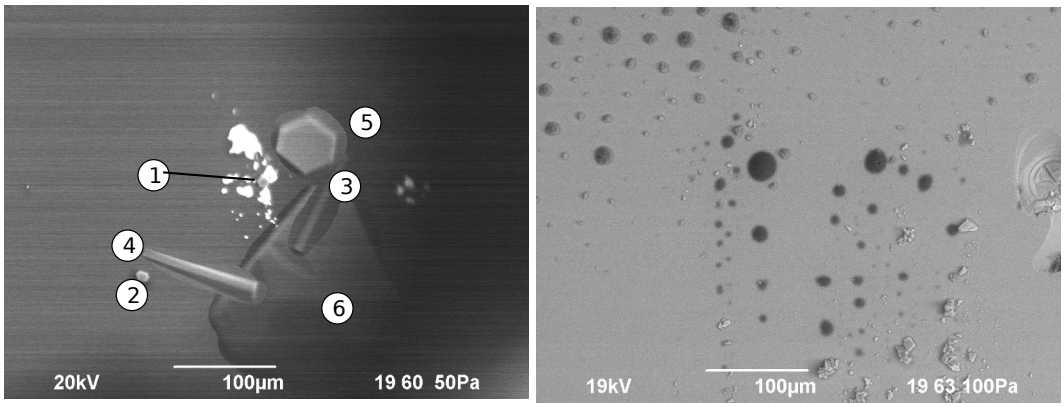

Figure 3.6 – Nucleation targets feldspar and kaolinite. Left panel: superimposed image of several runs at $T_{ice} = -31$ °C, saturation ratio S_i ≈1.15, growth times $\{80, 100, 130, 200, 250, 300\}$ s (1-6) on the diamond surface. Crystals formed around the mineral dust targets and only in one case (1) directly on a grain. Right panel: mix of feldspar and kaolinite attached with epoxy on the siliconized glass surface. There is no preferential formation of ice crystals on the grains. The formed ice has nucleated via supercooled droplets, which formed through condensation when lowering the surface temperature starting from above 0 °C, imaged at $T_{surf} \approx -42$ °C.

crystals nucleate only on the area that was previsously exposed to the electron beam. The reason for this is unknown, but it is known that after long imaging beam exposure, the deposition of hydrocarbons leads to darkening of the imaged area, as discussed previously (Egerton et al. (2004)). So it seems very likely that chemicals deposited could be the cause of the nucleation behaviour, as the electron energy is not high enough for a structural change of the diamond. An electrical charging effect seems unlikely due to the fact that the nucleation behaviour was observed 30 min after exposure. This sample was not re-imaged on another day.

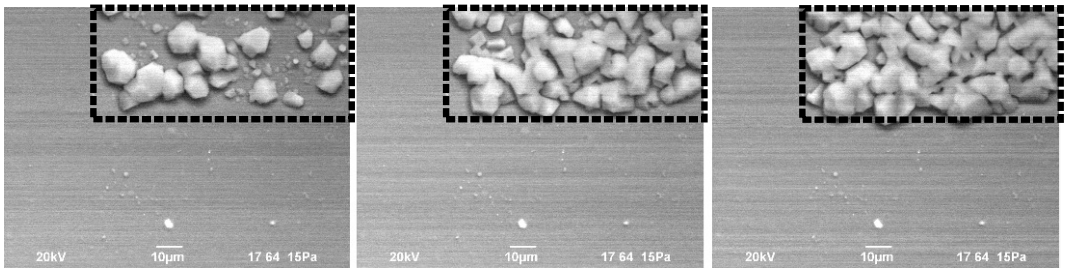

Figure 3.7 – Ice growth experiments on a diamond surface, previously exposed to the imaging beam for several minutes in the marked area (dashed lines). After initial nucleation periods of 4, 5 and 6 s (images left to right) at $S_i \approx 1.14$, crytals are grown a further 120 s at a saturation ratio of $S_i \approx 1.07$, $T_{ice} = -43$ °C.

3.5 Progressive Growth Sequences

The following section describes two examples of the experiments I used to study crystal growth. A short peak saturation is needed to initiate crystal growth; after this nucleation phase, the crystals are grown at a saturation ratio of 1.1 and 1.17 (figures 3.8 and 3.9, respectively). To obtain a time series equivalent, but at the same time only image once, the full experimental run is repeated several times, always starting from an equilibrated system and repeating the same nucleation phase and growth phase several times. Images are taken at different, increasing time intervals (5 or 10 s) in the individual runs. The runs are separated by an equilibration time of 300 s.

The quality of the crystals shown in the two examples is very different. In the first example, a complex collection of crystals form. In the second growth sequence (figure 3.9), only one crystal nucleates and grows near a step in the surface. So far, no determinant factors have emerged, that allow us to reliably predict the likely outcome of an experiment. Consequently, the overall conditions governing crystal growth are not controlled sufficiently well. Although it appears that in the present case a more complex crystal geometry emerged following growth at higher saturation ratio, it is not possible to ascribe the differences in crystal morphology solely to this single factor. A greater number of experimental runs are needed in the future.

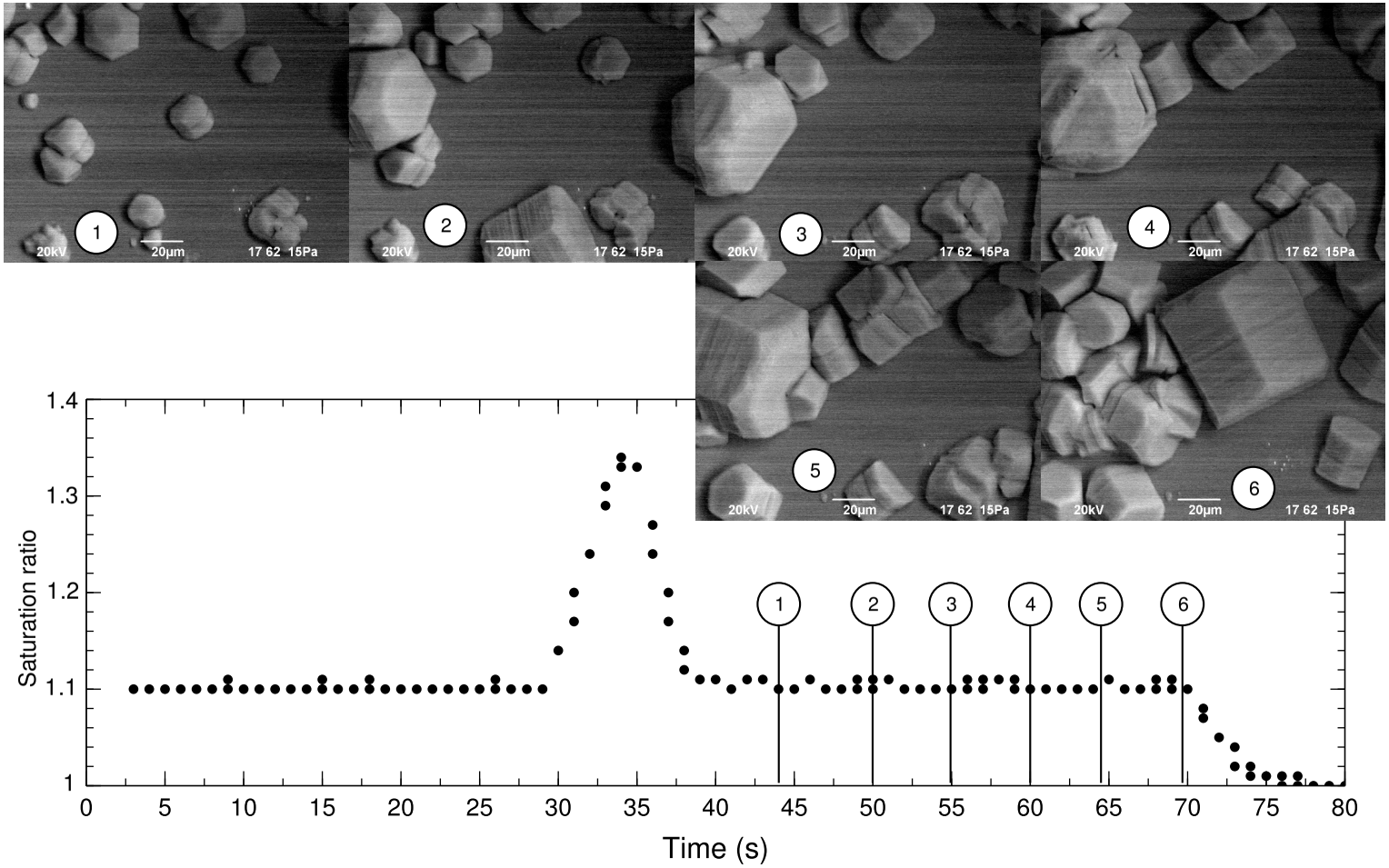

Figure 3.8 – Crystal growth example I. After a nucleation peak, crystals are grown for 10, 15, 20, 25, 30 and 35 s at a saturation ratio $S_i = 1.1$. Every image is the result of an individual run of the experiment, separated by a 300 s equilibration phase from the next run. The surface material is diamond with some kaolinite dust grains, $T_{ice} = -43$ °C.

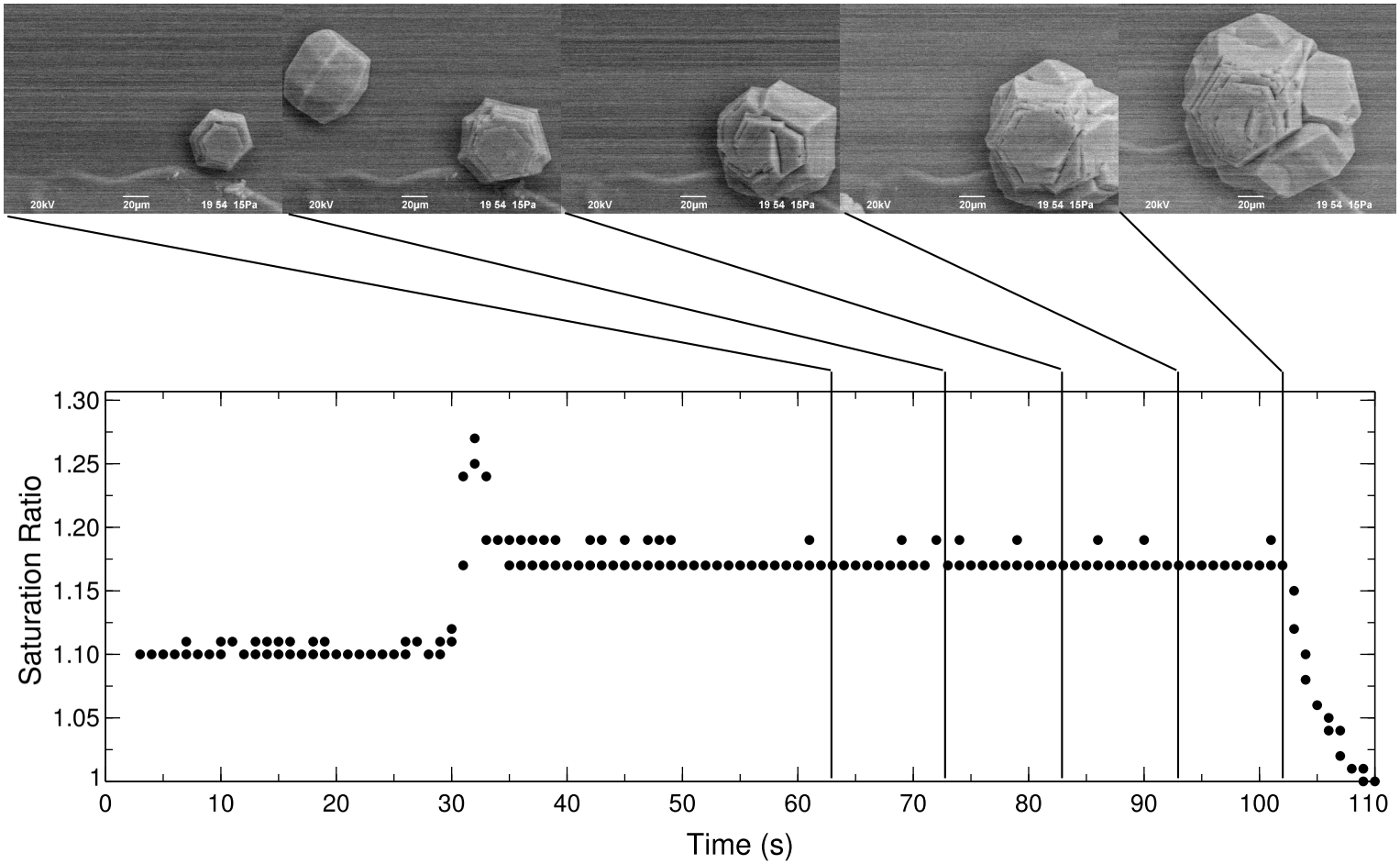

Figure 3.9 – Crystal growth example II — higher saturation ratio than in figure 3.8. After a nucleation peak, crystals are grown for 30, 40, 60 and 70 s at a saturation ratio ($S_i \approx 1.17$). Every image is the result of an individual run of the experiment, separated by a 300 s equilibration phase from the next run. $T_{ice} = -43\,°\mathrm{C}$.

3.6 Sublimation Sequences

During my experiments, I found that it was relatively easy to cause surface roughening through fast sublimation. Fast sublimation can be initiated by lowering the pressure in low vacuum mode by more than 30 Pa, or switching the vacuum system to high vacuum mode, in which the system will try to lower the pressure using the turbo molecular pump. These observations are in keeping with results from previous work by Cross (1971) (and Cross (1969)) and has also been described by several other groups (Rosenthal et al. (2007), Cullen and Baker (2001) and Barnes et al. (2002)).

Examples of the structure of the roughness that is observed are given in figure 3.10, which shows a time series of sublimation, imaging of roughness caused by sublimation through fast pumping, the sublimation result of a crystal grown on a coated copper needle, and structurally different types of rough crystals grown on patterned surfaces. In general, the development of a spiky ice surface can be observed equally on prismatic and basal facets. Although such huge and abrupt pressure changes are not very representative of the atmospheric case, the structures give some idea of the scale of the roughness occurring on the surfaces.

The second type of roughness that I observed, is stripy patterns along the facets parallel to the crystal's c-axis, similar to the already-described kinks, but more numerous and not developing in such a regular manner. Other observed types are block shaped patterns on facets during growth and grooves along edges (figure 3.11).

Stripy patterns can also be seen in figure 3.13, which shows an example of a time series of sublimating crystals. Crystals are grown for 80 s and left to sublimate. An image time sequence is obtained in a similar, already described, manner by re-running the experiment several times.

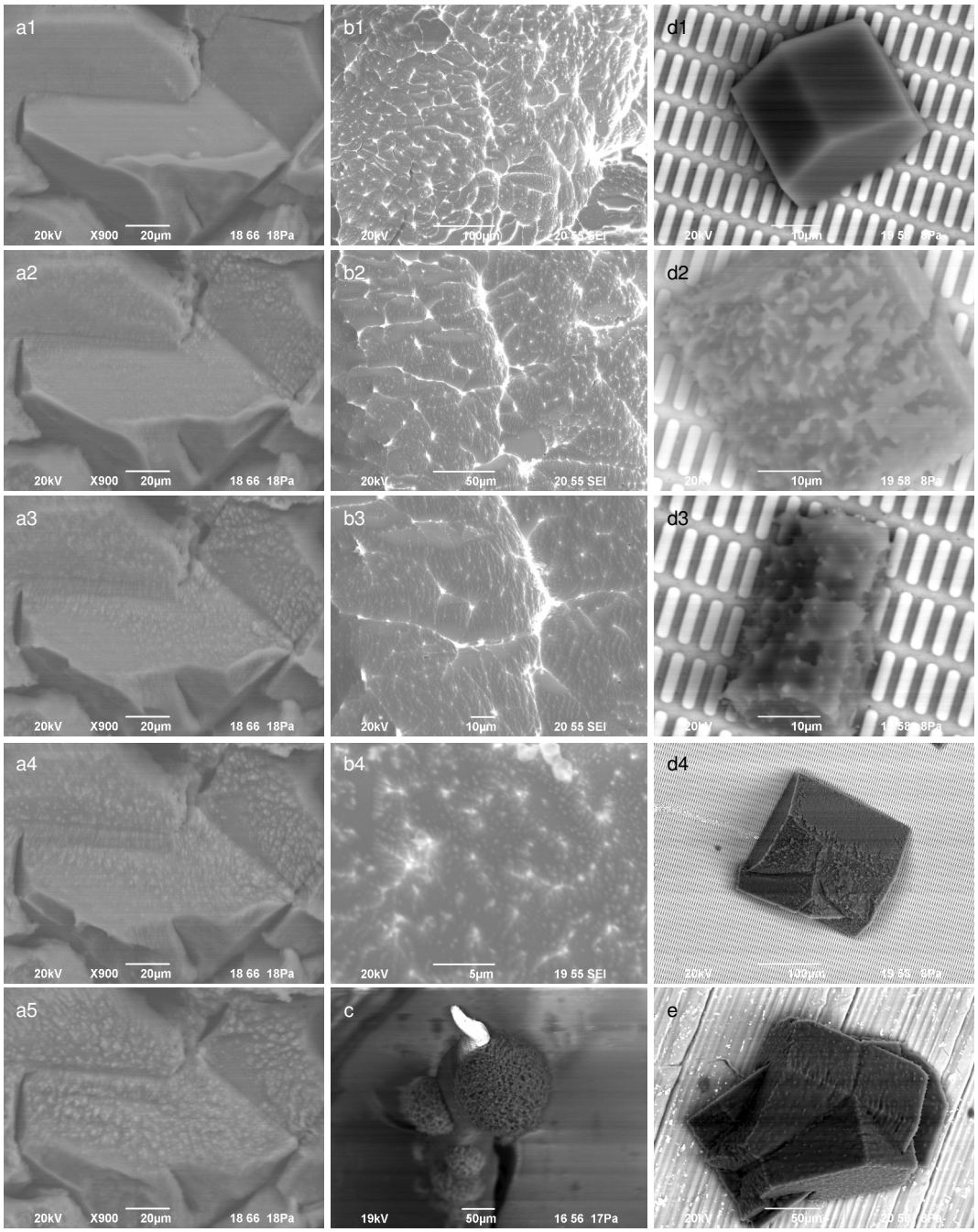

Figure 3.10 – a) Sequence of the development of roughness through fast sublimation initiated by lowering the pressure and pumping the chamber (a1-a5). b) Structure of roughness developing when switching the vacuum system to high vacuum and pumping the chamber, whilst imaging with the secondary electron detector (b1-b4). c) Rough remains of a crystal growth on a coated copper tip after sublimation. d) Crystals grown on a patterned silicon surface and sublimated (d1-d4). e) Sublimation result of a crystal grown on an aluminium surface.

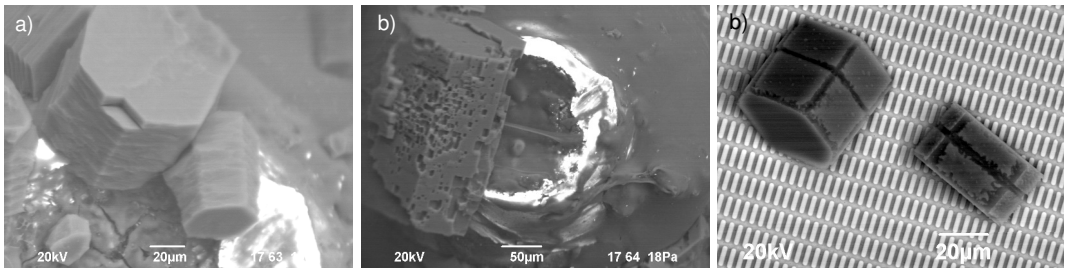

Figure 3.11 – Observed roughness features. a) Stripy patterns along facets parallel to the crystal's c-axis after sublimation on a patterned silicon surface. b) Block shaped patterning of facets during growth. c) Grooves along the edges during sublimation. The bright areas in a) and b) are exposed metal from a turntable stylus, without the diamond tip. Dark areas are polymer coated.

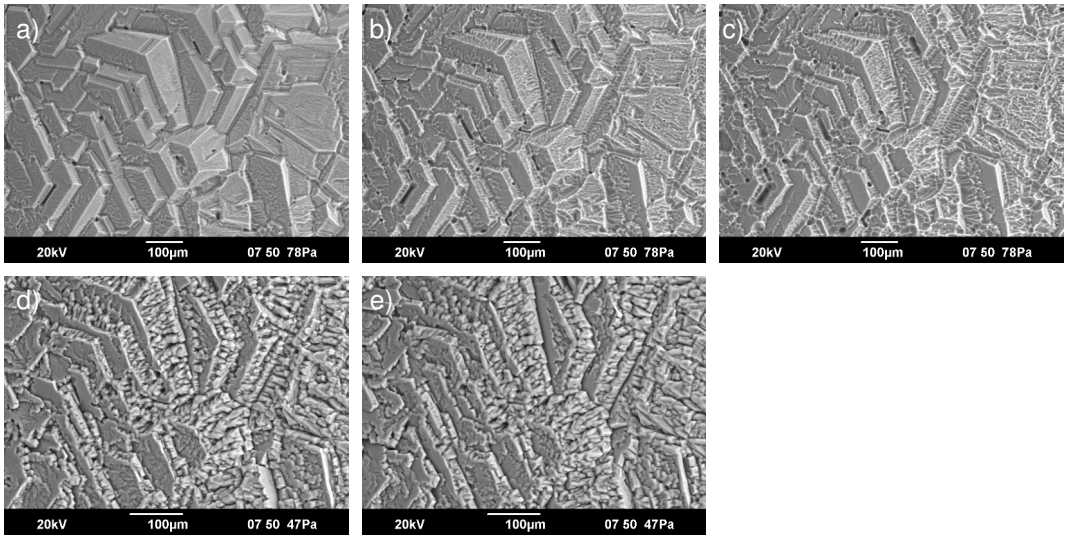

Figure 3.12 – Complexity increase after regrowth following sublimation. A sequence of images depicting the increase in complexity (a vs. e) after crystals are re-grown following a sublimation phase (a-c). Temperature data not recorded. t=0, 90, 410 and 500 s (left to right)

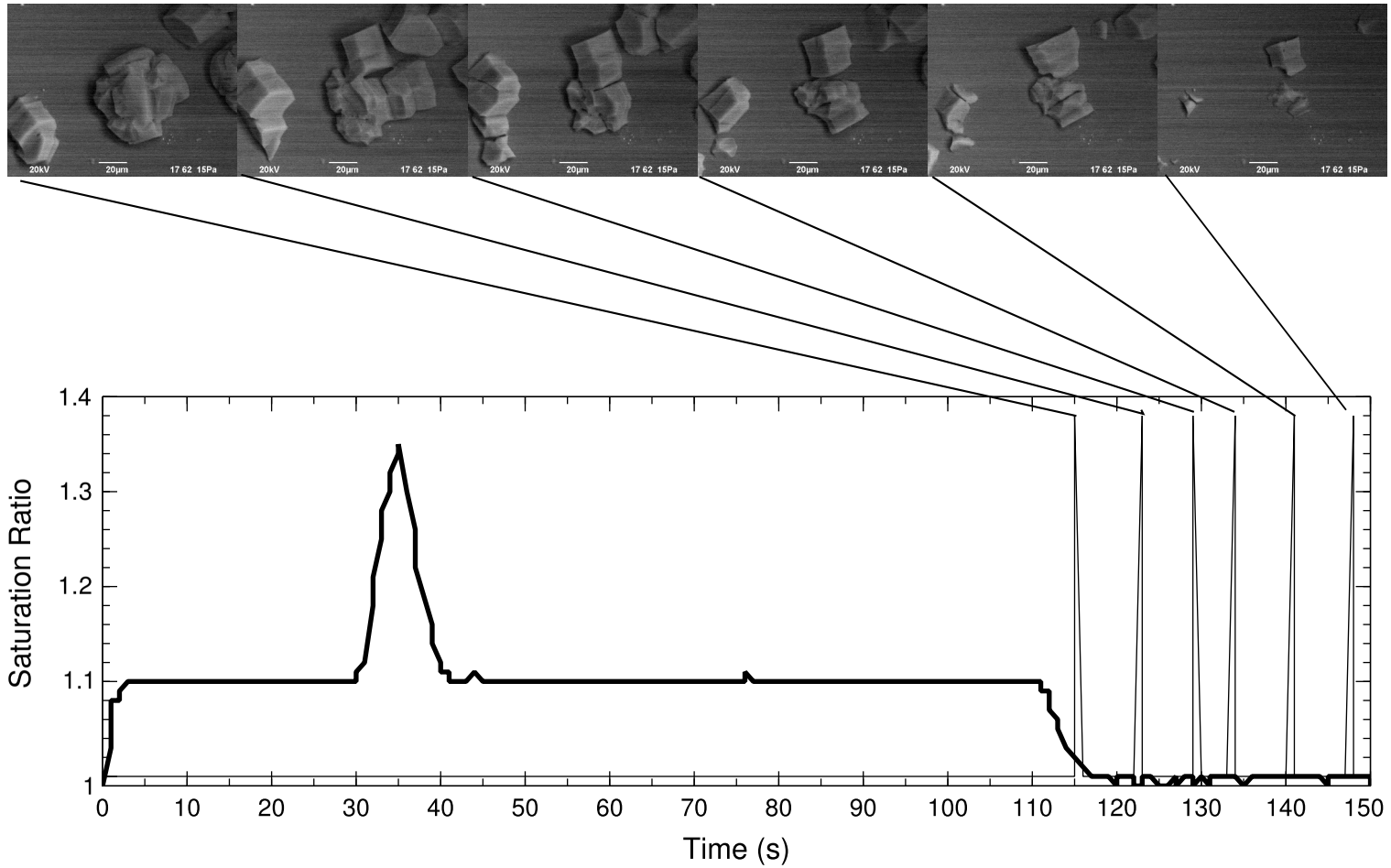

Figure 3.13 – Sublimation time sequence. After a nucleation peak, crystals are grown for 80 s at a saturation ratio ($S_i = 1.1$) and then left to sublimate. Images are taken at 5 s intervals and every image is the result of an individual run of the experiment. Experimental runs are separated by a 300 s equilibration phase. $T_{ice} = -43$ °C.

3.7 Cyclic Growth Series

Sublimation and growth cycles are considered important, as in atmospheric conditions, crystals can repeatedly travel through super- and subsaturated regions in the clouds. So, one question is how the growth history affects complexity or the development of roughness. Previous preliminary observations (figure 3.12) and results from other experiments conducted in flow tubes (section 1.3.1) demonstrate the importance of cyclic growth.

To investigate such sublimation/growth cycles, a more complex experiment was designed, as shown in figure 3.14. In this run, crystals are grown for 80 s, sublimated for 20 s and then re-grown, with images taken in 10 s intervals after the start of the second growth phase. It can be seen that the results are not separate crystals, rather more complex structures. More experiments are required, to determine the conditions and parameter ranges in which cyclic growth leads to an increase of complexity or surface roughness.

In general, it is difficult to find experimental parameter settings which result in successful sequence experiments. Many times, several parameter study runs that varied only a single parameter were required, before useful settings could be established. In addition, when using the same settings and materials, sometimes experiments were not reproducible. Explanations for this could be that by re-loading the small diffusion chamber with water, changes to the configuration are introduced and that changes in room and the microscope's temperature need to be considered and monitored and better controlled.

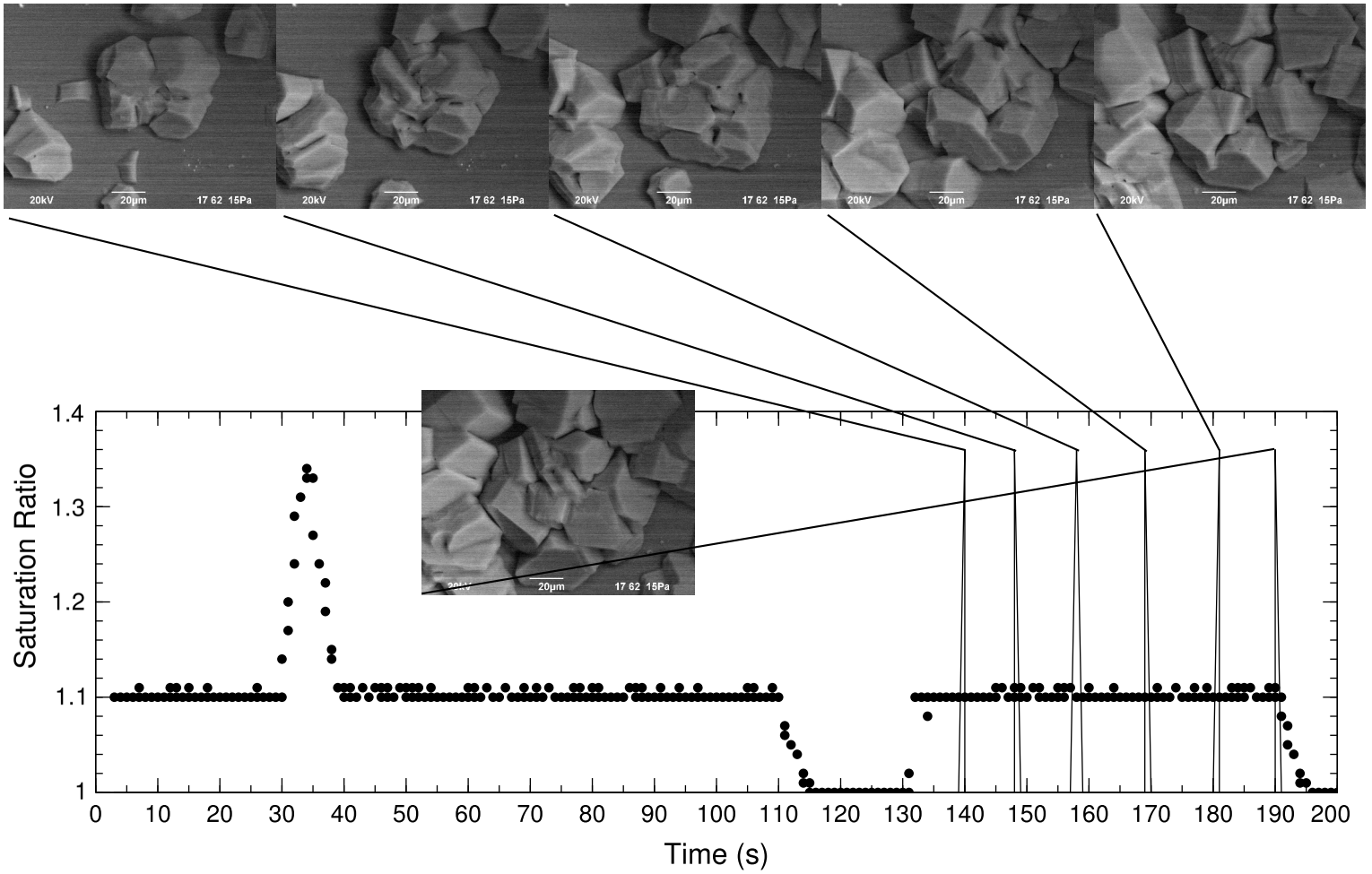

Figure 3.14 – Time series of a cyclic growth experiment. Crystals are first grown for 100 s, then left to sublimate for 20 s, and then re-grown again. Images are taken at increasing times of individual runs, separated by a 300 s equilibration phase. $T_{ice} = -43$ °C.

Chapter 4

General Discussion and Outlook

Several issues have emerged during the development of the experiments described in this thesis. Imaging the growth dynamics of small water ice crystals in a low pressure environment using an electron beam is challenging for several reasons. The control of pressure and temperatures inside the imaging chamber of a scanning electron microscope is not easily achieved without a re-design of the microscope's vacuum system, as introducing water vapour into the imaging chamber affects the microscope's pressure control-loops by influencing the pressure sensor readings.

The electron beam interacts with the water vapour causing ionization of the chamber gas, which helps to neutralize charge accumulated on the imaging targets. However, in doing so it may affect ice growth by the deposition of oxygen and nitrogen ions on the growing surface. Charging of the imaging target (crystals and growth surfaces) can still occur at lower pressures, when not enough ions are available to remove excess charge. Further, the water vapour reduces contrast and resolution, which complicates imaging especially at high vapour pressures.

Nevertheless, despite these technical difficulties, which can be overcome, as discussed in the sections on the experimental setup, it has also become clear that the method is capable of revealing the surface morphology, if appropriate precautions are taken concerning the crystal growth.

The charging and ionization effects, detailed in the section on the environmental scanning microscopy, strongly affect the molecule attachment to the bulk phase. This can only be prevented by imaging the results once, as the system must be

considered as potentially altered by the first electron beam exposure, and subsequent results are no longer free from unwanted influences.

Radiative heat exchange must be prevented from affecting the crystal growth. During SEM imaging, chamber walls can reach temperatures as high as 38 °C, due to instrument warming. Hence, radiative effects can be a major source of unwanted effects.

Even if an optimal SEM imaging setup is built, questions will remain. A technically ideal system is one that implements precise and fast control of the environmental parameters over a wide range of pressures (≈1–1000 Pa) and temperatures (-90–0 °C), is free from any radiative interactions, has a well defined small nucleation zone for repeated imaging and is able to resolve submicron structures, noise free in the presence of water vapour even at high pressures and with enough contrast.

Revisiting the initial questions we set out to investigate at the beginning, the results can be summarized as follows.

Addressing the last question first: “What is the effect of repeated growth and sublimation cycles is, i.e. if there is an influence of the growth history on crystal morphology?”. The experiments investigating repeated cycles of sublimation and growth following each other show that the crystal complexity can change and increase. In some cases this leads to a complexity increase originating from the formation of many small crystals. An example of this behaviour is shown in figure 3.12. A regrowth phase following a sublimation phase can also increase the prevalence of hole inclusions and in general lead to an increase in the complexity of the crystals, as they can develop from a single into a polycrystalline geometry. This is similar to the case mentioned previously caused by growth from the different structures developing after the sublimation period. As the crystals grow larger, they join into a complex geometry. However, given the small number of experimental runs, no single determining factor that governs the exact behaviour can be isolated.

The effect of sublimation on the surface morphology is substantial if the sublimation is fast and initiated by lowering the pressure through pumping of the chamber. Perfectly smooth crystal surfaces develop a highly rough surface with structures at sub-micrometer scale (figure 3.10). The influence is less prominent for the second frequently observed type of roughness: stripy patterns along the facets parallel to the c-axis as they can be seen in figure 3.11 and figure

3.13. It seems that the development of this type of pattern could be amplified through radiative effects on the crystal surface, especially if the crystal is near the equilibrium saturation. One interesting case of grooves that develop along edges of a hexagonal column during sublimation was observed (figure 3.11c), but the mechanism of the development is as yet unknown.

The question of the structure of roughness can be answered qualitatively for the cases observed. It is not yet possible to create a link between physico-chemistry processes involved at a molecular level and the macroscopic effects. Theoretical simulations cover size scales in the order of several lattice layers, which is orders of magnitudes smaller than a micrometer sized specimen. Experimentally, single layers or a small numbers of lattice layers can been observed for example using atomic force microscopy techniques, but scanning electron microscopy does not allow for this level of detail. The matter is further complicated by the fact that some ice consists of a mixture of hexagonal and cubic lattice arrangements. If one was to speculate, it seems possible that some of the observed roughness patterns are a macroscopic manifestation of a lowered binding energy at the location where the lattice structure is not purely hexagonal, which would explain the orthogonal orientation of the patterns on the facets parallel to the c-axis (figure 3.11 and 3.13). Further observed types of roughness structures are kinks (figure 1.4c) which run like a belt around the crystal. Often there is only one kink present around the centre of the crystal, but many crystals containing several kinks have been observed. The third type of roughness that is observed is of rectangular block type (figure 3.11b). The facets of a hexagonal column are covered with rectangular holes and elevations. The origin of this is uncertain, and it is not a frequently observed structure.

The question if fast growth leads to the formation of roughness or complex crystals largely remains unanswered for now. The problem of not having been able to find a good single nucleation target and suppressing ice growth everywhere else, makes it very difficult to observe growth at high super saturations. Ice forms at many unwanted locations which leads to a fast depletion of water vapour, before the effects on the targeted crystal can be observed. Further refinement of the experiment and materials used should allow to overcome this problem and permit to investigate growth at high super-saturations.

This leads to the first and last question: which changes in the environmental

parameters cause the development of surface roughness. This question must largely also remain open, as no conclusive pattern which could be translated into a model has emerged from he experiments done so far. A much larger set of experimental runs is needed to further investigate this. It has become evident from the experiments that cyclic changes between a growth and sublimation regime can change the crystal roughness and their complexity. This implies that the history of the environments, especially sublimation phases, an atmospheric ice crystal is subjected to can play a role in changes to its light scattering properties.

One further remaining question is how representative the growth of the crystals on a nucleation substrate is for atmospheric application, where the ice crytals are not in contact with a heat reservoir. The vapour deposition mode of nucleation still needs further attention, as the theoretical descriptions do allow predicting how well a certain material will nucleate in experiments. It is also unclear how and if the nucleation material's chemical and surface structure influences the macroscopic growth results. From my experiments investigating nucleation targets, it seems that the geometric structure of the particles, or nucleation sites might be of importance in addition to the crystallographic structure of the materials.

The results of my experiments on finding a suitable nucleation site have shown a case in which the prolonged exposure of a diamond surface to the imaging beam, led to changes which resulted in the ice preferentially nucleating at this rectangular window. Incidentally, here an interesting fact is that in cloud seeding applications the silver iodide is dispersed into the atmosphere using a burner. So one could hypothesize that the hydrocarbons are enhancing AgI's effectiveness in ice nucleation.

Another question is how the presence of a heat reservoir connected to the crystals growing on a surface affects the crystal's development, as for atmospheric ice this additional heat flow is absent and the only interaction of the crystals is radiative and with the surrounding gas.

A further concern are chemical contaminations (Hallett and Mason (1958), Odenkrantz (1968)): ice growth has been found to be affected by trace contaminations with concentrations as low as 1 ppm acetic acid (Knepp et al. (2009)), although this is currently tested by other groups who claim no altered growth for a contaminant level of 1–10 ppm for a variety (but limited list) of

substances[1]. They also state that experiments have only been done at relatively high temperatures of -25 °C and it is likely that at colder temperatures ice growth is more strongly affected by contaminations.

It is very difficult to maintain a completely clean environment with a complex setup. Only a very meticulous and rigorous choice of materials can achieve this. For example, in one of the experiments residues from cleaning a glass growth surface with a commercial isopropanol resulted in ice fingers spreading on the glass surface. A set of experiments though could investigate the effects of contaminants, but this will need full control over the vacuum system in order to introduce the contaminations; with an experimental setup as described here, this would be difficult to achieve.

Further experiments will need to cover the (already very limited) p-T space more systematically. The temperature range can be extended to lower temperatures (-90 °C) relatively easily by switching the diffusion chamber cooling to the circulation bath with a specified range of -90–30 °C, bypassing the Peltier driven coolstage.

Another improvement could be to include a means of simultaneously registering angle-dependent light scattering data by including laser diode based scattering measurements into the chamber. This would permit to directly measure the scattering phase functions and bypass the pathway of extracting the crystal geometry and surface roughness and then determining the scattering properties numerically from this information.

Another improvement could be to incorporate a flow of water vapour, simulating ice crystals falling through a cloud. In this case the growth would no longer be strongly diffusion limited, as a constant new supply of water vapour will reach the interface.

In general, given that the crystallization experiments are very difficult with respect to ruling out unwanted influences and that theoretical physical-chemistry methods are not able to accurately reproduce ice crystal growth, it might be that in-situ measurements are a more accessible approach to derive the required light scattering data. This is also supported by the fact that at the moment, to establish the link from single crystal geometry and surface morphologies, computational light scattering models, with their limitations for

[1] Libbrecht and Bell (2011)

larger crystals, are the only possibility.

Ideally, one would be able to use a high resolution imaging possibility inside a cloud. This would remove many problems connected to the uncertainties on the growth mechanisms, and would allow obervational data to be collected and catalogued. These data could be used in models until the knowledge on the ice crystal growth and interface kinetics has caught up and light scattering models have advanced to a stage where the light scattering properties of an ab inito computationally grown crystals can accurately be computed. However, the major disadvantage of this approach is the connection between crystal morphology and scattering properties on the one hand, and atmospheric variables such as humidity, would be weak because the growth history of any individual crystals would be difficult to establish.

Finally, it has also become clear that only a strong collaboration between several scientific fields of physical chemistry, mathematics, physics and atmospheric sciences will allow us to improve our understanding of the cloud systems and with this the climate processes. The ice crystal structure and growth phenomena are very much a physical-chemistry and a crystallography problem, electromagnetic scattering involves the methods of solving the partial differential equations with correct boundary conditions numerically or analytically for the given shapes and crystals, but the knowledge on how to link these to climate is predominantly situated in the atmospheric research community. It is a matter of finding and accessing the domain specific knowledge and transfer it to the climate science for mutually beneficial application.

Efforts to join up scientific collaboration across fields are already under way with several newly created centres of excellence in the atmospheric sciences which hold promise to generate new ideas, develop new techniques, interpret results and advance our knowledge of the fascinating phenomena occurring when molecules of water form ice in our atmosphere. Last but not least it is to be hoped that the outreach to the leaders of the world will eventually be successful, helped by enhanced scientific evidence, and a change in the anthropogenic influence can be achieved.

Appendix A

Wigner Flow in Quantum Mechanics

I contributed to a project of the theoretical quantum optics group at University of Hertfordshire, led by Dr. O. Steuernagel. The project investigates quantum mechanical systems using a quasi probability density formalism known as the Wigner formalism. Dynamics and quantum effects of bound states, such as tunnelling for example, are studied within this formalism using the techniques similar to the phase space methods used to investigate classical dynamic systems.

My contributions include porting computations to the university's high performance cluster. This includes the parallelization of existing code, developing the scripting framework, writing the data output management routines and conducting parts of the computations. In addition, to be able to study and present the numerical results, I facilitated the data import into the scientific visualisation package Vish (Benger et al. (2007)) and created visualisations.

The results have been published in the Physical Review Letters: O. Steuernagel, D. Kakofengitis, G. Ritter. Wigner Flow Reveals Topological Order in Quantum Phase Space Dynamics, 110(3), 2013.

A.1 Introduction

A classical mechanical system is fully described by its Hamiltonian H, which is obtained from the Lagrangian L by Legendre's transformation (e.g. Landau and Lifshitz (1969)) in the established way,

$$L(q_i, \dot{q}_i, t) = T - U \tag{A.1}$$

$$p_i = \frac{\partial L(q_j, \dot{q}_j, t)}{\partial \dot{q}_i} \tag{A.2}$$

$$H(p_i, q_i, t) = \sum_j p_j \dot{q}_j - L(q_i, \dot{q}_i, t) \tag{A.3}$$

with $i = 1, 2, \ldots, N$ for an N-dimensional system, T being the kinetic energy of a free particle of mass m and U the potential energy term of the system. The generalized coordinates and velocities are q_i and $\dot{q}_i := \frac{\mathrm{d}q_i(t)}{\mathrm{d}t}$ respectively, and p_i denote the conjugate momenta. In this setting the canonical or Hamilton's equations of motion in variables q_i and p_i are

$$\dot{q}_i = \frac{\partial H}{\partial p_i} \tag{A.4}$$

$$\dot{p}_i = -\frac{\partial H}{\partial q_i} \tag{A.5}$$

$$-\frac{\partial L}{\partial t} = \frac{\partial H}{\partial t} \tag{A.6}$$

Finding the solution of the problem requires integrating these $2N + 1$ first order differential equations (for a conservative system $\frac{\partial H}{\partial t} = 0$). The solutions are the curves $q(t) = (q_1(t), \ldots, q_N(t))$ and $p(t) = (p_1(t), \ldots, p_N(t))$ with parameter t, typically time.

Plotting a representative set of these curves in phase space spanned by pairs $\{q_i, p_i\}$ results in a phase portrait (figure A.1) which is a useful technique to understand the structure and dynamics of a system. By analysing the topological structure, such as fixed points or separation lines, systems can be compared or their stability analysed. Spirals, vortices and saddles (figure A.1) are topological structures which are associated with these points.

If the single particle classical framework is extended to a statistical theory, a phase space density $\varrho(p, q; t)$ is used. Liouville's theorem, which states, for conservative systems, that $\varrho(p, q; t)$ moves as if transported by an incompressible fluid, can then be stated in the form of a continuity equation

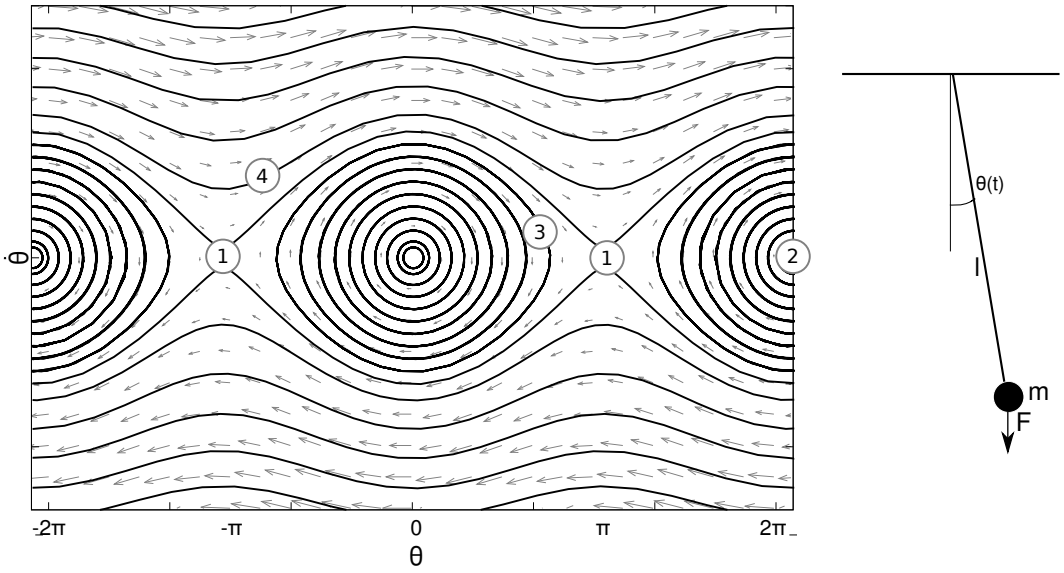

Figure A.1 – Illustration of the phase portrait of an undamped pendulum. The four types of solutions are easily recognisable: Periodic small oscillations (3), stationary solution at (1) and (2), saddles at $(\pm\pi, 0)$ and centres at $(\pm 2n\pi, 0)$ respectively, and rotations around the axis (4). Arrows depict the phase space flow field.

using the anti-commutative Poisson brackets, defined as follows

$$\{f, g\} \coloneqq \sum_{i=1}^{N} \left(\frac{\partial f}{\partial q_i} \frac{\partial g}{\partial p_i} - \frac{\partial f}{\partial p_i} \frac{\partial g}{\partial q_i} \right) \tag{A.7}$$

where $f(p_i, q_i, t)$ and $g(p_i, q_i, t)$ are functions on the phase space. Consequently, the time evolution of $\varrho(p, q; t)$ can be written in the form of a continuity equation

$$\frac{\partial \rho}{\partial t} = \{\varrho, H\} = -\{H, \rho\} \tag{A.8}$$

A.2 Quantum Phase Space Dynamics

Since no sharply defined trajectories in phase space exist due to Heisenberg's uncertainty relation, similar methods have not been easily available for a quantum mechanical systems. The following section briefly outlines, how these methods can be added as tools to study quantum mechanical systems when using Wigner functions for their description.

Simlarly to equation A.8, the time evolution of the density operator $\hat{\rho(t)}$ ($\hat{\rho(t)} = \sum_\alpha |\Psi^\alpha(t) >< \Psi^\alpha(t)|$) in quantum mechanical systems leads to the

Liouville-von Neumann equation

$$\frac{\partial \hat{\rho}(t)}{\partial t} = -\frac{i}{\hbar}[\hat{H}, \hat{\rho}] \tag{A.9}$$

where brackets denote the commutator $[a, b] = ab - ba$ and $\hbar$ Planck's constant divided by π.

A.3 Methods

In his paper (Wigner (1932)) Wigner introduces a quasi probability function $W(x, p; t)$ as

$$W(x, p; t) = \frac{1}{\pi\hbar} \int_{-\infty}^{\infty} dy\, \rho(x + y, x - y; t) \mathrm{e}^{\left(\frac{2i}{\hbar}\right)py} \tag{A.10}$$

with x coordinates and p momenta; and ϱ, for a pure state $\Psi(x, t)$, being related to the wave function of the quantum system in the following way

$$\varrho(x + y, x - y; t) = \Psi^*(x + y, t) \cdot \Psi(x - y, t) \tag{A.11}$$

with $\Psi^*(x; t)$ being the complex conjugate of $\Psi(x; t)$. W is a quasi probability function and normalized, 'quasi' because the function can assume negative values,

$$\int_{-\infty}^{\infty} \int_{-\infty}^{\infty} W(x, p, t)\, \mathrm{d}x\, \mathrm{d}p = 1 \tag{A.12}$$

The Wigner function has the property that its integrations with respect to one variable, its marginals, are the usual probability distributions for position $|\Psi(\mathfrak{x},t)|^2$ and momentum $(|\Phi(\mathfrak{p},t)|^2$ of the wave function,

$$|\Psi(\mathfrak{r},t)|^2 = \int_{-\infty}^{\infty} W(x, p; t)\, \mathrm{d}p \tag{A.13}$$

$$|\Phi(\mathfrak{p},t)|^2 = \int_{-\infty}^{\infty} W(x, p; t)\, \mathrm{d}x \tag{A.14}$$

In the next step a flow field J is constructed to arrive at a time evolution description of the system in terms of the Wigner function in the form of a

continuity equation, similar to the ones used in the classical case, (Donoso and Martens (2001), Wigner (1932), Schleich (2001))

$$\mathrm{J} = \begin{pmatrix} J_x \\ J_p \end{pmatrix} = \begin{pmatrix} \frac{p}{m} W(x,p;t) \\ -\sum_{l=0}^{\infty} \frac{(i\hbar/2)^{2l}}{(2l+1)!} \frac{\partial W(x,p;t)}{\partial p^{2l}} \frac{\partial^{2l+1} V(x)}{\partial x^{2l+1}} \end{pmatrix} \tag{A.15}$$

given, that the potential $V(x)$ can be expanded into a Taylor series (with respect to x). In a process similar to the one employed to obtain equation A.9, it can then be shown that the time evolution of the Wigner function W is (Wigner (1932))

$$\frac{\partial W}{\partial t} + \nabla \cdot \mathrm{J} = \frac{\partial W}{\partial t} + \frac{\partial J_x}{\partial x} + \frac{\partial J_p}{\partial p} = 0 \tag{A.16}$$

This subsequently make it possible to apply the tool set used for analysis in the classical phase space in a quantum mechanical system.

A.4 Results

This framework is used to investigate an example system: a bound state in a Caticha potential, which is a slightly asymmetric, smooth double well potential (figure A.2, a).

$$V(x) = 1 + E_0 + \frac{3}{2}\Delta E - \Delta E \alpha \sinh(2x) + \tag{A.17}$$

$$+ \cosh^2(x) \left(\frac{\Delta E^2}{4} \alpha \sinh(2x) - \frac{\Delta E^2}{4} - 2\Delta E \right) + \tag{A.18}$$

$$+ \frac{\Delta E^2}{4} (\alpha^2 + 1) \cosh^4(x) \tag{A.19}$$

Investigating the flow field by using the program outlined above, one can study how the Wigner flow field changes with time and how stagnation points (the points of the system where $|J| = 0$) and the associated local neighbourhood behave.

Some key findings, in comparison to a classical system are:

- the flow is system state dependent and so changes with time, leading to deviations from the classical trajectories,

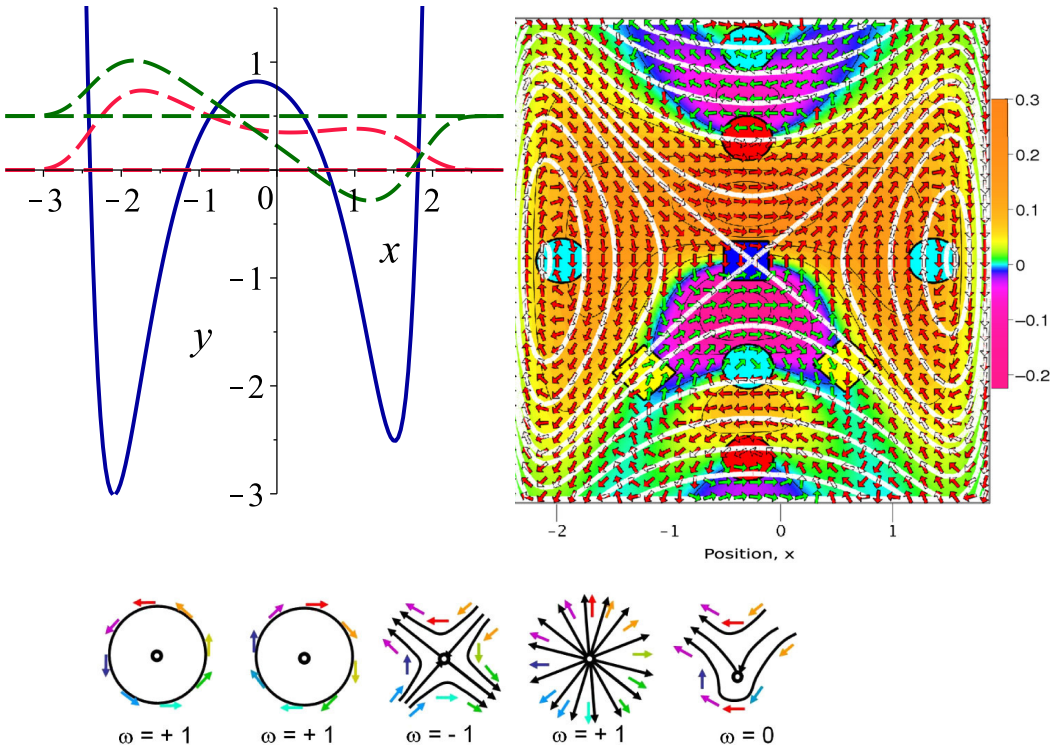

Figure A.2 – a) Plot of the Caticha potential (equation A.18) in blue (first two eigenstates are shown in red and green, (Steuernagel et al. (2013) for details)); b) Contour plot of the Wigner function $W(x, p; T/4)$, black contour lines, with arrows showing the normalized Wigner flow (J/|J|, red >0, green <0), white: classical phase portrait. All Wigner flow stagnation points are indicated with symbols: cyan and red circles indicate clockwise and anti-clockwise vortices, yellow diamonds are on separatrices and the blue square is on a saddle flow. The quantum-displacement of the vortices inwards near potential minima is clearly visible; c) Flow field around various stagnation point types and the associated winding number ω. Figure reproduced from Steuernagel et al. (2013), © American Physical Society.

- occurrence of time-dependent displacement of classical stagnation points (figure A.2, b),
- additional non classical stagnation points occur (figure A.2, b) that change position with time (figure A.3), as the flow depends on the state of the system,
- flow reversal (W can be negative) is linked with tunnelling,
- the flow winding number ω, carried by all stagnation points, is conserved.

The flow winding number $\omega(\mathcal{L};t)$ is defined as the integral around a closed convex loop $\mathcal{L}$ (figure A.2, c),

$$\omega(\mathcal{L};t) = \frac{1}{2\pi}\oint_{\mathcal{L}} d\varphi \tag{A.20}$$

and is an integer for loops that contain stagnation points.

Computing the fields of figure A.3[1] involves numerically solving J_x and J_p of the field (equation A.15) on a set of discret points (x_n, p_n, t_n). As an approximation the sums over l are terminated at $l \approx 13$, as the denominator $(2l+1)!$ becomes large very quickly. The parallelization of the computation is straightforward because every single point (x_n, p_n, t_n) can be computed independently. To compute the whole field on the three dimensional domain, I distributed the computation of individual slices on to different cluster nodes. The output data set is collected after the successful computation of all points and merged into one file. The computation of one solution on a grid domain of $800 \times 800 \times 600$ did complete in about 14 hours using 512 computational nodes (Intel Xeon® E5-2660@2.20 GHz) of the cluster.

Details and script fragments for deploying computation of slices using the computer algebra system Maple[2] for the Torque[3] job queueing system framework are given in the appendix B.3.

To visualize the simulation results I wrote the data conversion routines that facilitate import into the Vish visualization package (F5[4]), which I subsequently used to create visualizations such as figure A.3.

[1] Animated version: homepages.stca.herts.ac.uk/~phyqos/, youtube video b0odUg8EQng
[2] www.maplesoft.com
[3] `www.adaptivecomputing.com/products/open-source/torque/`
[4] `vish.fiberbundle.net`

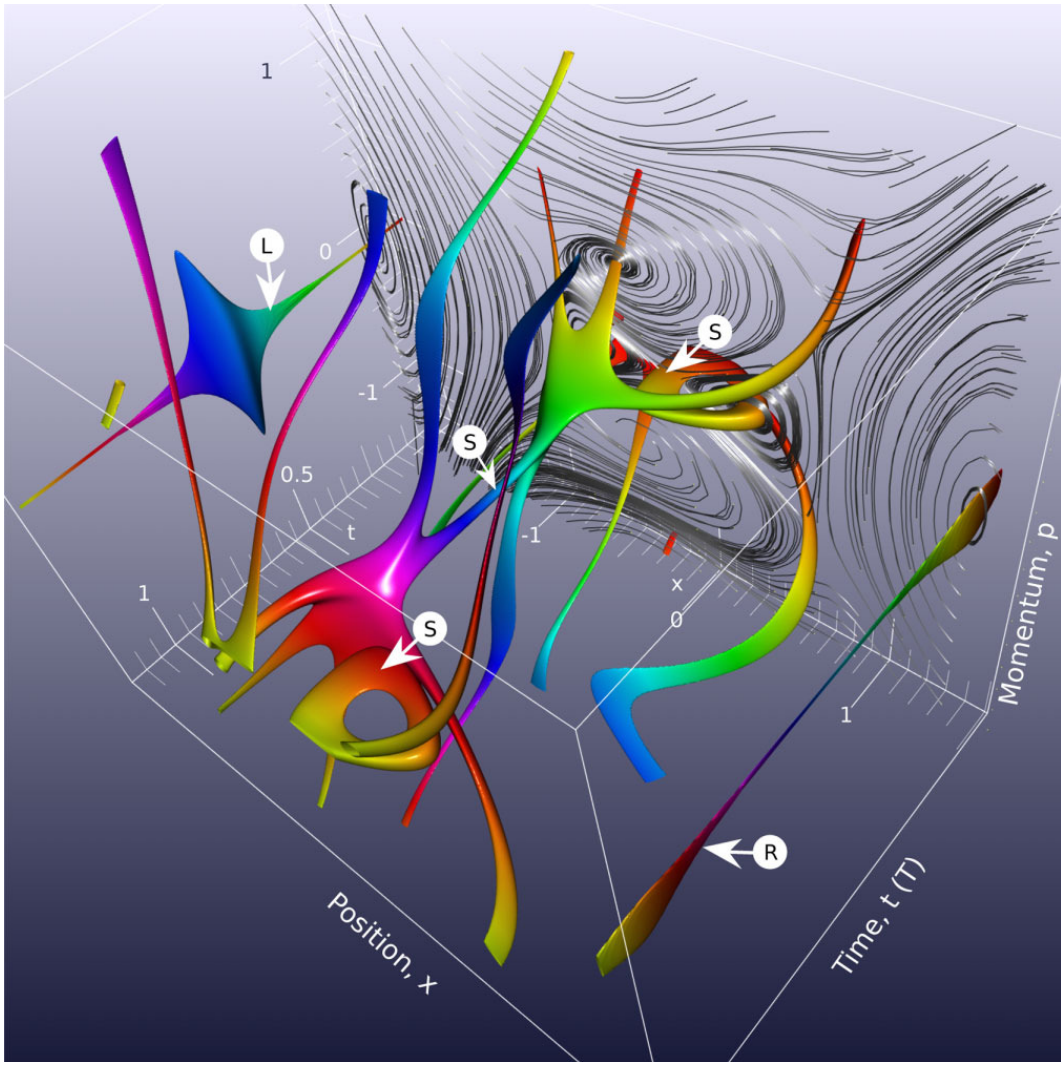

Figure A.3 – Wigner flow of the Caticha potential, phase space over time (t). The tube surface denotes a small magnitude of the flow ($|\mathrm{J}(x,p,t)|^2 = 3 \times 10^{-5}$). The time range is normalized to the period T and shown from $t = -0.1T, \ldots, 1.1T$. Colour advances with time (same colour represents same t); some features such as the yellow-orange torus are therefore seen twice. The tubes surround time lines of stagnation points as they advance with time through the phase space, with occurring splits and mergers. Grey integration lines at $t = 0.05$ help to identify separatrices (S) and vortices. The time line of the two stagnation vortices at $p = 0$, labelled (R) and (L) confirm a quantum-displacement of trajectories inwards. Figure reproduced from Steuernagel et al. (2013), © American Physical Society.

Appendix B

Source codes

B.1 VISA Instrument Access C Code

Example fragments for accessing a VISA instrument using C.

```
ViChar VISAinstradr[] = "USB0::0x0957::0x1318::TW49462520::0::INSTR";
ViChar buf[1024] = {0};
ViSession defaultRM, U2355;
unsigned short id_reg, devtype_reg;

        viOpenDefaultRM (&defaultRM);
        viOpen(defaultRM, VISAinstradr, VI_NULL, VI_NULL, &U2355);

        /* Initialize device */
        viPrintf( U2355, "*RST;CLS\n" );

        /* Send an *IDN? string to the device */
        viPrintf( U2355, "*IDN?\n");

        viScanf( U2355, "%t", buf);
        printf("Instrument identification string: %s\n", buf);
```

B.2 Pressure Conversion Table

Temperature (°C)		Pressure (Pa)		
T	T_{set}	P_{theor}	P_{set}	P
-25.2	-24	63	94	63.48
-26.2	-25	57	81	57.3
-27.2	-26	52	73	52.2
-28.1	-27	47	61	47.5
-29.2	-28	42	57	41.5
-30.3	-29	38	51	37.9
-31.1	-30	34	46	34.1
-32.1	-31	31	43	31.5
-33.05	-32	28	36	27.44
-	-33	25	-	-
-35.1	-34	22	32	23.6
-	-35	-	-	-
-37.0	-36	18	24	18.6
-	-37	-	-	-
-40.0	-39	13	19	12.53
-	-40	-	-	-
-42.0	-41	10	15	11.03
-49.8	-49	4	1	2.6

Table B.1 – This table is used to set the resulting real pressure of the system (P). For the desired pressure (P) a different (higher) pressure value needs to be set (P_{set}) because the Pirani gauge over estimates the pressures. Because the vapour content depends on the source ice temperature (T), this is inherently linked to the pressure and needs to be set concordantly (T_{set}). For a desired source ice temperature (T) the T_{set} and P_{set} are found. This is for the Deben Ultracool stage with a pre-cooling circuit temperature of 1 °C. P_{theor} is the theoretical vapour pressure for the listed T.

B.3 Maple Parallelization Scripts

The presented script fragments outline the idea of how to evaluate a function on a $100 \times 100 \times 100$ grid domain, by distributing the computation across 100 nodes which individually compute slices of $100 \times 100 \times 1$ using the computer algebra system Maple[1].

[1] `www.maplesoft.com`

The cluster job queueing system (Torque based) provides a $PBS_ARRAYID variable which increases monotonically for every node in which the job is run. By making this visible to the Maple program, it is possible to compute the different parts of a computational domain. In addition, every node needs to create a unique identifiable output file to store its data. Upon successful completion of all computational jobs on the cluster, the data files are joined and processed with a finalizer script and data converter if needed.

Torque script (array.pbs):

```
#!/bin/bash
#PBS -N p1
#PBS -l nodes=1
#...

maple -q -s  -c "istart:=$PBS_ARRAYID;" -c "iend:=$PBS_ARRAYID;"
loop-dist.mpl
```

In the Maple program (loop-dist.mpl), the variable `istart` and `iend` contain the node index, which is different on every node. As $i_{start} = i_{end}$ this selects exactly one for-loop iteration (a different version of the script shown at the bottom can select a range), as demonstrated in the Maple program fragment.

Maple program fragment (loop-dist.mpl):

```
for zn from istart to iend do
  fname:=sprintf("%s_%04d.dat",fprefix, zn);
  fd := fopen(fname, WRITE);
  for yn from 1 to ZN do
    for xn from 1 to XN do
       # compute and store
       data[xn,yn]:=f( X(xn), Y(yn), Z(zn) );
    od;
  od;
  # write data.
od;
```

The job is then submitted using the command-line option `-t` of the command qsub to create an array of 100 jobs for the 100 different slices using

```
qsub -t 1-100 array.pbs
```

On a multi core desktop, the script (rundesktop.sh) given below can be used to distributing ranges of the outer loop onto the different cores. Which is executed through invoking. This is executed with `./rundesktop loop-unroll.mpl`.

rundesktop.sh

```
#!/bin/bash
#
# Maple loop distribute: desktop (multi core)
# G Ritter, London 2011

# warning: no spaces between varname and "=" and number!

# This sets the start and endvalue for the outer unrolled loop as
# for i = LOOP_VAR_I_start to LOOP_VAR_I_end
#   other code including inner loops
# end

# NOTE: you want to start from 1 to to get 100 iterations run 1 to 100
#       and not 0 to 100
LOOP_VAR_I_START=1
LOOP_VAR_I_END=100

# set this to the number of cores on the desktop PC
NNODES=4

# Path to maple.
MAPLE="/opt/maple13"

##### no need to modify below

let TOTALSTEPS=$LOOP_VAR_I_END-$LOOP_VAR_I_START
let STEPSperNODE=($TOTALSTEPS)/$NNODES

echo totals $TOTALSTEPS
echo stepspernode $STEPSperNODE

let ISTART=$LOOP_VAR_I_START
let IEND=$ISTART+$STEPSperNODE
```

```
let FULLNODES=$NNODES-1
for job in $(eval echo "{1..$FULLNODES}")
do
  if  [ $ISTART -ge $LOOP_VAR_I_END ]; then
  break;
  fi
  #echo from $ISTART to $IEND
  $MAPLE/bin/maple -q -s -c "istart:=$ISTART;" -c "iend:=$IEND;"
$1 &
  let ISTART=$IEND+1
  let IEND=$ISTART+$STEPSperNODE
done

#echo $ISTART
#echo $IEND
if [ $ISTART -le $LOOP_VAR_I_END ]; then
  let IEND=$LOOP_VAR_I_END
  #echo last $ISTART to $IEND
  $MAPLE/bin/maple -q -s -c "istart:=$ISTART;" -c "iend:=$IEND;"
$1 &
fi
wait
```

B.4 Thermal Conductivities

Material	Thermal Conductivity ($W\,m^{-1}K^{-1}$)	Lattice
Tungsten	173	bcc
Silicon	149	diamond cubic
Copper	≈380	bcc
Epoxy Adhesives	<1	—
Amorphous glass	≈1	—
Ice (near -20°C)	2.4	
Diamond (synthetic) plate	>1900	diamond cubic

Table B.2 – Thermal conductivities of several materials.

Bibliography

Agilent Technologies. VISA user's guide. Technical report, 2001.

J. Almeida, S. Schobesberger, A. Kürten et al. Molecular understanding of sulphuric acid-amine particle nucleation in the atmosphere. *Nature*, 502(7471): 359–363, 2013.

S. Arrhenius. On the influence of carbonic acid in the air upon the temperature of the ground. *Phil. Mag.*, 41:237–276, 1896.

J. D. Atkinson, B. J. Murray, M. T. Woodhouse et al. The importance of feldspar for ice nucleation by mineral dust in mixed-phase clouds. *Nature*, 498:355–358, 2013.

M. P. Bailey and J. A. Hallett. Comprehensive habit diagram for atmospheric ice crystals: confirmation from the laboratory, AIRS II, and other field studies. *J. Atm. Sci.*, 66:2888–2899, 2009.

M. B. Baker. Cloud microphysics and climate. *Science*, 276:1072–1077, 1997.

A. J. Baran. From the single-scattering properties of ice crystals to climate prediction: A way forward. *Atm. Res.*, 112:45–69, 2012.

A. J. Baran, R. Cotton, K. Furtado et al. A self-consistent scattering model for cirrus. II: The high and low frequencies. *Q. J. Roy. Meteorol. Soc.*, 140:1039–1057, 2014a.

A. J. Baran, P. Hill, K. Furtado et al. A coupled cloud physics-radiation parameterization of the bulk optical properties of cirrus and its impact on the met office unified model global atmosphere 5.0 configuration. *J. Climate*, June 25, 2014b.

P. R. F. Barnes, R. Mulvaney, E. W. Wolff et al. A technique for the examination of polar ice using the scanning electron microscope. *J. Microsc.*, 205(2):118–124, 2002.

I. L. Barnett, A. Lignell and M. S. Gudipati. Survival depth of organics in ices under low-energy electron radiation (<=2 keV). *Astrophys. J.*, 747(1):13, 2012.

J. W. Barrett, H. Garcke and R. Nürnberg. Numerical computations of faceted pattern formation in snow crystal growth. *Phys. Rev. E*, 86:011604, 2012.

S. Barsky and M. Petrou. The 4-source photometric stereo technique for three-dimensional surfaces in the presence of highlights and shadows. *IEEE Trans. Pattern Anal. Mach. Intell.*, 25(10):1239–1252, 2003.

L. S. Bartell. Diffraction studies of clusters generated in supersonic flow. *Chem. Rev.*, 86(3):491–505, 1986.

T. Bartels-Rausch, H.-W. Jacobi, T. F. Kahan et al. A review of air-ice chemical and physical interactions (AICI): liquids, quasi-liquids, and solids in snow. *Atmos. Chem. Phys.*, 14(3):1587–1633, 2014.

T. Bartels-Rausch, V. Bergeron, J. H. E. Cartwright et al. Ice structures, patterns, and processes: A view across the icefields. *Rev. Mod. Phys.*, 84:885–944, 2012.

W. Benger, G. Ritter and R. Heinzl. The concepts of vish. In 4^{th} *High-End Visualization Workshop, Obergurgl, Tyrol – Austria, June 18-21*, pages 26–39. Berlin and Lehmanns Media-LOB.de, 2007. ISBN 978-3-86541-216-4.

M. V. Berry. Supernumerary ice-crystal halos? *Appl. Opt.*, 33(21):4563–4568, 1994.

S. Biagi. Monte Carlo simulation of electron drift and diffusion in counting gases under the influence of electric and magnetic fields. *Nucl. Instrum. Methods Section A*, 421:234–240, 1999.

R. E. Bolz and G. L. Tuve. *CRC Handbook of Tables for Applied Engineering Science*. CRC Press, US, 1973.

G. Brisebois. Low noise amplifiers for small and large area photodiodes, design note 399. Technical report, Linear Technologies, 2006.

R. T. Bruintjes. A review of cloud seeding experiments to enhance precipitation and some new prospects. *B. Am. Meteorol. Soc.*, 80(5):805, 1999.

V. Buch, S. Bauerecker, J. P. Devlin et al. Solid water clusters in the size range of tens–thousands of H2O: a combined computational/spectroscopic outlook. *Int. Rev. Phys. Chem.*, 23(3):375–433, 2004.

J. H. E. Cartwright, B. Escribano and C. I. Sainz-Diaz. The mesoscale morphologies of ice films: Porous and biomorphic. *Astrophs. J.*, 687:1406, 2008.

S. Chen and I. Baker. In-situ observations of snow sublimation using scanning electron microscopy. In *66th Eastern Snow Conference*, Niagara-on-the-Lake, Ontario, Canada, 2009.

C. Chou, J. Ulanowski, P. Herenz et al. Experimental evidence of ice crystal roughness upon relative humidity cycles. in preparation, 2014.

T. Claquin, M. Schulz and Y. J. Balkanski. Modeling the mineralogy of atmospheric dust sources. *J. Geophys. Res-Space*, 104:22243–22256, 1999.

G. Cohen and G. Coon. Theoretical consideration of retarded control. *Trans. ASME*, 75:827–834, 1953.

B. H. Cole, P. Yang, B. A. Baum et al. Ice particle habit and surface roughness derived from parasol polarization measurements. *Atmos. Chem. Phys.*, 14: 3739–3750, 2014.

P. J. Connolly, M. J. Flynn, Z. Ulanowski et al. Calibration of the cloud particle imager probes using calibration beads and ice crystal analogs: The depth of field. *J. Atmos. Oceanic. Technol.*, 24(11):1860–1879, 2007.

P. Conrad, G. E. Ewing, R. L. Karlinsey et al. Ice nucleation on BaF2(111). *J. Chem. Phys.*, 122(6):064709, 2005.

R. Cotton, S. Osborne, Z. Ulanowski et al. The ability of the small ice detector (SID-2) to characterize cloud particle and aerosol morphologies obtained during flights of the FAAM BAe-146 research aircraft. *J. Atmos. Oceanic*, 27: 290–303, 2009.

S. J. Cox, S. M. Kathmann, J. A. Purton et al. Non-hexagonal ice at hexagonal surfaces: the role of lattice mismatch. *Phys. Chem. Chem. Phys.*, 14(22): 7944–7949, 2012.

J. Crank. *The mathematics of diffusion*. Clarendon Press, Oxford, 1975.

M. C. Croarkin, W. F. Guthrie, G. W. Burns et al. Temperature-electromotive force reference functions and tables for the letter-designated thermocouple types based on the ITS-90. Technical report, Natl. Inst. Stand. Technol. Monograph 175, 1993.

J. D. Cross. Scanning electron microscopy of evaporating ice. *Science*, 164: 174–177, 1969.

J. D. Cross. The effect of impurities on the surface structure of evaporating ice. *J. Glaciol.*, 10(59):287–292, 1971.

D. Cullen and I. Baker. Observation of impurities in ice. *Microsc. Res. Techniq.*, 55: 1980207, 2001.

G. D. Danilatos. Foundations of environmental scanning electron microscopy. *Advances in electronics and electron physics*, 71:109–249, 1988.

J. G. Dash, H. Fu and J. S. Wettlaufer. The premelting of ice and its environmental consequences. *Rep. Prog. Phys.*, 58(1):115–167, 1995.

J. Dash and J. Wettlaufer. The surface physics of ice in thunderstorms. *Can. J. Phys.*, 81(1-2):201–207, 2003.

F. Domine, T. Lauzier, A. Cabanes et al. Snow metamorphism as revealed by scanning electron microscopy. *Microsc. Res. Techniq.*, 62:22–48, 2003.

A. Donoso and C. C. Martens. Quantum tunneling using entangled classical trajectories. *Phys. Rev. Lett.*, 87(22):223202, 2001.

D. Drouin, A. R. Couture, D. Joly et al. CASINO V2.42, a fast and easy-to-use modeling tool for scanning electron microscopy and microanalysis users. *Scanning*, 29(3):92–101, 2007.

J. Edwards, S. Havemann, J.-C. Thelen et al. A new parametrization for the radiative properties of ice crystals: Comparison with existing schemes and impact in a GCM. *Atm. Res.*, 83:19–35, 2007.

R. Egerton, P. Li and M. Malac. Radiation damage in the TEM and SEM. *Micron*, 35: 399–409, 2004.

M. Elbaum and J. Wettlaufer. Relation of growth and equilibrium crystal shapes. *Phys. Rev. E.*, 48(4):3180–3183, 1993.

M. Elbaum. Roughening transition observed on the prism facet of ice. *Phys. Rev. Lett.*, 67(21):2982–2985, 1991.

K. Eleftheratos, C. S. Zerefos, P. Zanis et al. A study on natural and manmade global interannual fluctuations of cirrus cloud cover for the period 1984–2004. *Atmos. Chem. Phys.*, 7(10):2631–2642, 2007.

P. J. Feibelman. Lattice match in density functional calculations: ice Ihvs.β-AgI. *Phys. Chem. Chem. Phys.*, 10(32):4688–4691, 2008.

G. Fish, O. Bouevitch, S. Kototov et al. Ultrafast response micropipette-based submicrometer thermocouple. *Rev. Sci. Instrum.*, 66(5):3300–3306, 1995.

A. Fletcher, B. Thiel and A. Donald. Amplification measurements of alternative imaging gases in environmental SEM. *J. Phys. D: Appl. Phys.*, 30:2249–2257, 1997.

A. I. Flossmann and W. Wobrock. A review of our understanding of the aerosol–cloud interaction from the perspective of a bin resolved cloud scale modelling. *Atm. Res.*, 97:478–497, 2010.

D. A. Forsyth and J. Ponce. *Computer vision: a modern approach*, chapter 5 Source, shadows and shading, pages 55–68. Pearson Prentice Hall, 2003.

J. Fourier. Remarques générales sur les températures du globe terrestre et des espaces planétaires. *Ann. Chimie Physique*, 27:136, 1824.

N. Fukuta and B. Mason. Epitaxial growth of ice on organic crystals. *J. Phys. Chem. Solids*, 24(6):715 – 718, 1963.

N. Fukuta and T. Takahashi. The growth of atmospheric ice crystals: A summary of findings in vertical supercooled cloud tunnel studies. *J. Atm. Sci.*, 56(12): 1963–1979, 1999.

H. O. Funsten, D. M. Suszcynsky, S. M. Ritzau et al. Response of 100 % internal quantum efficiency silicon photodiodes to 200 eV to 40 keV electrons. *IEEE T. Nucl. Sci.*, 44(6):2561–2565, 1997.

Y. Furukawa and J. S. Wettlaufer. Snow and ice crystals. *Phys. Today*, 325:70–71, 2007.

K. Gierens, U. Schumann, M. Helten et al. Ice-supersaturated regions and subvisible cirrus in the northern midlatitude upper troposphere. *J. Geophys. Res.,*, 105:22743–22753, 2000.

T. Gonda and T. Yamazaki. Morphological stability of polyhedral ice crystals growing from the vapor phase. *J. Cryst. Growth*, 60:259–263, 1982.

J. Gravner and D. Griffeath. Modeling snow-crystal growth: A three-dimensional mesoscopic approach. *Phys. Rev. E*, 79:011601, 2009.

A. Guignard, C. J. Stubenrauch, A. J. Baran et al. Bulk microphysical properties of semi-transparent cirrus from AIRS: a six year global climatology and statistical analysis in synergy with geometrical profiling data from CloudSat-CALIPSO. *Atmos. Chem. Phys.*, 12(1):503–525, 2012.

G. Hall. Solid propellant temperature profiles obtained through embedded microthermocouples. Technical report, Astronautics Laboratory (AFSC), Edwards AFB CA 93523-5000, 1990.

J. Hallett and B. J. Mason. The influence of temperature and supersaturation on the habit of ice crystal grown from vapour. *Proc. R. Soc. Lond. A*, 247:440–453, 1958.

D. Hamilton. Performance of transfer resistance amplifiers with capacitive sources in optical applications. *Circuits, Devices and Systems, IEEE Proceedings G*, 138(1):45 –51, 1991.

R. H. Hamstra and P. Wendland. Noise and frequency response of silicon photodiode operational amplifier combination. *Appl. Opt.*, 11(7):1539–1547, 1972.

S. Hartmann, D. Niedermeier, J. Voigtländer et al. Homogeneous and heterogeneous ice nucleation at LACIS: operating principle and theoretical studies. *Atmos. Chem. Phys.*, 11(4):1753–1767, 2011.

D. A. Hegg and M. B. Baker. Nucleation in the atmosphere. *Rep. Prog. Phys.*, 72(5): 056801, 2009.

A. K. Heidinger and M. J. Pavolonis. Global daytime distribution of overlapping cirrus cloud from NOAA's advanced very high resolution radiometer. *J. Climate*, 18(22):4772–4784, 2005.

B. F. Henson, L. F. Voss, K. R. Wilson et al. Thermodynamic model of quasiliquid formation on H2O ice: Comparison with experiment. *J. Chem. Phys.*, 123:144707, 2005.

E. Hesse and Z. Ulanowski. Scattering from long prisms computed using ray tracing combined with diffraction on facets. *J. Quantit. Spectr. Rad. Transf.*, 79: 721–732, 2003.

C. Hoose and O. Möhler. Heterogeneous ice nucleation on atmospheric aerosols: a review of results from laboratory experiments. *Atmos. Chem. Phys.*, 12(20): 9817–9854, 2012.

X. L. Hu and A. Michaelides. Water on the hydroxylated (001) surface of kaolinite: From monomer adsorption to a flat 2D wetting layer. *Surf. Sci.*, 602(4):960–974, 2008.

X. L. Hu and A. Michaelides. The kaolinite (001) polar basal plane. *Surf. Sci.*, 604 (2):111–117, 2010.

J. P. Ibe, J. P. P. Bey, S. L. Brandow et al. On the electrochemical etching of tips for scanning tunneling microscopy. *JVST A*, 8(4):3570–3575, 1990.

Y. Itikawa and N. Mason. Cross sections for electron collisions with water molecules. *J. Phys. Chem. Ref. Data.*, 34(1):1–22, 2005.

E. J. Jensen, P. Lawson, B. Baker et al. On the importance of small ice crystals in tropical anvil cirrus. *Atmos. Chem. Phys.*, 9(15):5519–5537, 2009.

D. Kaczmarek. Backscattered electrons topographic mode problems in the scanning electron microscope. *Scanning Microscopy*, 12(1):161–169, 1998.

K. Kanaya and S. Okayama. Penetration and energy-loss theory of electrons in solid targets. *J. Phys. D: Appl. Phys.*, 5(43):43–58, 1972.

P. H. Kaye, E. Hirst, R. S. Greenaway et al. Classifying atmospheric ice crystals by spatial light scattering. *Opt. Lett.*, 33(13):1545–1547, 2008.

J. Kiehl and V. Ramanathan. *The frontiers of climate modelling*. Cambridge Univ. Press, UK, 2006.

K. Kikuchi, T. Kameda, K. Higuchi et al. A global classification of snow crystals, ice crystals, and solid precipitation based on observations from middle latitudes to polar regions. *Atm. Res.*, 132:460–472, 2013.

D.-J. Kim and J.-Y. Koo. A low-noise and wide-band ac boosting current-to-voltage amplifier for scanning tunneling microscopy. *Rev. Sci. Instrum.*, 76:023703–1, 2005.

Y.-K. Kim and M. Rudd. Binary-encounter-dipole model for electron-impact ionization. *Phys. Rev. A*, 50:3954–3967, 1994.

J. Kirkby, J. Curtius, J. Almeida et al. Role of sulphuric acid, ammonia and galactic cosmic rays in atmospheric aerosol nucleation. *Nature*, 476(7361):429–433, 2011.

T. N. Knepp, T. L. Renkens and P. B. Shepson. Gas phase acetic acid and its qualitative effects on snow crystal morphology and the quasi-liquid layer. *Atmos. Chem. Phys.*, 9:7679–7690, 2009.

T. Kobayashi. The growth of snow crystals at low supersaturation. *Philos. Mag.*, 6: 71–80, 1961.

T. Kobayashi and K. Higuchi. On the pyramidal faces of ice crystals. Technical report, Contributions from the Institute of Low Temperature Science, 1957.

A. V. Korolev, E. F. Emery, J. W. Strapp et al. Small ice particles in tropospheric clouds: Fact or artifact? Airborne icing instrumentation evaluation experiment. *B. Am. Meteorol. Soc.*, 92(8):967–973, 2010.

A. V. Korolev and M. I. P. Supersaturation of water vapor in clouds. *J. Atm. Sci.*, 60 (24):2957–2974, 2003.

M. Krämer, C. Schiller, A. Afchine et al. Ice supersaturations and cirrus cloud crystal numbers. *Atmos. Chem. Phys.*, 9(11):3505–3522, 2009.

W. F. Kuhs, G. Genov, D. K. Staykova et al. Ice perfection and onset of anomalous preservation of gas hydrates. *Phys. Chem. Chem. Phys.*, 6:4917–4920, 2004.

W. F. Kuhs, C. Sippel, A. Falenty et al. Extent and relevance of stacking disorder in "ice Ic". *PNAS*, 109(52):21259–21264, 2012.

T. Kuroda. Rate determining processes of growth of ice crystals from the vapour phase part I: Theoretical consideration. *J. Meteor. Soc. Japan*, 62(3):552–562, 1984.

T. Kuroda and T. Gonda. Rate determining processes of growth of ice crystals from the vapour phase part II: Investigation of surface kinetic process. *J. Meteor. Soc. Japan*, 62(3):563–673, 1984.

L.-C. Labonnote, G. Brogniez, J.-C. Buriez et al. Polarized light scattering by inhomogeneous hexagonal monocrystals: Validation with adeos-polder measurements. *J. Geophys. Res-Space.*, 106:12139–12153, 2007.

A. A. Lacis, G. A. Schmidt, D. Rind et al. Atmospheric CO2: Principal control knob governing earth's temperature. *Science*, 330:356, 2010.

A. Lakhtakia and R. Messier. *Sculptured thin films: nanoengineered morphology and optics*. SPIE Press, Bellingham, WA, 2005.

D. Lamb and P. Hobbs. Growth rates and habits of ice crystals grown from the vapor phase. *J. Atm. Sci.*, 28,:1506–1509, 1971.

L. Landau and E. Lifshitz. *Mechanics, a course of theoretical physics*, volume 1. Pergamon Press, 1969.

K. G. Libbrecht and R. Bell. Chemical influences on ice crystal growth from vapor. *ArXiv e-prints*, arXiv:1101.0127 [cond-mat.mtrl-sci]:1–7, 2011.

K. G. Libbrecht and H. C. Morrison. A convection chamber for measuring ice crystal growth dynamics. *ArXiv e-prints*, arXiv:0809.4869[cond-mat.mtrl-sci], 2008.

H. Lindqvist, O. Jokinen, K. Kandler et al. Modelling mineral dust using stereophotogrammetry. *AAPP*, 89(1):58–1 – 58–4, 2011.

G. Ling and R. W. Gerard. The normal membrane potential of frog sartorius fibers. *J. Cell. Physio.*, 34(3):383–396, 1949.

A.-S. Lucier. Preparation and characterization of tungsten tips suitable for molecular electronics studies. Master's thesis, Center for the Physics of Materials, McGill University, 2001.

D. K. Lynch. *Cirrus*. Oxford University Press, 2002.

A. Macke, J. Mueller and R. E. Single scattering properties of atmospheric ice crystals. *J. Atm. Sci.*, 53:2813–25, 1996.

A. Macke, P. N. Francis, G. M. McFarquhar et al. The role of ice particle shapes and size distributions in the single scattering properties of cirrus clouds. *J. Atm. Sci.*, 55(17):2874–2883, 1998.

C. Magono and C. W. Lee. Meteorological classification of natural snow crystals. *Jour. Fac. Sci., Hokkaido Univ.*, 2(4):321–366, 1966.

T. L. Malkin, B. J. Murray, A. V. Brukhno et al. Structure of ice crystallized from supercooled water. *PNAS*, 109(10):4020, 2012.

M. Maruyama, T. Ashida and C. A. Knight. Disk crystals of ice grown in air-free water: no effect of dissolved air on the morphology. *J. Cryst. Growth.*, 205(3):391 – 394, 1999.

T. Matsukawa, R. Shimizu and H. Hashimoto. Measurements of the energy distribution of backscattered kilovolt electrons with a spherical retarding-field energy analyser. *J. Phys. D: Appl. Phys.*, 7:695–702, 1974.

M. Matsumoto, S. Saito and I. Ohmine. Molecular dynamics simulation of the ice nucleation and growth process leading to water freezing. *Nature*, 416:409–413, 2002.

A. Maurellis and J. Tennyson. The climatic effects of water vapour. *Phys. World*, 5: 1–5, 2003.

W. Mayneord. The significance of the Röntgen. *Acta — Unio Internationalis Contra Cancrum*, 2:271–282, 1937.

G. M. McFarquhar and A. J. Heymsfield. Parameterization of tropical cirrus ice crystal size distributions and implications for radiative transfer: results from CEPEX. *J. Atmos. Sci.*, 54:2187–2200, 1997.

G. M. McFarquhar, A. J. Heymsfield, J. Spinhirne et al. Thin and subvisual tropopause tropical cirrus: observations and radiative impacts. *J. Atm. Sci.*, 57: 1841–1853, 2000.

G. Mie. Beiträge zur Optik trüber Medien, speziell kolloidaler Metallösungen. *Ann. Phys-Leipzig.*, 330(3):377–445, 1908.

O. Möhler, P. R. Field, P. Connolly et al. Efficiency of the deposition mode ice nucleation on mineral dust particles. *Atmos. Chem. Phys.*, 6(10):3007–3021, 2006.

E. Moore and V. Molinero. Is it cubic? Ice crystallization from deeply supercooled water. *Phys. Chem. Chem. Phys.*, 13:20008–16, 2011.

C. E. Morris, D. G. Georgakopoulos and D. C. Sands. Ice nuleation active bacteria and their potential role in precipitation. *J. Phys. IV France*, 121:87–103, 2004.

R. Mulvaney, E. W. Wolff and K. Oates. Sulphuric acid at grain boundaries in antarctic ice. *Nature*, 331(6153):247–249, 1988.

D. M. Murphy and T. Koop. Review of the vapour pressures of ice and supercooled water for atmospheric applications. *Q. J. Roy. Meteorol. Soc.*, 131:1539–1565, 2005.

B. J. Murray, D. O'Sullivan, J. D. Atkinson et al. Ice nucleation by particles immersed in supercooled cloud droplets. *Chem. Soc. Rev.*, 41(19):6519–6554, 2012.

P. J. Neiman. The Boulder, Colorado, concentric halo display of 21 july 1986. *Bull. Am. Meteorol. Soc.*, 70:258–264, 1989.

J. Nelson. Sublimation of ice crystals. *J. Atm. Sci.*, 55:910–919, 1998.

J. Nelson and C. A. Knight. A new technique for growing crystals from the vapor. *J. Cryst. Growth*, 169:795–797, 1996.

S. P. Neshyba, B. Lowen, M. Benning et al. Roughness metrics of prismatic facets of ice. *J. Geophys. Res. D*, 118(8):3309–3318, 2013.

S. Nikzad, T. Cunningham, M. E. Hoenk et al. Direct detection of 0.1–20 keV electrons with delta doped, fully depleted, high purity silicon p-i-n diode arrays. *Appl. Phys. Lett.*, 89(18):182114, 2006.

F. K. Odenkrantz. Modification of habit and charge of ice crystals by vapor contamination. *J. Atmos. Sci.*, 25:337–338, 1968.

E. A. Ouellette and A. Harris. Thermal conductivity of diamond-loaded glues for the ATLAS particle physics detector. Technical Report arXiv:1008.0876, CERN, 2010. Comments: Submitted to J.Phys. D.

J. Paluszynski and W. Slowko. Measurements of the surface microroughness with the scanning electron microscope. *J. Microsc.*, 233:10–17, 2009.

G. W. Petty. *A first course in atmospheric radiation (2nd Ed.)*. Sundog Publishing, 2006. ISBN 0972903313.

W. C. Pfalzgraff, R. M. Hulscher and S. P. Neshyba. Scanning electron microscopy and molecular dynamics of surfaces of growing and ablating hexagonal ice crystals. *Atmos. Chem. Phys.*, 10(6):2927–2935, 2010.

Application Bulletin AB-075. Photodiode monitoring with op-amps. Burr-Brown/Texas Instruments, US, 1994.

I. Plante and F. A. Cucinotta. Cross sections for the interactions of 1 eV–100 MeV electrons in liquid water and application to Monte-Carlo simulation of HZE radiation tracks. *New J. Phys.*, 11(6):063047, 2009.

H. Preston-Thomas. The international temperature scale of 1990 (ITS90). *Metrologia*, 27:3–10, 1990.

H. Pruppacher and J. Klett. *Microphysics of clouds and precipitation*. Springer, 2010.

A. Rango, W. P. Wergin and E. F. Erbe. Snow crystal imaging using scanning electron microscopy: II. Metamorphosed snow. *Hydrolog. Sci. J.*, 41(2):235–250, 1996.

A. Rango, J. Foster, E. G. Josberger et al. Rime and graupel: description and characterization as revealed by low-temperature scanning electron microscopy. *Scanning*, 25(3):121–131, 2003.

M. Riikonen, M. Sillanpää, L. Virta et al. Halo observations provide evidence of airborne cubic ice in the Earth's atmosphere. *Appl. Opt.*, 39(33):6080–6085, 2000.

D. Rivera, M. Morari and S. Skogestad. Internal model control. 4. PID controller design. *Ind. Eng. Chem. Res.*, 25(1):252–265, 1986.

W. Rosenthal, J. Saleta and J. Dozier. Scanning electron microscopy of impurity structures in snow. *Cold Reg. Sci. Technol.*, 47(1-2):80 – 89, 2007.

K. Sassen, N. C. Knight, Y. Takano et al. Effects of ice-crystal structure on halo formation: cirrus cloud experimental and ray-tracing modeling studies. *Appl. Opt.*, 33(21):4590–5002, 1994.

K. Sassen, J. Zhu and S. Benson. Midlatitude cirrus cloud climatology from the Facility for Atmospheric Remote Sensing. IV. Optical displays. *Appl. Opt.*, 42(3): 332–340, 2003.

K. Sassen, Z. Wang and D. Liu. Global distribution of cirrus clouds from CloudSat/Cloud-Aerosol Lidar and Infrared Pathfinder Satellite Observations (CALIPSO) measurements. *J. Geophys. Res. D*, 113(D8):D00A12, 2008.

C. Saunders. Charge separation mechanisms in clouds. *Space Sci. Rev.*, 137:335, 2008.

G. Sazaki, S. Zepeda, S. Nakatsuboa et al. Elementary steps at the surface of ice crystals visualized by advanced optical microscopy. *PNAS*, 107(46): 19702–19707, 2010.

W. P. Schleich. *Quantum optics in phase space*. Wiley-VCH Verlag, Weinheim, DE, 2001.

C. G. Schmitt and A. J. Heymsfield. On the occurrence of hollow bullet rosette– and column–shaped ice crystals in midlatitude cirrus. *J. Atm. Sci.*, 64:4514–4519, 2007.

SCPI. *Standard Commands for Programmable Instruments, volume 1: Syntax and style*. Standard-Commands-for-Programmable-Instruments (SCPI) Consortium, 1999.

J. A. Sellberg, C. Huang, T. A. McQueen et al. Ultrafast X-ray probing of water structure below the homogeneous ice nucleation temperature. *Nature*, 510 (7505):381–384, 2014.

V. Shcherbakov, J. F. Gayet, O. Jourdan et al. Light scattering by single ice crystals of cirrus clouds. *Geophys. Res. Lett.*, 33(15):L15809, 2006a.

V. Shcherbakov. Why the 46° halo is seen far less often than the 22° halo? *J. Quant. Spectrosc. Ra.*, 124:37–44, 2013.

V. Shcherbakov, J.-F. Gayet, B. Baker et al. Light scattering by single natural ice crystals. *J. Atm. Sci.*, 63(5):1513–1525, 2006b.

J. E. Shilling, M. A. Tolbert, O. B. Toon et al. Measurements of the vapor pressure of cubic ice and their implications for atmospheric ice clouds. *Geophys. Res. Lett.*, 33(17):L17801, 2006.

J. Smagorinsky. General circulation experiments with the primitive equations. *Mon. Weather. Rev.*, 91:99–164, 1963.

P. Spichtinger, K. Gierens and W. Read. The global distribution of ice-supersaturated regions as seen by the microwave limb sounder. *Quart. J. Roy. Meteorol. Soc.*, 129:3391–3410, 2003.

M. Spranck, M. Kaessens and L. Reimer. Influence of the angular distribution of backscattered electrons on signals at different take-off angles in low-voltage scanning electron microscopy (LVSEM). *Scanning*, 17:97–105, 1995.

P. F. Staub. Bulk target backscattering coefficient and energy distribution of 0.5-100 keV electrons: an empirical and synthetic study. *J. Phys. D: Appl. Phys.*, 27:1533–1537, 1994.

O. Steuernagel, D. Kakofengitis and G. Ritter. Wigner flow reveals topological order in quantum phase space dynamics. *Phys. Rev. Lett.*, 110(3):030401, 2013.

B. Stevens and S. Bony. What are climate models missing? *Science*, 340: 1053–1054, 2013.

T. Stocker, D. Qin, G.-K. Plattner et al, editors. *IPCC, 2013: Climate Change 2013: The physical science basis. Contribution of working group I to the fifth assessment report of the Intergovernmental Panel on Climate Change*. Cambridge University Press, Cambridge, United Kingdom and New York, NY, USA, 2013.

D. J. Stokes. Environmental scanning electron microscopy for biology and polymer science. *Microscopy and Analysis*, 26(6):67–71, 2012.

F. Stratmann, A. Kiselev, S. Wurzler et al. Laboratory studies and numerical simulations of cloud droplet formation under realistic supersaturation conditions. *J. Atmos. Oceanic.*, 21(6):876–887, 2004.

C. J. Stubenrauch, A. Chédin, G. Rädel et al. Cloud properties and their seasonal and diurnal variability from TOVS Path-B. *J. Climate*, 19(21):5531–5553, 2006.

W. Tape and G. P. Können. A general setting for halo theory. *Appl. Opt.*, 38(9): 1552–1625, 1999.

M. L. Taylor, R. L. Smith, F. Dossing et al. Robust calculation of effective atomic numbers: the Auto-Zeff software. *Med. Phys.*, 39:1769, 2012.

B. Thiel. Imaging properties of various gases in the environmental SEM. In *Inst. Phys. Conf. Ser. No 168; Section 3, Electron Microscopy and Analysis Group Conf. EMAG2001, Dundee*, 2001.

B. L. Thiel, I. C. Bache, A. L. Fletcher et al. An improved model for gaseous amplification in the environmental SEM. *J. Microsc.*, 187:143–157, 1997.

A. C. Thomas. *Growth of thin film water on α-Al2O3 (0001) and its implications for ice nucleation.* PhD thesis, Department of Chemistry and Biochemistry, Ohio University, US, 2009.

K. Thürmer and N. C. Bartelt. Growth of multilayer ice films and the formation of cubic ice imaged with STM. *Phys. Rev. B*, 77(19):195425, 2008.

K. E. Trenberth, J. T. Fasullo and J. Kieh. Earth's global energy budget. *B. Am. Meteorol. Soc.*, 90:311–323, 2009.

J. Tyndall. On the passage of radiant heat through dry and humid air. *Philos. Mag.*, 26:169–194, 273–285, 1863.

Z. Ulanowski, E. Hirst, P. Kaye et al. Retrieving the size of particles with rough and complex surfaces from two-dimensional scattering patterns. *J. Quant. Spectrosc. Radiat. Transfer.*, 113(18):2457–2464, 2012.

Z. Ulanowski, P. H. Kaye, E. Hirst et al. Incidence of rough and irregular atmospheric ice particles from Small Ice Detector 3 measurements. *Atmos. Chem. Phys.*, 14:1649–1662, 2014.

Z. Ulanowski. Ice analog halos. *Appl. Opt.*, 44(27):5754–5758, 2005.

Z. Ulanowski, E. Hesse, P. H. Kaye et al. Scattering of light from atmospheric ice analogues. *J. Quant. Spectrosc. Radiat. Transfer.*, 79–80C:1091–1102, 2003.

Z. Ulanowski, E. Hesse, P. H. Kaye et al. Light scattering by complex ice-analogue crystals. *J. Quantit. Spectr. Rad. Transf.*, 100:382–392, 2006.

G. Vali. Ice nucleation - a review. In M. Kulmala and P. Wagner, editors, *Nucleation and Atmospheric Aerosols 1996*, pages 271–279. Pergamon, 1996.

C. M. Vitus, H. S. Isaacs and V. Schroeder. A study of the electrochemical behavior of tungsten in caustic solutions and platinum/iridium in chloride solutions. Technical report, Brookhaven National Laboratory and University of California, 1994.

J. Voigtlaender, P. Herenz, C. Chou et al. Investigation of nucleation, dynamic growth and surface properties of single ice crystals. In *GRA*, volume 16, EGU2014-5649, 2014.

B. Vonnegut. The nucleation of ice formation by silver iodide. *J. Appl. Phys.*, 18: 593–595, 1947.

L. F. Voss, B. F. Henson, K. R. Wilson et al. Atmospheric impact of quasiliquid layers on ice surfaces. *Geophys. Res. Lett.*, 32:L07807, 2005.

T. Vynnyk, T. Schultheis, T. Fahlbusch et al. 3D-measurement with the stereo scanning electron microscope on sub-micrometer structures. *J. Europ. Opt. Soc. Rap. Public.*, 5:10038s, 2010.

P. Walden, G. W. Stephen and E. Tuttle. Atmospheric ice crystals over the antarctic plateau in winter. *J. Appl. Meteorol.*, 42:1392–1405, 2003.

J. M. Wallace and P. V. Hobbs. *Atmospheric science: an introductory survey*. Academic Press, 2nd edition, 2006.

D. Waller, D. Stokes and A. Donald. Development of low temperature ESEM: exploring sublimation. *Microsc. Microanal.*, 11(2):414–415, 2005.

C. Wei-Tse, H. Ing-Shouh, C. Mu-Tung et al. Method of electrochemical etching of tungsten tips with controllable profiles. *Rev. Sci. Instrum.*, 83(8): 083704–083704–6, 2012.

W. P. Wergin, E. F. Erbe, A. Rango et al. Irregular snow crystals: Structural features as revealed by low temperature scanning electron microscopy. *Scanning*, 24(5):247–256, 2002.

A. Wexler. Vapor pressure formulation for ice. *J. Res. Natl. Bur. Stand. Sec. A*, 81(1): 5–20, 1977.

E. Whalley. Scheiner's halo: evidence for ice Ic in the atmosphere. *Science*, 211: 389–390, 1981.

E. Wigner. On the quantum correction for thermodynamic equilibrium. *Phys. Rev.*, 40(5):749–759, 1932.

N. Wildmann, M. Mauz and J. Bange. Two fast temperature sensors for probing of the atmospheric boundary layer using small remotely piloted aircraft (RPA). *Atmos. Meas. Tech.*, 6:2101–2113, 2013.

K. Williams and M. J. Webb. A quantitative performance assessment of cloud regimes in climate models. *Clim. Dyn.*, 33:141–157, 2009.

T. A. Witten and S. L. M. Diffusion-limited aggregation, a kinetic critical phenomenon. *Phys. Rev. Lett.*, 47(19):1400–1403, 1981.

T. A. Witten and L. M. Sander. Diffusion-limited aggregation. *Phys. Rev. B.*, 27(9): 5686–5697, 1983.

R. K. Yadav and R. Shanker. Energy and angular distributions of backscattered electrons from collisions of 5 keV electrons with thick Al, Ti, Ag, W and Pt targets. *Pramana*, 68:517–528, 2007.

P. Yang and K. N. Liou. Single-scattering properties of complex ice crystals in terrestrial atmosphere. *Contr. Atmos. Phys.*, 71:223–248, 1998.

M. A. Yurkin and A. G. Hoekstra. The discrete-dipole-approximation code ADDA: capabilities and known limitations. *J. Quant. Spectrosc. Radiat. Transfer*, 112(13): 2234–2247, 2011.

C. S. Zender, R. L. Miller and I. Tegen. Quantifying mineral dust mass budgets: terminology, constraints, and current estimates. *Eos Trans. AGU*, 85(48):509, 2004.

K. Zickfeld, M. G. Morgan, D. J. Frame et al. Expert judgments about transient climate response to alternative future trajectories of radiative forcing. *PNAS*, 107(28):12451–12456, 2010.

J. Ziegler and N. Nichols. Optimum settings for automatic controllers. *Trans. A.S.M.E.*, 64:759–768, 1942.

F. Zimmermann, M. Ebert, A. Worringen et al. Environmental scanning electron microscopy (ESEM) as a new technique to determine the ice nucleation capability of individual atmospheric aerosol particles. *Atmos. Env.*, 41(37): 8219–8227, 2007.